Template controlled mineralization of functional ZnO thin films

Von der Fakultät Chemie der Universität Stuttgart zur Erlangung der Würde eines Doktors der Naturwissenschaften (Dr. rer. nat.) genehmigte Abhandlung

Vorgelegt von
Nina Blumenstein
aus Stuttgart

Hauptberichter:	Prof. Dr. J. Bill
Mitberichter:	Prof. Dr. Ir. E. J. Mittemeijer

Tag der mündlichen Prüfung:
07.11.2016

Institut für Materialwissenschaft
2017

Contents

Glossary

AFM	Atomic force microscopy
APTES	(3-aminopropyl)triethoxysilane
ATR	Attenuated total reflection
AZO	Aluminum-doped zinc oxide
d_{33}	Piezoelectric coefficient
d_{eff}	Effective piezoelectric coefficient
FDTS	1H,1H,2H,2H-perfluorodecyltrichlorosilane
FET	Field effect transistor
GZO	Gallium-doped zinc oxide
His	Histidine
HMTA	Hexamethylene tetramine
ICP-AES	Inductively coupled plasma atomic emission spectroscopy

IEP	Isoelectric point
IR	Infrared spectroscopy
IRRA	Infrared reflection absorption
IZO	Indium-doped zinc oxide
LED	Light emitting diode
MeOH	Methanol
PE	Polyelectrolyte
PFM	Piezoresponse force microscopy
PGA	Poly-L-glutamic acid
PL	Photoluminescence spectroscopy
PLL	Poly-L-lysine
PMMA	Poly(methyl methacrylate)
PPLN	Periodically poled lithium niobate
PS	Polystyrene
PSS	Polystyrene sulfonate

PVP	Polyvinylpyrrolidone
SAM	Self-assembled monolayer
SEM	Scanning electron microscopy
TEAOH	Tetraethylammonium hydroxide
WCA	Water contact angle
XPS	X-ray photoelectron spectroscopy
XRD	X-ray diffraction
ζ-potential	Zeta-potential

Summary

Miniaturization in electronics is a strong driving force for the development of new materials for electronic nanodevices. Conventional production techniques often require highly sophisticated methods including vacuum techniques and heat treatments.

However, living nature provides examples for the fabrication of functional materials under ambient conditions. Organic additives and templates control crystallite growth of an inorganic phase and act as scaffolds for structure formation. The combination of the inorganic and organic phases, for example, leads to outstanding mechanical hardness and fracture toughness at the same time (e. g. in nacre).

The principles of biomineralization can be transferred to the fabrication of technically interesting materials, like ZnO. These bioinspired methods can be used to closely control the properties of the deposited material.

In this work, the bioinspired deposition of functional ZnO thin films was investigated. In the first part of this work, it was possible to show that the surface charge of the organic template can be used to control ZnO film growth. On the non-modified pre-oxidized substrate, island growth was observed even for 10 deposition cycles. Moreover, on a non-polar, fluorined self-assembled monolayer (SAM), film growth is suppressed completely. In contrast to this behavior, the investigated polar templates can interact with the dipolar ZnO crystallites in solution. The more polar the template, the more homogeneous the films get. In addition, a 002 texture can be achieved by applying a sulfonate-terminated polyelectrolyte

multilayer. This template exhibits the highest negative surface potential of all templates investigated in this work. With increasing thickness the influence of the templates vanishes. The attachment of ZnO crystallites to the already grown ZnO film and therefore the growth rate is independent of the template. Furthermore, an initially non-polar polystyrene brush was shown to be activated in the deposition solution. After a reaction with the basic medium, a polar functional group is accessible for the dipolar ZnO crystallites and a homogeneous film can grow. The interaction between the template and the crystallites is even high enough to promote a 002 texture of the film.

Deposition experiments from aqueous solution revealed that not only film growth but also film morphology can be controlled by the applied templates. A structured surface of polar islands with amino-termination in a non-polar matrix of a fluorined functionality was mineralized. The polar ZnO particles in solution can attach homogeneously to the polar template. A film with low surface roughness is formed. On the fluorined surface however, a film with high surface roughness is observed due to large agglomerates that were formed to reduce the surface energy of the ZnO particles.

In the second part of this thesis, the piezoelectric properties of films deposited onto a COOH-terminated SAM, a sulfonate-terminated polyelectrolyte multilayer and a polystyrene brush were measured. In a ZnO film with random crystallite orientation, the piezoelectric deformations are nullified. In a 002 textured film however, the deformations act in the same direction and add to a macroscopic response of the samples. As was shown in the previous part, the template polarity influences the texture of the ZnO films. It could be demonstrated that by choosing the correct template, it is possible to tune the piezoactivity of the films. The COOH-terminated template has a low surface charge and a film with random orientation is precipitated. Consequently the measured piezoresponse is very low. On the contrary, the other two templates with high surface charge lead to

textured film growth. The corresponding measured piezoelectric constants are comparable to or even higher than those found for samples deposited by conventional methods.

In the third part of this thesis, a procedure was developed for the bioinspired precipitation of ZnO films doped with Al, Ga or In. As a first result, it was shown that the introduction of the doping elements into the solution influences the film growth. For Al, the films get thicker with increasing doping content and in addition, a 002 texture can be observed. This traces back to the introduction of water into the deposition solution by adding the aluminum nitrate nonahydrate. The water increases the hydrolyzation rate and more ZnO is formed. In contrast, the introduction of Ga and In lead to a decrease in film thickness for higher doping contents. The reason is a suppression of ZnO precipitation by the competing precipitation of Ga and In hydroxides. A combination of optical emission spectroscopy (ICP-AES) and photoluminescence measurements could prove that all three doping elements are incorporated into the ZnO. The incorporated amount of Ga and In is higher compared to that of Al due to the lower difference in ionic radii to the Zn ion of the first two compared to the latter. In addition, photoluminescence measurements show that the UV band emission of ZnO can be tuned by the amount of the doping element. The more Al, Ga or In is incorporated, the higher is the blue shift of this band. Furthermore, conductivity measurements on the ZnO films doped with Ga and In show that the doping reduces the resistivity by two orders of magnitude compared to the undoped film.

In summary, this work shows that by choosing the correct template, it is possible to suppress or promote ZnO film growth from solution. By applying templates with high surface charge, it is possible to achieve a 002 texture which is responsible for a piezoelectric activity of the film. In addition, by doping with Al, Ga or In, tuning of the optical band gap and the conductivity of the ZnO films is possible.

Zusammenfassung

Mit der fortschreitenden Miniaturisierung in der Technik werden elektronische Bauteile im Nanometermaßstab immer wichtiger. Hierbei werden funktionelle Materialien auf kleinster Ebene strukturiert. Konventionelle Methoden zur Erzeugung solcher Materialien sind aufwendig und oft sind Vakuumtechnologien oder Wäremebehandlungen nötig.

In der belebten Natur finden sich Prozesse, die funktionelle Materialien unter Umgebungsbedingungen erzeugen. Mit Hilfe organischer Additive wird das Kristallitwachstum eines anorganischen Materials gesteuert. Organische Template führen ebenfalls zu einer gezielten Formgebung. Im Verbund zeichnen sich diese organisch/anorganischen Strukturen beispielsweise durch eine hohe mechanische Festigkeit und gleichzeitig hohe Zähigkeit aus (z. B. bei Perlmutt).

Die Prinzipien der Biomineralisation können auf die Herstellung technisch interessanter Materialien, wie beispielsweise ZnO, übertragen werden. Diese bioinspirierten Verfahren können dazu verwendet werden, die Eigenschaften des Materials gezielt zu beeinflussen.

Diese Arbeit beschäftigt sich mit der bioinspirierten Synthese funktioneller ZnO-Schichten. Im ersten Teil dieser Arbeit konnte gezeigt werden, dass die Oberflächenladung eines organischen Templats dazu genutzt werden kann, das Wachstum von ZnO-Schichten zu steuern. Auf dem reinen, voroxidierten Substrat kann selbst nach 10 Beschichtungszyklen nur Inselwachstum beobachtet werden. Ein unpolares Templat, hier eine fluorinierte selbstorganisierende Monolage (SAM), unterdrückt das Wachstum von ZnO auf

dem Substrat sogar vollständig. Dagegen erfolgt auf den untersuchten polaren Templaten homogenes Schichtwachstum. Deren funktionelle Gruppen können mit den dipolaren ZnO-Kristalliten aus der Lösung wechselwirken. Hierbei gilt, je höher die Oberflächenladung des Templats, desto stärker ist die Wechselwirkung und desto homogener werden die Schichten. Zusätzlich kann auf einer sulfonat-terminierten Polyelektrolyt-Multischicht, dem Templat mit der höchsten hier untersuchten negativen Oberflächenladung, eine 002 Texturierung des ZnO beobachtet werden. Der Einfluss der Template auf das Wachstum schwindet jedoch mit steigender Schichtdicke. Sobald die ZnO-Schicht geschlossen ist, können die ZnO-Partikel aus der Lösung nur noch mit dem bereits abgeschiedenen ZnO wechselwirken. Daraus folgt, dass die Wachstumsrate der Schichten unabhängig vom eingesetzten Templat und dessen Ladung ist. Des Weiteren konnte gezeigt werden, dass ein zu Beginn unpolares Polystyrol-Bürsten-Polymer durch die Abscheidelösung aktiviert werden kann. Eine polare funktionelle Gruppe wird durch eine Reaktion mit dem basischen Lösungsmittel freigelegt. Diese kann anschließend mit den dipolaren ZnO-Kristalliten wechselwirken, was zum Wachstum einer homogenen Schicht führt. Die Wechselwirkung zwischen Templat und Kristalliten ist sogar stark genug, um eine 002 Textur entstehen zu lassen.

Mit Hilfe von Abscheideversuchen aus wässriger Lösung konnte zudem gezeigt werden, dass nicht nur das Schichtwachstum, sondern auch die entstehende Schichtmorphologie kontrolliert werden kann. Hierfür wurde ein strukturiertes Templat aus polaren, amino-terminierten Inseln in einer unpolaren Matrix mit fluorinierten Molekülen eingesetzt. Die ZnO-Partikel in Lösung können sich an die polaren Inseln anlagern. Sie bilden eine homogene Schicht mit geringer Oberflächenrauhigkeit. Auf dem unpolaren Templat dagegen bildet sich eine Schicht mit hoher Rauhigkeit. Hier wird die Oberflächenenergie der ZnO-Partikel durch Agglomeration verringert. Dies führt dann schließlich zu der beobachteten rauhen Schicht.

Im zweiten Teil der Arbeit wurden die piezoelektrischen Eigenschaf-

ten von ZnO-Schichten gemessen, die auf einer COOH-terminierten SAM, einer sulfonat-terminierten Polyelektrolyt-Multilage oder einem Polystyrol-Bürsten-Polymer abgeschieden wurden. In einer ZnO-Schicht mit zufälliger Kristallitorientierung heben sich die piezoelektrischen Verformungen gegenseitig auf. Bei einer 002 texturierten Schicht wirkt die Verformung dagegen immer in die gleiche Richtung und addiert sich zu einem messbaren Wert. Wie im vorherigen Teil gezeigt wurde, beeinflusst die Oberflächenladung des Templats die Textur der abgeschiedenen ZnO-Schicht. Auf diese Weise konnte gezeigt werden, dass durch die Wahl des Templats die Piezoaktivität gezielt eingestellt werden kann. So wird auf der COOH-terminierten SAM eine Schicht mit willkürlicher kristallographischer Orientierung abgeschieden. Daher ist die gemessene piezoelektrische Antwort sehr gering. Auf den anderen beiden Templaten dagegen entsteht eine Schicht mit 002 Textur. Der gemessene piezoelektrische Koeffizient dieser Schichten ist daher gleich hoch oder höher als der von Schichten, die mittels konventioneller Methoden hergestellt wurden.

Der dritte Teil dieser Arbeit beschäftigt sich mit der Entwicklung einer bioinspirierten Methode, um mit Al, Ga oder In dotierte ZnO-Schichten abscheiden zu können. Hierbei hat sich gezeigt, dass das Einbringen der Dotierelemente in die Abscheidelösung das Schichtwachstum beeinflusst. So steigt die Schichtdicke durch Zugabe von Al mit steigendem Dotiergehalt. Dies lässt sich auf das Einbringen von Wasser durch das Aluminiumnitrat Nonahydrat erklären. Das Wasser erhöht die Hydrolysegeschwindigkeit und mehr ZnO wird abgeschieden. Durch die Zugabe von Ga oder In werden die Schichten dagegen mit steigendem Dotiergehalt dünner. Hierbei wird die Abscheidung von ZnO durch eine konkurrierende Ausscheidung von Ga- oder In-Hydroxid behindert. Mit Hilfe der Atomemissionsspektometrie (ICP-AES) und Photolumineszenzmessungen konnte nachgewiesen werden, dass die Dotierelemente in das ZnO-Gitter eingebaut werden. Erstere hat gezeigt, dass weniger Al im Vergleich zu Ga oder In eingebaut wird, was auf

die größere Ionenradiendifferenz zwischen ersterem und Zn zurückzuführen ist. Außerdem zeigen die Photolumineszenzspektren, dass die UV-Bande von ZnO durch den Einbau der Dotierionen verschiebt. Je höher der Dotiergehalt, desto stärker ändert sich die Wellenlänge der UV-Bande. Weiterhin wurden an den ZnO-Schichten mit Ga und In Leitfähigkeitsmessungen durchgeführt. Diese ergaben, dass der Widerstand durch die Dotierung um zwei Größenordnungen geringer ist, als für die undotierte Probe.

Zusammenfassend können die folgenden Schlüsse gezogen werden. In dieser Arbeit wurde gezeigt, dass das Wachstum von ZnO-Schichten durch die geeignete Wahl eines Templates unterdrückt oder gefördert werden kann. Bei Einsatz eines Templates mit hoher Oberflächenladung lässt sich zudem eine 002 Textur erzeugen, die mit einer hohen Piezoaktivität der Schicht einhergeht. Zusätzlich kann durch Dotierung mit Al, Ga oder In die optische Bandlücke und die Leitfähigkeit der ZnO-Schichten gesteuert werden.

1 Introduction

In close relation to the ongoing downsizing of electric products, more and more nanoelectronic devices are fabricated. These devices require structured nanomaterials with specific electrical, optical or piezoelectric properties. To obtain such materials, sophisticated methods are often correlated with high energy consumption or elaborate vacuum technology. Examples for such techniques are radio frequency magnetron sputtering [1, 2], pulsed laser deposition [3] or sol-gel processes with subsequent heat treatment [4].

A new approach for fabricating nanostructured materials can be found in living nature. The nacre of mollusc shells, for example, is produced with the help of biopolymers that control the growth of aragonite crystallites. An organic matrix directs the attachment of the crystallites so that they assemble with a common crystallographic orientation. The composite of the organic matrix and the inorganic aragonite lead to high mechanical hardness in combination with high fracture toughness. [5, 6]

The principles found in nature can be transferred to semiconducting materials for electronic devices. One of these materials is ZnO. It is a semiconductor with a wide band gap of 3.37 eV, UV emission and piezoelectric properties. [7, 8] Bioinspired deposition of ZnO crystallites and films was already achieved by several research groups. Different organic additives in the deposition solution were used to control the crystallite growth of ZnO. [9–15] In other studies, field effect transistors were build with ZnO thin films that were deposited on tobacco mosaic viruses [16] or DNA [17]. Furthermore, artificial nacre could be produced by alternatively depositing

polyelectrolye multilayers and ZnO films [18]. The resulting composite material exhibits a hardness higher than that of a single layer ZnO film.

In this work, Bioinspired mineralization of functional ZnO films is investigated. Different organic templates with amino, carboxy, sulfonate or fluorine functionalities are investigated concerning their ability to support or suppress ZnO growth from solution (chapter 3.1). In addition, ZnO is deposited onto a polymer brush that is activated in the deposition solution (chapter 3.2). In section 3.3, deposition of ZnO onto a structured template of amino and fluorine functionality is performed. In chapter 3.4, the influence of a carboxylate and sulfonate functionality on the piezoelectric properties of ZnO is investigated. In the last part of this work (chapter 3.5) the ZnO films are doped with Al, Ga and In. The growth of these films is characterized as well as their optical and electrical properties.

1.1 Zinc oxide

Zinc oxide is a material with a wide range of applications. Large quantities are used as white pigments (chinese white), as accelerators in rubber vulcanization or as catalysts. Additionally, it shows high UV absorption and is antiseptic, which is why it is found in sunblocking cosmetics and pharmaceutics like creams or plasters. [7, 8] Other applications arise from the field of electronic devices. ZnO was reported to be used as varistor material [7, 8, 19, 20], for gas sensors [7, 8, 21] or as transparent conductive oxide in solar cells [7, 8, 22, 23]. Further research is done on the subject of UV light emitting diodes (LEDs) [7, 8, 24, 25] and field effect transistors (FETs) [7, 8, 16, 17, 26, 27].

These many different applications show that ZnO is a versatile material with interesting properties. In nature, it can be found as red, orange crystals [8]. Its crystal structure is the hexagonal wurtzite structure with the space group $P6_3mc$ and a c/a ratio of 1.602 (figure 1.1).[7] Aside from

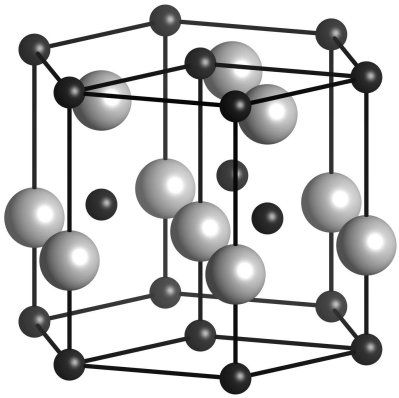

Figure 1.1: Schematic drawing of the ZnO wurtzite crystal structure. Zn and O ions sit on hcp sublattices. [28]

the thermodynamically stable wurtzite, ZnO also has a metastable zinc blende phase (space group $F\bar{4}3m$) that can only grow on cubic substrates. Here, the lattice consists of two interpenetrating fcc sublattices. The third modification is a high pressure phase. The phase transition occurs at about 10 GPa where the crystal structure changes into the more densely packed rocksalt structure (space group $Fm3m$, 17 % volume shrinkage). [7, 8]

Bulk ZnO can be produced in high quality and large quantities. The hydrothermal method is quite common and relatively cheap. A zinc-salt solution is heated in an autoclave to 300 °C to 450 °C under a pressure of up to 2500 bar. Crystal growth is initiated by a thermal gradient and a seed crystal. Another technique is the vapor transport of an evaporated Zn precursor. The deposition takes place at elevated temperatures (1100 °C to 1400 °C) under oxygen or air. ZnO thin films or nanostructures (e. g. ribbons, flower-like structures, pyramids) are deposited *via* metal oxide chemical vapor deposition, molecular beam epitaxy, sputtering, pulsed laser deposition, sol-gel process or chemical bath deposition.[7, 8]

Some of the properties of ZnO can be explained by looking at the crystal structure of the wurtzite phase. The Zn^{2+} and O^{2-} ions sit on interpenetrating hcp sublattices and are tetrahedrally coordinated. Crystal faces perpendicular to the c-axis are terminated by either Zn^{2+} (0001) or O^{2-} ions $(000\bar{1})$. Other faces with the same amount of Zn^{2+} and O^{2-} ions, namely the $(11\bar{2}0)$ and $(10\bar{1}0)$ planes, exhibit a non-polar character. The non-centrosymmetry leads to a polarity of the crystallites and explains the piezoelectric behavior of ZnO (see chapter 1.1.2). [7, 8]

Furthermore, ZnO is not only interesting for its piezoelectric, but also for its electrical and optical properties. ZnO is a II-VI semiconductor with a large band gap of 3.37 eV. It can therefore sustain large electric fields and has a high break-down voltage. Additionally, a high exciton binding energy of 60 meV gives rise to excitonic emission in the UV range, even at room temperature. The source of the second emission band in the green spectral range is still under discussion. Native zinc vacancies V_{Zn} [29], oxygen vacancies V_O[30] as well as Cu impurities [31] are proposed to be responsible for this relatively broad band.

1.1.1 Doping of ZnO

The band structure of ZnO is characterized by an s-like conduction band and a three-fold degenerated p-like valence band. The direct band gap lies at the Γ point of the Brillouin-zone and is 3.37 eV wide. ZnO exhibits n-type conductivity even without doping. The reason for this behavior is still under debate. It was proposed that oxygen vacancies or zinc interstitials could act as donors. But neither simulations nor experiments could confirm the contribution of these defects to the n-type behavior. The unintentional presence of hydrogen interstitials might be more probable. Simulations have shown that these impurities create new states in the band gap of ZnO [32, 33].

The natural n-type conductivity makes it difficult to achieve realiable

p-type doping. Defects like zinc interstitials (Zn_i) and oxygen vacancies (V_O) or hydrogen interstitials (H_i) can compensate the p-type dopants. Additionally, low solubility limits and self-compensation prevent successful doping. Acceptor elements are group I (Li, Na, K) or group V elements (N [34, 35], P, As, Sb [36–39]). From these examples, nitrogen might be the most promising candidate.

n-type doping on the other hand is easily achieved by the incorporation of group III elements like Al, Ga or In [40–42]. They possess one more valence electron than Zn (electron configurations: Zn: [Ar] $3d^{10}$ $4s^2$; Al: [Ne] $3s^2$ $3p^1$; Ga: [Ar] $3d^{10}$ $4s^2$ $4p^1$; In: [Kr] $4d^{10}$ $5s^2$ $5p^1$). When they substitute the Zn^{2+} ions they introduce one excess electron and act as donors. The formation of additional states in the band gap influences the electrical conductivity of the material and the wavelength of the light that is emitted during photoluminescence is shifted. This allows to tune the optical properties of the ZnO by changing the doping content.

To investigate this correlation, the optical band gap can be measured by photoluminescence spectroscopy (PL) (see section 1.4.9). With increasing doping content, the band gap of ZnO is decreased by lowering of the conduction band energy and rising of the valence band energy (figures 1.2a and 1.2b). The UV band of ZnO shifts to lower energies (and consequently to higher wavelengths) with increasing doping content. [43] However, experiments show the opposite behavior for samples doped with Al, Ga or In [44–48]. This can be explained by the Burstein-Moss effect. For higher doping concentrations, the Fermi energy E_F degenerates, i. e. it is lifted into the conduction band of the semiconductor. The states below E_F are occupied. Therefore, more energy is needed for the excitation of electrons from the valence to the conduction band (figure 1.2c). When the optical band gap is measured in this case, it seems as if the band gap increases with higher doping content. Consequently, the bands in the PL spectra show a blue shift.

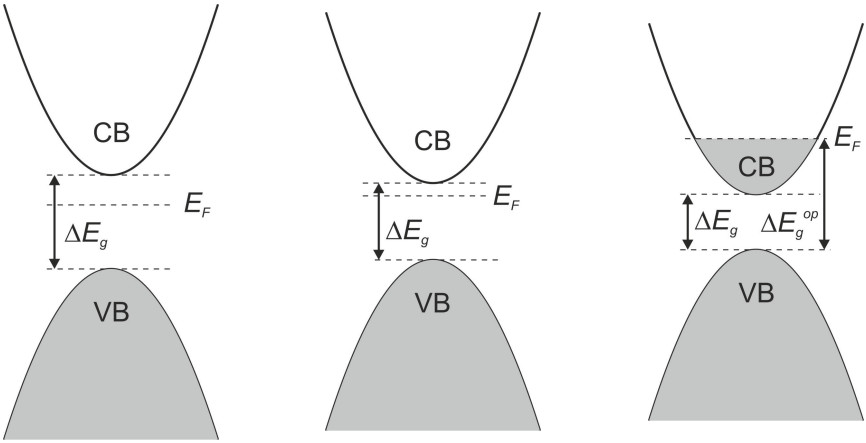

Figure 1.2: Schematic drawing of the band structure of a) natural n-type ZnO, b) lightly doped n-type ZnO and c) a degenerated semiconductor with the band gap ΔE_g showing the Burstein-Moss effect. The Fermi energy E_F is lifted into the conduction band (CB). The energy that is necessary to excite an electron from the valence band (VB) into the CB is ΔE_g^{op} and is higher than the actual band gap ΔE_g. Therefore, the band measured in PL shows a blue shift.

1.1.2 Piezoelectric effect of ZnO

ZnO is a piezoelectric material due to its wurtzite crystal structure and dielectric properties. The piezoelectric effect causes a polarization of the crystal when a mechanical stress is applied. In contrast to ferroelectrica, the polarization is non-permanent and cannot be switched by inversing the direction of the mechanical stress. The inverse piezoelectric effect can be observed, when a voltage is applied and the material shows a mechanical deformation.

The extent of deformation Δz and the applied voltage V are correlated *via* the tensor *d*. Equation 1.1 describes the response of a ZnO sample that is oriented along the crystallographic c direction to an electric field applied in the same direction [49]:

$$\Delta z = d_{33}V + \frac{M_{333}}{t}V^2. \tag{1.1}$$

The piezoelectric deformation for this case is given by the corresponding tensor element d_{33} times the applied voltage. The latter part of the equation describes the second order response of the system. This so-called electrostrictive effect (M_{333} is the electrostrictive coefficient) describes a deformation that is independent of the direction of the electric field. It occurs in all dielectrics and is not restricted by crystal symmetry. M_{333} is much smaller than d_{33} and scales with the sample thickness t. Kornev et al. [50] calculated a value for M_{333} of $-3.6 \times 10^{-22}\,\mathrm{m^2\,V^{-2}}$ for ZnO.

For ZnO with hexagonal crystal symmetry, the piezoelectric tensor has three independent components, d_{33}, d_{13} and d_{15}:

$$d_{ij} = \begin{pmatrix} 0 & 0 & 0 & 0 & d_{15} & 0 \\ 0 & 0 & 0 & d_{15} & 0 & 0 \\ d_{31} & d_{31} & d_{33} & 0 & 0 & 0 \end{pmatrix}. \tag{1.2}$$

The values for the coefficients are high compared with other wurtzite-structure materials. Depending on the type of material, different values for d_{33} are found in literature: 12.4 pm V^{-1} for bulk ZnO [51, 52] and 2 pm V^{-1} to 13 pm V^{-1} for ZnO thin films and nanobelts [1, 4, 53]. Compared to two materials regularly used as reference samples for piezoresponse force microscopy (PFM) measurements, namely periodically poled lithium niobate (PPLN) (7.11 pm V^{-1}[51]) and x-cut quartz (around 2.2 pm V^{-1}[51, 52]), these values are in the same range.

1.2 Bioinspired Mineralization

1.2.1 Basic Principles

The methods to produce ZnO as described in section 1.1 either require special reaction conditions (vacuum or high pressure, elevated temperatures) or an annealing step (e. g. sol-gel process). On the other side, nature proves that it is possible to create highly functional materials under mild conditions (i. e. near room temperature, atmospheric pressure, aqueous medium). Mollusc shells for example consist of nacre, a material with high hardness and high fracture toughness. Bones and teeth withstand high strains and magnetic particles in bacteria provide means for orientation along the earth's magnetic field. In all these cases, the materials used are adapted to fit the challenges of their specific area of application (for more examples, see e. g. [5, 6, 54]).

To be able to produce such a variety of forms and functions, biology resorts to the combination of inorganic with organic components. The organic phase plays the role of a so-called template. On the one hand, the template consists of polymeric molecules that form a scaffold for the deposition of the inorganic material. On the other hand, it can also consist of soluble species that interact with the inorganic phase in solution. In both

cases, the template allows control over the formation, shape and deposition of the inorganic crystallites and therefore the properties. [6, 55]

In this context, it is important to know about the crystallization processes in solution and how they can be influenced by organic additives. The classical theory of nucleation and growth of crystallites is a purely thermodynamic treatment. The formation of stable nuclei is governed by the interplay of the free energy won through the phase transition ΔG_v and the energy needed to create the new surface ΔG_s:

$$\Delta G = \Delta G_\mathrm{s} + \Delta G_\mathrm{v} = 4\pi r^2 \gamma + \frac{4}{3}\pi r^3 \frac{\Delta g_\mathrm{v}}{V_m}. \tag{1.3}$$

Here, r is the cluster radius, γ is the surface tension, Δg_v represents the free energy per mole associated with the solid-liquid phase change, and V_m is the molar volume. [56] Cluster formation is induced by a driving force, like supersaturation in solution or a temperature gradient. The clusters can grow if they reach the critical radius r^* that is marked by a maximum in ΔG, else they will dissolve. Particles with a radius larger than r^* grow by ion attachment. The final crystal shape is then determined by the surface energies of the different faces. The fraction of high energy surfaces will be reduced, while the one of low energy surfaces increases. [56]

However, it was found that there is another pathway for precipitation, that is called "non-classical" crystallization. Here, the mineralization is kinetically hindered and the final, stable phase is only reached *via* a series of intermediate, metastable phases (Ostwald's step rule). The intermediates can be either amorphous or crystalline, but the energy needed for their formation is smaller than for the direct precipitation of the stable phase (*cf.* figure 1.3). [55, 57]

In this mechanism, the presence of additives is a crucial factor. First, the additives can stabilize the intermediate phases by adsorption, for example. Second, it is known that organic molecules can adsorb to specific crystal

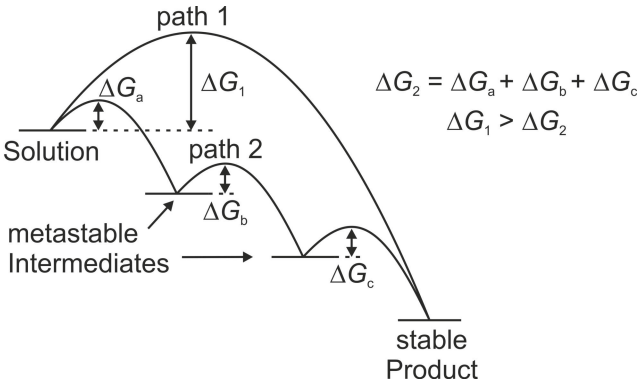

Figure 1.3: Energy diagram of a mineralization process demonstrating Ostwald's step rule. Path 1 shows the direct transformation of the dissolved species into the stable solid phase. If path 1 is kinetically hindered, precipitation of one or more metastable intermediate phases (amorphous or crystalline) occurs. The energy needed for the step wise transformation (path 2) is lower than for path 1. (adapted from [55])

faces and inhibit their growth. The resulting crystal shape can change drastically.

Growth of the so formed nanocrystals is then also different from the classical way. Instead of ion-by-ion growth to a single crystal, the nanoparticles can aggregate to form a so-called mesocrystal. The driving force for the aggregation is the reduction of free surface energy. High energy faces can disappear by fusing two or more crystallites with the same orientation ("oriented attachment"). The resulting mesocrystal cannot be distinguished easily from a single crystal due to the common orientation of the crystallites. Here again, additives play an important role in the morphology control. [6, 55]

In biomineralization, the non-classical pathway is quite common. With the help of highly specialized organic molecules, the crystallization of the inorganic material can be controlled. To adapt the principles of biomineralization to materials of technical interest is therefore a growing topic in research. Complex structures of materials like silica, hydroxyapatite, titania or silver have been produced by several research groups [58–63].

1.2.2 Bioinspired synthesis of ZnO

ZnO is a material that can be produced in a variety of structures by bioinspired mineralization, depending on the additives in solution [13, 64–66]. Recently, Lipowsky et al. investigated the deposition of ZnO from methanolic solution [18, 67–69]. The system is similar to the one used in this work (section 2.2.1). They chose polyvinylpyrrolidone (PVP) (figure 1.4a) and tetraethylammonium hydroxide (TEAOH) (figure 1.4b) as additives and methanol (MeOH) as solvent. The latter was used due to its low rate of hydrolysis. In water, the hydrolysis reaction would be too fast and no film could be deposited. [69] TEAOH was added to elevate the pH of the solution. According to the results of Reichle et al. [70], at pH values of 8 to 9, soluble zinc hydroxide species are stable that promote ZnO deposition.

Lipowsky et al. performed particle size measurements over the reaction time and could identify three stages that lead to the formation of ZnO. The first stage starts with the mixing of the solutions and ends after heating to 60 °C. Here, depending on the PVP content, they found either no particles, an amorphous or an already crystalline phase containing ZnO and $Zn(OH)_2$. In the second stage, after heating, those particles dissolved and amorphous spicules, probably consisting of $Zn(OH)_2$ and/or ZnO, were present. The elongated growth of these particles is mediated by PVP molecules that are incorporated into the spicules. In the last stage, that describes the long-time behavior, the amorphous precursor particles transform into crystalline ZnO. [68] The particles deposit in an oriented way, directed by a polar template (SO_3H-terminated self-assembled monolayer) onto a substrate. The result is a homogeneous film with a 002 texture. For reaction times longer than 90 min the nanocrystallites start to agglomerate in solution and those agglomerates sediment onto the substrate. [68, 71]

As already mentioned in the previous paragraph, the third additive, PVP, has a pronounced influence on this mineralization process. Lipowsky et al. investigated the precipitation behavior of solutions containing no, intermediate or high amounts of PVP [68]. Without polymer in solution, they found that there are already crystalline particles consisting of ZnO and $Zn(OH)_2$ present in the first stage. These rod like particles disintegrate into ZnO nanoparticles that grow very fast. Since all ZnO is agglomerating, no film can be formed on the substrates. [68, 72]

In the opposite case of a very high PVP content in solution, Lipowsky et al. found no particles in neither of the stages. This leads to the conclusion that high quantities of the polymer prevent crystallization. Indeed, experiments with intermediate PVP concentrations show the behavior described above, while the particle size decreases with increasing PVP concentration. [68]

Therefore, Lipowsky et al. stated that the PVP molecules intertwine in solution, forming a network. Like this, the intermediate, amorphous phase

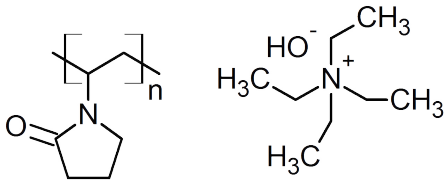

(a) (b)

Figure 1.4: Structural formulas of the additives (a) polyvinylpyrrolidone and (b) tetraethylammonium hydroxide.

is stabilized and Zn^{2+} ions are slowly released to form ZnO. [68]

1.3 Templates

For the preparation of electronic devices, it is necessary to create functional structures with dimensions in the nm-scale. Lithography methods are often used to deposit or etch away material in a site-selective manner. This requires several steps (e. g. preparation of a mask, etching, depositing) and highly specialized equipment.

To simplify this production process, it would be interesting to deposit structures of a semiconductor material with optimized properties in a one-pot synthesis. For this, it is necessary to provide structures onto which the material can be site-selectively deposited. A variety of organic templates can be used to modify the surface properties of a substrate in a way to promote or inhibit the attachment of crystallites from solution. Likewise, the templates can also influence the properties of the resulting thin films (as will be shown in chapter 3.1.2). In this chapter, different organic molecules are presented that can be used for the mineralization of ZnO.

1.3.1 Self-assembled monolayers

Surface functionalization can be achieved in different ways. Molecules for self-assembled monolayers (SAMs) consist of an anchoring group, a hydrocarbon chain and a functional end group. The latter is responsible for the properties of the modified surface. Functional groups like amines, carboxylates or sulfonates are polar and lead to hydrophilic behavior. Hydrophobic surfaces on the other hand can be achieved by molecules with methyl or fluorine termination.

The molecules are attached to a substrate surface *via* the anchor group. [73, 74] Binding to the substrate is highly specific. Thiols, for example, are used to modify gold surfaces [75], whereas silanes are binding to Si substrates [76, 77]. During adsorption, the molecules arrange in an ordered way. The interaction between the chains defines the distance and orientation of the molecules [75–78]. SAM formation thereby resembles phase transformations. In the beginning, only few molecules are adsorbed to the surface and ordering is very low. The chains are partially lying flat on the substrate and therefore, this state is called "vapor". With increasing density, several intermediate phases can occur. Sometimes, there is a so-called "liquid phase". Here, the molecules start to reorientate themselves and a short-range order is achieved. There might also be other configurations, like liquid-crystalline or "striped". In the end, all molecules stand upright, normally tilted by an angle. Due to the highly oriented state of the molecules, this phase is called "solid". However, how the evolution of completely dense monolayers is going on is still under discussion. [79, 80]

Their ordered structure and functionalization make SAMs versatile templates for the deposition of ceramic materials. In the past years, there were several groups investigating the influence of different surface functionalities on the mineralization behavior of ZnO. In some studies, the ZnO particles preferentially grow on polar templates due to electrostatic interactions. [81–86]. Others report that molecules from the deposition solution adsorb

to the ZnO crystallites and lead to hydrophobization of the crystallite faces. In these cases, attachment of the particles onto non-polar functional groups is favored. [86–88]

For a better comparison of the deposition behavior on polar and non-polar surfaces, patterned substrates are used regularly. There are various techniques to produce contrasting structures of two SAMs with different endgroups. Two elaborate methods to create distinct structures are micro contact printing or UV photopatterning. For the first, a polymer stamp is used to transfer SAM molecules onto a substrate [83, 88–90]. For the other, a mask covers parts of the already SAM-covered template. A chemical modification is accomplished by illuminating the substrate with UV light [18, 85, 87]. Another possibility to get structured surfaces is using polymer blend lithography (figure 1.5). Two incompatible polymers are spin cast onto the substrate. During solidification, phase separation occurs. Under optimized conditions, a reproducible island-matrix structure is achieved. One of the polymers can then be dissolved selectively and the now free substrate surface areas can be coated with one SAM molecule. Afterwards, the second polymer can be removed with a suitable solvent or by CO_2 snowjet and another SAM can be deposited. [81, 91–93] This leads to the formation of islands of one SAM in a matrix of the other SAM. The deposition onto these functional patterns can then be investigated.

1.3.2 Polymer brushes

Aside from SAMs, substrates can be functionalized by polymer brushes. Similar to SAMs, they can be structured with different techniques [86, 94, 95]. Polymer brushes form a covalent bond to the substrate surface. Depending on the chemical nature of the polymers, the grafting density and the solvent, the polymer molecules can adopt different conformations. In a poor solvent at low grafting densities for example, the molecules collapse and form a "pancake" structure (figure 1.6a). Increasing the grafting density leads to

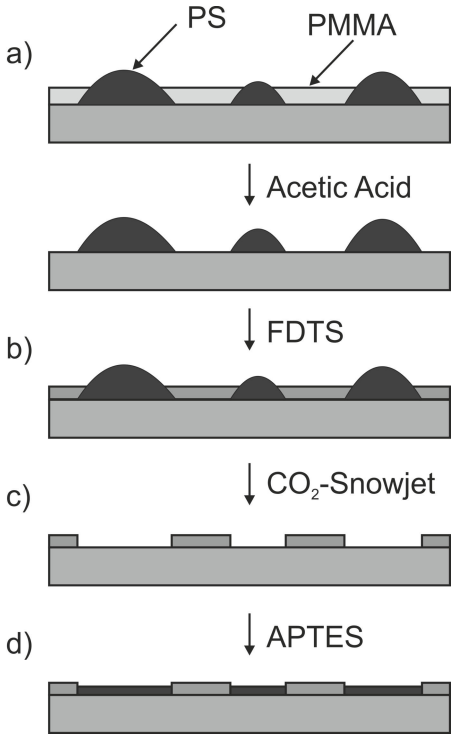

Figure 1.5: Schematic representation of the polymerblend lithography process. a) Two polymers, here, Polystyrene (PS) and Polymethylmethacrylate (PMMA) are phase separated during spin casting and one of them is selectively dissolved. b) The holes are then covered with one SAM molecule type, here FDTS. c-d) The second type (APTES) is deposited after dissolving the second polymer. (adapted from [81])

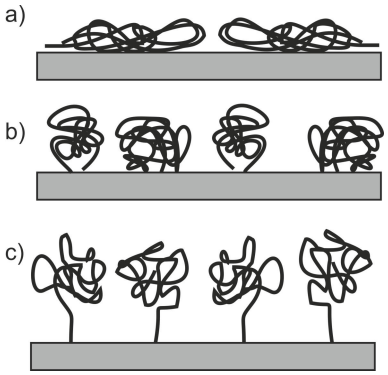

Figure 1.6: Depending on the chemical sorroundings and the grafting density, polymer molecules in a brush show different conformations. a) The polymer molecules collapse in a poor solvent at low densities. b) At higher densities, pinned micelles are formed. c) In a good solvent and low densities, the molecules are in equilibrium configuration. With increasing density, the molecules are forced to stretch away from the surface. (adapted from [96])

the formation of pinned micelles (figure 1.6b). In a good solvent on the other hand, the molecules can adopt an equilibrium conformation ("mushrooms", figure 1.6c). In the presence of more molecules, the individual chains start to repel each other, forcing the chains to stretch away from the substrate to prevent overlapping. Ultimately, a dense polymer brush is achieved (figure 1.6d). Depending on the state the brush is in, not only a functional end group but the chemical nature of the complete chain determines the properties of the deposited polymer brush. [96]

To pin the individual molecules to the surface, two different approaches can be distinguished. The first one is the so-called "grafting from" method. In this case, an initiator is attached to the substrate and the substrate is immersed in a monomer solution. The initiator then starts a polymerization reaction (e. g. polycondensation, radical or ionic polymerization). [96–98]

The second method is named “grafting to”. Here, the already polymerized molecules bind covalently to functional groups at the substrate surface. [99–101] In this work, a vinyl-terminated brush is attached to surface silanol groups of a silica substrate. Maas et al. assumed that the vinyl group first transforms into an alcohol and then reacts with a silanol group to form an ether bond (see chapter 3.2). Since they used water-free chloroform as solvent, they propose that the water necessary for the hydroxylation of the vinyl comes from condensation reactions of the silica surface. [101]

1.3.3 Polyelectrolyte multilayers

Multilayer systems consisting of an inorganic phase (e. g. alumina, titania or ZnO) and an organic phase (e. g. polyelectrolytes) are prepared to achieve enhanced mechanical properties of thin films. The organic phase guides the mineralization of ceramic particles (see section 1.2). Lipowsky et al. found in their work that a composite material of poly(amino acids) and ZnO leads to higher hardness compared to a bulk ZnO sample. [18] Additionally, X-ray diffraction (XRD) measurements showed a preferred orientation along the (002) direction of the ZnO crystallites. This texture is a prerequisite for macroscopically piezoactive ZnO films (see section 1.1.2). Therefore, the deposition of ZnO onto polyelectrolyte (PE) multilayers will be investigated in this work.

PE multilayers consist of polycations and polyanions that are alternately deposited on a substrate. In a simple layer-by-layer procedure, the substrate is immersed in a solution containing one of the polymers (figure 1.7). After a washing step, the substrate is dipped into the second polymer and subsequently washed. The film thickness can be determined by the number of deposition cycles. During the washing steps, residual polymer is removed and adsorbed molecules are rearranged to form more stable bonds. [102–104]

The most important driving force for the film formation is electrostatic

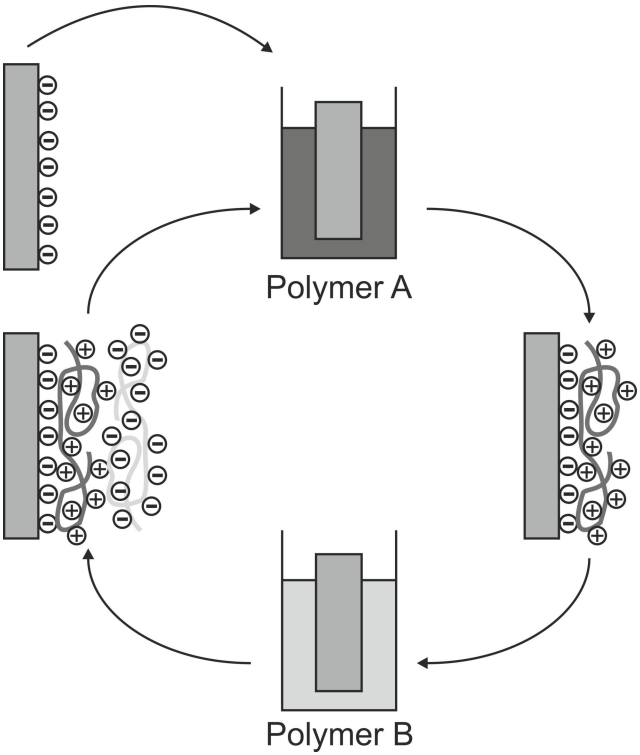

Figure 1.7: For the layer-by-layer assembly of polyelectrolyte films, a substrate is immersed in a solution of polymer A. In general, polymer A should be oppositely charged compared to the substrate. In this scheme, the substrate is negatively and polymer A is positively charged. Adsorption takes place due to electrostatic interactions. The next polymer layer is added by dipping the substrate into a solution of polymer B (negatively charged). The deposition can be repeated several times to increase the film thickness. In-between the dipping steps, the substrate is washed to form more stable bonds and remove contaminants.

interaction. The polymer molecules are attracted by the oppositely charged substrate. When the surface is completely covered, adsorbed molecules repel molecules in solution with the same charge. This prevents further layer growth. By exchanging the polymer with another, oppositely charged polymer, a second layer starts to grow. Here again, bonds between positive and negative charges are formed and stabilize the film.

Depending on the nature of the used PE molecules, the pH and the ionic strength of the solution, the structure of the multilayers can be influenced. For strong PE with a high charge, stable multilayers can be fabricated independent of the pH. The charge density of weak PE on the other hand is highly dependent on the pH of the solution. There is a critical charge density below which no stable layer can be formed since the electrostatic attraction is too low. At the same time, a high charge leads to repulsion of segments within a single molecule, i. e. the chain is stretched and quite stiff. With a lower charge density, the PE molecule becomes more flexible and can adopt different conformations. When these coiled molecules adsorb to the substrate, a thicker layer is formed. Additionally, the different PE layers can overlap. Another parameter that influences PE adsorption is the ionic strength of the counter ions in solution. A high ionic strength leads to screening of charges along the polymer chain. These screened charges do not repel each other anymore and the molecule can adapt more conformations, i.e. it is more flexible. Furthermore, the screening also decreases the total charge of the polymer. Consequently, during deposition of a PE multilayer, more molecules are necessary to compensate the charge of the underlying PE layer. [102–104]

For the deposition of a mineral phase, the ζ-potential of the PE multilayers is important, which was found to be only dependent on the charge of the uppermost layer. Dejeu et al. [105] and Hoogeveen et al. [103] measured the ζ-potential after each deposition step during multilayer formation of poly(allyl amine)/PSS and poly(vinylimidazole)/poly(acrylic acid),

respectively. The ζ-potential changes from positive to negative values and back. In the case of charge compensation, the surface potential should be zero. Therefore, if the newly measured potential is below or above zero, the charge on the surface overcompensated by the next polymer layer.

1.4 Methods

1.4.1 Water contact angle measurements

When a droplet of water is in contact with a solid surface, the area that is covered by the droplet is determined by the surface and interface energies (γ) of the system (figure 1.8a). For a hydrophilic surface, it is more favorable to form an interface between the water (l) and the solid (s) than to maintain the solid/air surface. The droplet therefore spreads over a large surface area (figure 1.8b). In the case of a hydrophobic surface, the interaction between the solid and air (v) is preferred over the solid/liquid interaction. The result is a droplet with a high contact angle to minimize the interfacial area (figure 1.8c). In total, the correlation between contact angle θ and interfacial energies is described by the Youngs equation [106]:

$$\gamma_{\mathrm{sv}} = \gamma_{\mathrm{lv}} + \gamma_{\mathrm{ls}} \cos\theta \tag{1.4}$$

1.4.2 Zeta potential

Surface charges are not only responsible for the formation of PE multilayers (see section 1.3.3). They are also involved in the interaction of the organic template with polar particles during mineralization of an inorganic phase. By measuring the ζ-potential one gets information about the surface potential of the template.

There are two possible mechanisms for the formation of a charged sur-

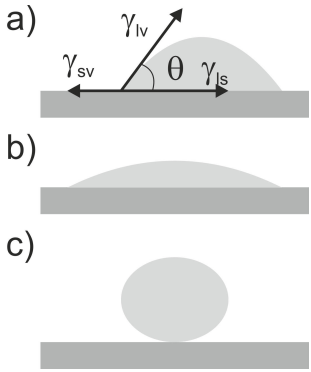

Figure 1.8: Schematic representation of a droplet on a) a hydrophilic and b) a hydrophobic surface. c) The interfacial energy between the solid (s), liquid (l) and vapor (v) phases determine the contact angle θ.

face in a dispersion medium: Protonation or deprotonation of dissociable functional groups or adsorption of charged species. The latter is dominant for non-polar materials. In the first case, the evolution of the potential can be described by the model of Gouy, Chapman, Stern and Grahame [107]. Figure 1.9 shows the example of a negatively charged surface in a dispersion medium. Near the surface, a fixed double layer of ions is formed (Stern layer). An inner layer (inner Helmholtz layer) of anions is bound to the surface. The solvation number of anions is lower than that of cations. Therefore, their hydration shell is smaller and the ions can more easily approach the surface. Short range van der Waals forces prevail over the electrostatic repulsion. Due to the strong binding, the ions loose their hydration shell. [108] The outer Helmholtz layer is formed by electrostatically attracted, positively charged counterions. Due to their hydration shell, there is a maximum number of ions that can adsorb to the surface. It is therefore not possible that the surface charge is compensated completely by the Stern layer. More counterions are accumulated in a loosely bound

layer ("diffuse layer"). The concentration of counterions decreases with increasing distance to the surface, until the concentration is equal to the concentration of anions. Figure 1.9 also shows the evolution of the potential. It first increases linearly due to the inner Helmholtz layer and then decreases linearly in the outer Helmholtz layer. In the diffuse layer, an exponential decrease can be found. [107–110]

A part of the diffuse layer can be removed by shear stresses, when the surface is moved in solution or the solvent streams along the surface. Then, the surface charge is not compensated completely anymore and a residual potential, the ζ-potential, can be measured. The faster the movement, the more of the layer is removed and the potential that remains increases (figure 1.10). Since the Stern layer is strongly bound to the surface, it cannot be removed. Therefore, the highest potential that can be measured is ZP_S. [107–110]

Surface charges of particles can be determined by electrophoresis. Here, the particles are moving in an electric field. Then, the ζ-potential can be calculated from the particle velocity and the applied electric field. [109–111]

For substrates, streaming potential or streaming current measurements are performed. [110–112] An electrolyte solution is pressed through a rectangular cavity of around 100 nm in width between two samples. This stream drags along ions from the diffuse layer. Essentially, this corresponds to the movement of a particle in a medium. The result is a streaming current I_{stream} that can be measured in dependence on the applied pressure. The ζ-potential can be is related to I_{stream} *via* the Helmholtz-Smoluchowski equation:

$$I_{\mathrm{stream}} = \frac{\epsilon\zeta}{\eta}\frac{\Delta p}{L}A \tag{1.5}$$

with the dielectric constant ϵ, the viscosity η, the pressure difference Δp, the channel length L and the sample area A. The measurement is performed by increasing the pressure in the cavity and simultaneous measurent of

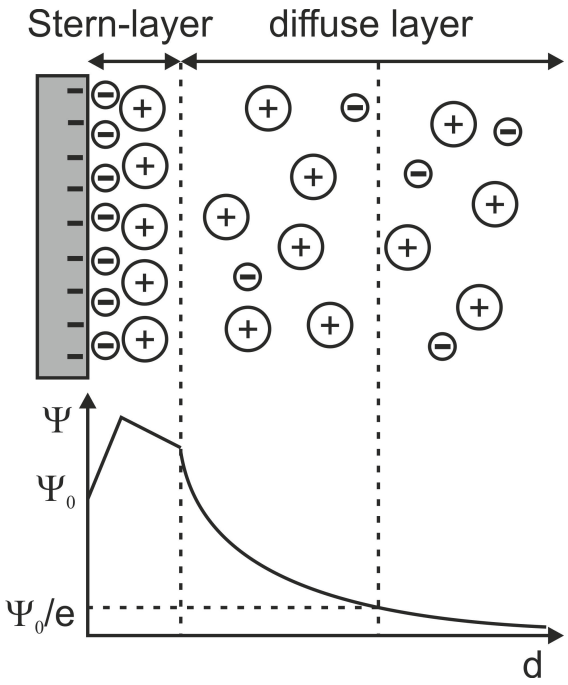

Figure 1.9: The charge of a substrate is compensated by counterions in solution. The scheme shows the ion distribution in dependence on the distance to the surface and the evolution of the potential. A fixed double layer (Stern layer) is formed by ions bound to the surface by electrostatic and van der Waals forces. To completely compensate the surface charge, loosely bound ions are accumulated in a diffusive layer. This layer can be removed by shear forces and an effective charge remains unbalanced. This so-called ζ-potential can be measured by e. g. electrophoresis or streaming current measurements. (adapted from [108])

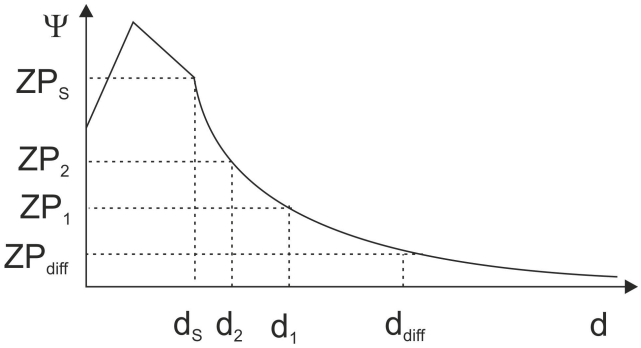

Figure 1.10: If a particle moves in the solution or if the solvent streams along the surface, part of the diffuse layer is removed. The faster the movement is, the higher are the shear stresses and the more of the diffuse layer is lost. Consequently, the ζ-potential increases until it has reached the Stern potential of the Stern-layer. (adapted from [108])

the streaming current. According to equation 1.5, the ζ-potential can be calculated from the slope of the curve when plotting I_{stream} against Δp. [109–112]

The surface potential depends, amongst others, on the pH of the solution (figure 1.11). In the shown example, the surface is positively charged due to protonation of functional groups. At higher pH, the functional groups are deprotonated and a negative charge is the result. The pH value at which the surface seems neutral is called isoelectric point (IEP). Additionally, figure 1.11 shows the ζ-potential curves for highly acidic (e. g. with sulfonate functionality) or basic (e. g. with amino functionality) surfaces.

In the case of surfaces without dissociable groups, the measured ζ-potential is caused by the adsorption of ions to the surface. They exhibit an IEP that typically lies at a pH value of around 4. [112]

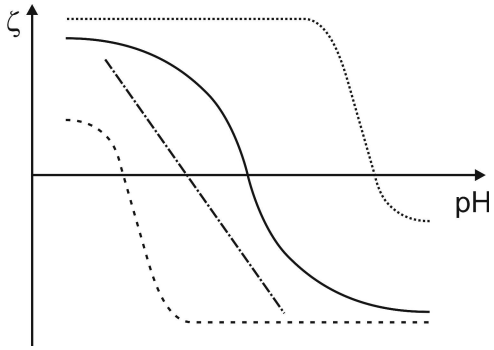

Figure 1.11: The diagram shows the ζ-potential against pH of materials with different functional groups (amphoteric: solid; acidic: dashed; basic: dots; non-polar: dot-dash). (adapted from [112])

1.4.3 Infrared Spectroscopy

Molecules can vibrate or rotate when they are irradiated with infrared light. This causes a change in the bond lengths and angles. Depending on the adsorbed energy, different atomic groups or vibration modes can be excited. For infrared spectroscopy (IR), the sample is mounted in an interferometer and exposed to a pulse of infrared light. The intensity is measured after transmission through the sample by a detector. The adsorption spectrum can be calculated *via* Fourier transformation. Absorption bands in the spectra can be correlated to specific vibration modes. [113]

There are different techniques available for varying sample types. For analysis of surfaces or powder samples, attenuated total reflection (ATR) measurements can be carried out. Here, the sample is pressed against a medium with high refractive index, e. g. a diamond crystal. The beam is transported through the medium at an angle higher than the total reflection angle. Due to interactions with the sample, an evanescent wave is created and the intensity of the beam is lowered. This can be analyzed and the adsorption spectrum can be used to identify the occuring bands. [114–116]

Measurements of thin films can be improved by so-called infrared reflection absorption (IRRA) measurements. The film is deposited onto a substrate with metal coating. The beam is reflected at the film/metal interface and then detected. The pathway of the beam is twice as long as for transmission and can even be prolonged by using a grazing incidence setup. This enhances the signal to noise ratio. [116]

1.4.4 Atomic force and Piezoresponse force microscopy

The atomic force microscopy (AFM) technique allows the characterization of a surface with high lateral resolution. [117–120] A sharp tip mounted on a cantilever interacts with the sample surface. In case of a height change or a modified interaction, the cantilever motion is changed. This can be detected by a laser beam that is first directed to the backside of the cantilever. The reflected beam then impinges on a four-field photodiode. Any movement of the cantilever results in a deflection of the laser on the diode and a change in the photocurrent. By calibration, the difference in the voltage in mV can be converted into a distance in nm. The sample itself is placed on a sample holder that can be moved with piezoelectric transducers. This allows a scanning of a certain surface area and localized informations can be translated into a 2D or 3D image.

Contrast formation is achieved by changing the interaction between tip and sample surface. The system can be operated in different modes. One of them is the contact mode, where the tip is in direct contact with the sample surface at a constant force. A change in the sample height causes the cantilever to bend, which can be detected *via* the laser. A feedback loop ensures that the default force is reestablished. [118, 120, 121] Another possible operation mode is the so called “tapping” mode. In this case, the cantilever vibrates at its resonance frequency and a certain amplitude. By lowering the tip to the surface, the amplitude is dampened till a setpoint value is reached. A height change results in a change in amplitude, which

again can be detected by the laser. Additionally, a shift in the phase signal can be evaluated. [118–120, 122]

With AFM, it is possible to measure various sample properties. Most obviously, a detailed topography image is obtained. In contact mode, there is also the possibility to measure the friction of the surface, while the phase shift in tapping mode contains information about elastic properties. Additionally, the localized electrical and magnetic properties can be analyzed by applying a conductive or magnetic tip in contact mode. [123]

A special case of AFM measurements is the PFM mode. Here, the piezoelectric properties can be measured by applying a voltage between a conductive AFM tip and the sample. Due to the inverse piezoelectric effect, the sample will expand or retract. The cantilever is in contact with the surface and follows the deformation. The movement is detected by the AFM laser. Additionally, the sample can exhibit shear deformation due to the contribution of d_{13} (see equation 1.2 in chapter 1.1.2). This causes torsion of the cantilever and can also be used to investigate the polarization of the individual domains [2, 124]. By scanning a surface area, a map of the piezoelectric response can be compiled. [125–127]

A disadvantage of using the tip as top electrode is the highly inhomogeneous electric field that is generated. The excitation is localized to only a small volume. The material around this area does not deform and a clamping of the excited volume is the result. For this case, Kalinin et al. [128] found a correlation between the measured d_{eff} and real d_{33} of

$$d_{33} \approx 2d_{\text{eff}}. \tag{1.6}$$

To create a more homogeneous field, it is possible to coat the sample with a conductive material (e. g. gold) as top electrode. The disadvantage here is first, the low lateral resolution of the measurements. Second, the top electrode might hinder the movement of the underlying grains. This

clamping would lead to a decrease of the measured response. [129]

To improve the detection, an alternating current is used instead of a direct current. This leads to a vibration of the sample surface. The response is resolved with a lock-in amplifier into an amplitude and a phase signal. After calibration, the amplitude corresponds to Δz in equation 1.1. The phase signal contains information about the orientation of the polarization[1].[125–127]

For quantitative evaluation, the drive amplitude V_ω of the alternating current $V_{\mathrm{AC}} = V_{\mathrm{DC}} + V_\omega \cos \omega t$ is varied. The response can be calculated by inserting $V = V_{\mathrm{AC}}$ in equation 1.1 [49]:

$$\Delta z_\omega = d_{\mathrm{eff}} V_\omega + 2 \frac{M_{333}}{t} V_{\mathrm{DC}} V_\omega. \tag{1.7}$$

If the measured response is plotted against the drive amplitude, d_{eff} can be calculated from the slope of the linear curve. The interception with the y-axis should be zero (no applied voltage, no deformation). In reality, the interception is often higher due to a background signal. This signal arises from the electronic circuit of the AFM setup. It can be measured with a non-piezoelectric sample, like an amorphous glass slide. Here, the value of $\Delta \mathrm{z}_\omega$ should be independent of the applied voltage [130, 131].

Additionally, the electrostrictive part of the response can be measured at the second harmonic frequency 2ω [49]:

$$\Delta z_{2\omega} = \frac{M_{333}}{2t} V_\omega^2. \tag{1.8}$$

Plottet against the drive amplitude, the values for $\Delta \mathrm{z}_{2\omega}$ follow a parabolic shape and should be much lower than the values for $\Delta \mathrm{z}_\omega$. If this is not

[1] It has to be kept in mind that a complete reconstruction of the orientation is only possible, if the response is measured in x-, y- and z-direction. First, the response is measured in x- and z-direction. Due to the asymmetry of the cantilever, the sample has to be rotated by 90° to obtain the in-plane response in y-direction. [2, 124]

the case, then the sample is not piezoelectric and the electrostrictive part dominates the behavior.

1.4.5 Scanning electron microscopy

Since its invention in the 1930s, scanning electron microscopy (SEM) became a versatile tool for sample characterization. An electron beam is generated from a cathode. It is focused and rastered over the sample by an electromagnetic lens system. The electrons can interact with the sample material in different ways. Aside from X-ray emission, electrons can be scattered and ejected. Depending on the working current, the interactions take place in a volume under the surface. In most cases, so-called "secondary electrons" from inelastic scattering events are used for contrast formation in SEM. These secondary electrons can be detected depending on the position on the sample surface. The more electrons are emitted, for example at edges or corners, the higher the intensity will get. The result is a image with three-dimensional appearance of the sample surface. [132, 133]

1.4.6 X-ray diffraction

Structure analysis of crystalline samples can be performed with the help of X-rays. The radiation is diffracted at the lattice planes of the crystallite. Waves diffracted at different, parallel lattice planes can interfere with each other due to a difference in path length. Under certain angles θ, the diffracted waves with a wavelength λ undergo constructive interference. Bragg's equation describes the correlation between wavelength, the lattice distance d and the angle of incidence for different diffraction orders n [134]:

$$n\lambda = 2d \sin\theta \tag{1.9}$$

In Bragg-Brentano geometry, the sample is placed in the center of a goniometer circle. The X-ray source and the detector are moved along this circle. The angles between source and sample and sample and detector are equal (θ-2θ method). [135] A setup of lenses is used to focus the beam on the sample. A monochromator filters the radiation to ensure that the sample is illuminated with one single wavelength. During the measurement, the angle of incidence is varied continuously. If Bragg's law (equation 1.9) is fulfilled, there is constructive interference and the diffracted beam can be detected. A plot of the intensity against 2θ gives the so-called diffraction pattern. From the position of the reflections one can calculate the lattice parameters of the sample and thus the crystal structure can be determined. Deviations in the relative intensities $I(hkl)$ of the samples in comparison with those of a reference powder sample $I_0(hkl)$ can be quantified *via* the so-called texture coefficient $T_\mathrm{C}(hkl)$: [136]:

$$T_\mathrm{C}(hkl) = \frac{\frac{I(hkl)}{I_0(hkl)}}{\frac{1}{n}\sum_n \left(\frac{I(hkl)}{I_0(hkl)}\right)} \tag{1.10}$$

The parameter n is the number of all reflections taken into account. The texture coefficient of powder samples with random crystal orientation is around 1. For samples with a texture coefficient $T_\mathrm{C}(hkl)$ higher than 1, there is a preferred crystallite orientation in the corresponding hkl direction.

Furthermore, the broadening of the diffraction lines (the integral breadth $\beta_{2\theta}$ can be correlated to the crystallite size D of polycrystalline samples. They can be calculated by Scherrer's equation [137]:

$$D = \frac{K\lambda}{\beta_{2\theta}\cos\theta} \tag{1.11}$$

with the shape factor K.

For polycrystalline samples, the crystallites vary in size. Therefore,D

is also called the volume weighted mean column height. The values of D obtained with Scherrer's equation correspond to an approximation to the crystallite size. [138, 139]

1.4.7 X-ray photoelectron spectroscopy

The photoelectric effect was first explained by Einstein in 1905. [140] He stated that an impinging photon can excite an electron from the inner shells of an atom. The energy that is transferred ($h\nu$ with Planck's constant h and the frequency ν) has to be higher than the binding energy of the electron E_{bind} plus the energy needed to excite the electron to the vacuum level Φ. Additional energy is converted into kinetic energy E_{kin}:

$$h\nu = E_{\mathrm{bind}} + \Phi + E_{\mathrm{kin}} \tag{1.12}$$

In X-ray photoelectron spectroscopy (XPS), X-rays are used for the emission of electrons out of the sample material. The energy of the incident beam is high enough to excite electrons from the inner core shells of the atoms. By analyzing E_{kin} with a detector, their binding energy can be calculated. The result is a spectrum of the count rate *vs* the binding energy. Since the electrons from inner shells do not contribute to the chemical binding, their binding energy is characteristic for the chemical element. The peak position can be used to derive the composition and the intensities can be related to the content of the respective element in the sample. [141, 142]

1.4.8 Inductively coupled plasma atomic emission spectroscopy

Inductively coupled plasma atomic emission spectroscopy (ICP-AES) provides a means to perform elemental analysis. The sample is dissolved in a solvent or by the use of acids. Afterwards, it is injected in an argon

plasma at several thousand Kelvin. At this high temperature, the sample atoms become ionized and can recombine, emitting light of a wavelength characteristic for the element. Calibration measurements can be performed by using solutions of the pure element in varying concentrations. Then, the intensities of corresponding bands in the sample and calibration spectra can be compared. This allows to determine the concentration of the respective element in the sample. [143]

1.4.9 Photoluminescence spectroscopy

Emission of photons in a semiconductor can be caused by transitions from charge carriers from a high energy state to a low energy state or recombination of excitons. This process is initiated by external excitation. Depending on the source of this excitation, one can distinguish between e. g. chemiluminescence (chemical reaction), electroluminescence (electric current), cathodoluminescence (electron beam) or photoluminescence (optical). The latter is used in PL, where emission is stimulated by an optical light source. Then, the energy distribution of the emitted light is determined by spectral analysis. There are several possible mechanisms that contribute to the emission spectrum. Electrons in the conduction band, for example, can recombine with holes in the valence band (band-to-band transition). Free or bound carriers can recombine with bound carriers. Additionally, an electron and a hole can form a so-called exciton, i. e. they are bound together by Coulomb interactions and behave as a quasi-particle. These excitons can themselves contribute to the emissions. By measuring PL spectra, information about the band structure, band gap, impurities and defects can be gained. [144, 145]

For polycrystalline samples, it is also possible to correlate the crystallite

radius R with the measured band gap E^* [146]:

$$E^* = E_\mathrm{g} + \frac{h^2}{8R^2}\left(\frac{1}{m_\mathrm{e}} + \frac{1}{m_\mathrm{h}}\right) - \frac{1.8e^2}{\epsilon R} + \cdots \tag{1.13}$$

with the band gap of bulk ZnO E_g (3.37 eV), Planck's constant h, the effective electron and hole masses $m_\mathrm{e} = 0.24m_0$ and $m_\mathrm{h} = 0.45m_0$ and the dielectric constant of ZnO $\epsilon = 3.7$. [147]

For doped samples, it is also possible to investigate the dependence of the emitted light on the doping content. Here, it has to be taken into account that with increasing doping content, the crystallite size might change. Therefore, it is necessary to distinguish between the two influencing parameters. This can be done, for example, by inserting the crystallite sizes calculated from XRD data into equation 1.13 to get E^*. Only if this value is uncorrelated to the measured E^*, the shift of the UV band can be attributed to the doping.[145]

1.4.10 Conductivity measurements

A method to measure the conductivity of thin film samples with an irregular shape was developed by van der Pauw.[148] Four contacts, A, B, C and D are placed on the circumference of the sample. By measuring the potential between contacts C and D (U_CD) and the current between A and B (I_AB) the resistance can be calculated as

$$R_\mathrm{AB,CD} = \frac{U_\mathrm{CD}}{I_\mathrm{AB}}. \tag{1.14}$$

Correspondingly, a second resistance $\mathrm{R_{BC,DA}}$ can be defined. For a known film thickness d, the resistance is correlated to the specific resistance ρ of the material:

$$\exp\left(\frac{-\pi d}{\rho}R_\mathrm{AB,CD}\right) + \exp\left(\frac{-\pi d}{\rho}R_\mathrm{BC,DA}\right) = 1. \tag{1.15}$$

Additionally, the sheet resistance ρ_s can be calculated by dividing ρ by d.

The samples for the van der Pauw method have to fulfill certain requirements:

- The contacts are infinitely small.
- The film thickness is homogeneous over the complete sample surface.
- There are no isolated holes in the film.

2 Experimental Part

2.1 Template preparation

2.1.1 Cleaning of Si wafers

For the deposition of different templates, boron-doped Si (100) wafers (Siltronic) were used. Organic and inorganic residuals, were removed by several cleaning steps in water and organic solvents. First, the wafers were immersed in Milli-Q water (18 MΩ cm) and treated in an ultrasonic bath for 10 min. After drying with a stream of nitrogen, another ultrasonification in a mixture of ethanol/acetone 1:1, again for 10 min, was applied. The next step was to use oxygen plasma (10 min, 30 W, *PlasmaCleaner Plasma Prep*^{2}, GaLa Gabler Labor Instrumente) to clean the surface further and to increase the number of surface silanol groups. [149, 150] Finally, the wafers were again cleaned in Milli-Q water for 10 min in ultrasound.

Cleaning of the substrates used for PS brush formation was performed at the Institute of Nanotechnology, Karlsruhe Institute of Technology (KIT). A CO_2 snowjet is a device for removing organic residues from a surface. A stream of CO_2 gas expands *via* a small nozzle. This leads to cooling of the gas so that liquid droplets and ice crystals are formed ("snow"). The impact of the droplets and crystals on a surface leads to mechanical abrasion of contaminations. Additionally, the liquid CO_2 dissolves organic residues on the surface.[151, 152] The substrates are held in place by a vacuum chunk. This chunk is heated to 30 °C to 40 °C. This prevents freezing of the

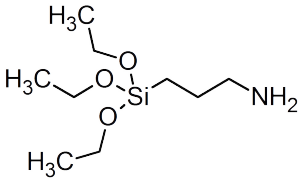

Figure 2.1: Chemical formula of (3-aminopropyl)triethoxysilane.

wafer. Cleaning is performed by directing the snowjet onto the substrate and moving it systematically along its surface for about 1 min.

2.1.2 Self-assembled monolayers

For the modification of the cleaned 1 cm × 1 cm or 1 cm × 2 cm Si wafers, SAMs with different functional groups were used. For amino functionalization, (3-aminopropyl)triethoxysilane (APTES) (figure 2.1) was applied, and a further modification step with succinic anhydride leads to carboxylate termination. The templates were used immediately after preparation. To get a highly hydrophobic surface, the wafers are modified with 1H,1H,2H,2H-perfluorodecyltrichlorosilane (FDTS).[153]

2.1.2.1 APTES

To get amino-functionalities, a solution of 0.05 ml APTES (Sigma-Aldrich, 99 %, figure 2.1) in a mixture of 0.5 ml water in 9.5 ml ethanol was prepared similar to [154] and left for hydrolyzation for 5 min. After that period, the wafers were immersed into the solution. Silanization then takes place for 1 h. Afterwards, the substrates are rinsed thoroughly in ethanol and dried with a nitrogen stream.

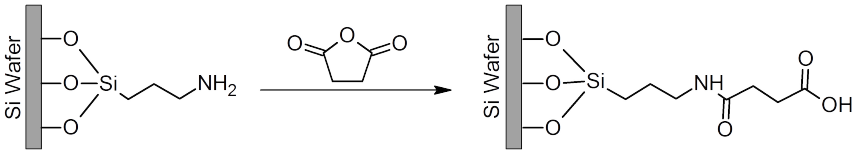

Figure 2.2: Modification process of the APTES SAM to achieve carboxylate functionality.

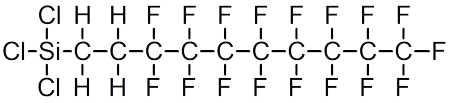

Figure 2.3: Chemical formula of the 1H,1H,2H,2H-perfluorodecyltrichlorosilane molecule.

2.1.2.2 Carboxylate-terminated SAMs

The APTES SAM can be modified with succinic anhydride (Sigma-Aldrich, $\geq 99\,\%$) for a carboxylate functionalization (figure 2.2). [17] The wafers are incubated in 10 ml of a 143 mM solution of succinic anhydride in N-methyl-2-pyrrolidone for 2 h. Then, the APTES-functionalized wafers are rinsed in water and dried with a nitrogen stream.

2.1.2.3 FDTS SAM

FDTS functionalization was performed in cooperation with Stefan Walheim (Institute of Nanotechnology, KIT). First, cleaned Si wafers were glued upside down into the lid of a desiccator. Secondly, two droplets of FDTS (Sigma-Aldrich, figure 2.3) were placed on the bottom. Then, a vacuum of 50 mbar was applied for 10 h to 12 h.

2.1.2.4 Structured Templates APTES/FDTS

Templates with APTES islands in a FDTS matrix were prepared by Stefan Walheim and Cheng Huang (both Institute of Nanotechnology, KIT) *via* polymer blend lithography (see chapter 1.3.1) according to Huang et al. [93]. A mixture of polystyrene (PS) ($M_w = 96\,\mathrm{kg\,mol^{-1}}$, polydispersity index = 1.04) and poly(methyl methacrylate) (PMMA, $M_w = 95.9\,\mathrm{kg\,mol^{-1}}$, polydispersity index = 1.05) with a mass ratio of 3:7 and a total concentration of $15\,\mathrm{mg\,l^{-1}}$ was dissolved in methyl ethyl ketone (Sigma-Aldrich). The solution was then spin-coated onto 1.5 cm × 1.5 cm Si substrates at 1500 revolutions per minute. The humidity should be kept at 40 % to 45 %. This is done by flooding the chamber with a mixture of pure nitrogen and nitrogen saturated with water at a flow rate of 40 standard cubic centimeters per minute.

For the deposition of the FDTS matrix, the PMMA is selectively dissolved by immersing the wafers with acetic acid for 30 s. The SAM is now deposited on the uncovered parts of the substrates as described in section 2.1.2.3.

Afterwards, the remaining PS islands are removed with a snowjet (see chapter 2.1.1). APTES is deposited onto these sites *via* the gas phase corresponding to the procedure described for FDTS (*cf.* section 2.1.2.3). In the end, the substrates are covered with islands of amino-terminated APTES areas in a fluorinated FDTS matrix.

2.1.3 Polystyrene brushes

PS brushes were obtained from Stefan Walheim and Cheng Huang (both Institute of Nanotechnology, KIT). Vinyl-terminated PS (Polymer Standard Source, $M_w = 2.6\,\mathrm{g\,mol^{-1}}$, $M_n = 2.4\,\mathrm{g\,mol^{-1}}$, see chapter 1.3.2) was dissolved in toluene to a concentration of 3 wt.%. 100 µl of this solution are then spin-coated onto a Si wafer cleaned with a snow jet and left to evaporate. To get a film of several micrometers in thickness, the process was

repeated 3 times. To graft the PS molecules to the natural SiO_x surface, the wafers are placed in a massive aluminum vacuum chamber. The chamber is evacuated to a pressure of less than 1 mbar and heated to 145 °C. After 12 h the samples are cleaned in a three-step counterflow rinsing process in tetrahydrofuran and dried with nitrogen. [155]

2.1.4 Polyelectrolyte layers

Template preparation for mineralization experiments and water contact angle (WCA) measurements, ζ-potential, AFM and SEM measurements were carried out by Fabian Streb within the scope of his master's thesis [156]. PE films were prepared with a layer-by-layer dip-coating technique. Poly-L-lysine hydrobromide (PLL, Sigma-Aldrich, $M_w = 15000 - 30000\,\mathrm{g\,mol^{-1}}$, figure 2.4a), poly-L-glutamic acid sodium salt (PGA, Sigma-Aldrich, $M_w = 15000 - 30000\,\mathrm{g\,mol^{-1}}$, figure 2.4b) and poly(sodium 4-styrenesulfonate) ($M_w = 70\,000\,\mathrm{g\,mol^{-1}}$, figure 2.4c) were dissolved separately in Milli-Q water to a concentration of $1\,\mathrm{mg\,ml^{-1}}$. The PLL solution was adjusted to a pH of 9 with 0.3 M KOH. For the subsequent dipping steps, a *Dipping Robot DR3* (Riegler & Kirstein) was programmed to get a final sequence of $(PLL–PGA)_2$–PLL–PSS. Each step takes 20 min. In between the coating steps, the wafers were dipped three times into Milli-Q water. Afterwards, the wafers were dried in a nitrogen stream.

2.2 Mineralization

2.2.1 Deposition from methanolic solution

Part of the deposition experiments and sample characterization were carried out by Caroline Hofmeister (samples on PS, [155, 157]) and Fabian Streb (samples on PE, [156]) within the scope of their diploma thesis and master's thesis, respectively.

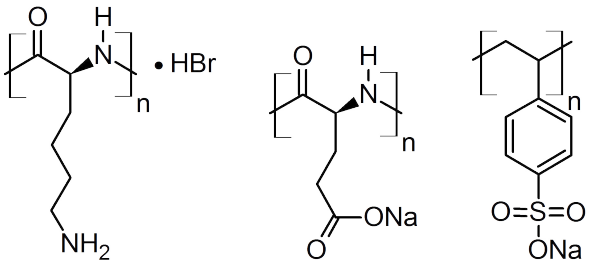

(a) (b) (c)

Figure 2.4: Structural formulas of the polyelectrolytes (a) poly-L-lysine hydrobromide, (b) poly-L-glutamic acid sodium salt and (c) poly(sodium 4-styrenesulfonate).

Care should be taken that all vessels used for preparation of solutions and during mineralization are dry. According to Stitz et al. [158], the water content influences the particle size and deposition mechanism. Therefore, vessels are kept at 80 °C in an oven until use.

For ZnO mineralization, stock solutions of $Zn(CH_3COO)_2 \cdot 2\,H_2O$ (Sigma-Aldrich, $\geq$ 99.0 %), TEAOH (Sigma-Aldrich, 1.5 M in MeOH) and PVP (Sigma-Aldrich, $M_w = 10\,000\,\mathrm{g\,mol^{-1}}$) in MeOH (J. T. Baker, VLSI) were prepared. Then, the zinc nitrate and PVP solutions are mixed and the TEAOH stock solution is added drop wise under gentle stirring. To maintain a constant speed of adding the solution, a peristaltic pump is used. The TEAOH solution is pumped through the tube at a constant velocity of $1.047\,\mathrm{ml\,min^{-1}}$. Due to the pumping intervals, drops form at the tube's outlet which are released into the zinc nitrate/PVP solution. This ensures a slow change in pH and prevents unwanted, macroscopic precipitation of zinc salts. Reaction solutions are freshly prepared every day to prevent agglomeration.

Two different batches of PVP (BCBF4168V and BCBJ4889V) were used. Their molecular weight distribution is slightly different. The M_w measured

Table 2.1: Concentrations and mixing volume ratios of deposition solution S1 with PVP batch BCBF4168V.

	concentration in stock solution [mM]	Mixing ratio	concentration in deposition solution [mM]
PVP	20	3	8.6
TEAOH	85	2	24.3
$ZnAc_2$	40	2	11.4

by gel permeation chromatography (performed at the Max Planck Institute for Polymer Research, Mainz) for batch BCBF4168V is $5607\,\mathrm{g\,mol^{-1}}$ whereas it is higher for batch BCBJ4889V ($M_w = 5783\,\mathrm{g\,mol^{-1}}$). Lipowsky et al. [68] found that the molecular weight has an influence on ZnO deposition. The higher the molecular weight, the slower the ZnO deposition gets. Therefore, the ratio [PVP]/[Zn^{2+}] has to be reduced for the solution with batch BCBJ4889V in comparison to the one with batch BCBF4168V to maintain optimum reaction conditions. In the following, reaction solutions prepared with batch BCBF4168V will be called S1 and solutions with batch BCBJ4889V are named S2. The composition of the solutions are shown in tables 2.1 and 2.2. Experiments that were carried out with S1 are deposition experiments on PS brushes (section 2.1.3) and doping experiments with aluminum (section 2.2.3). If not stated otherwise, all other experiments were carried out with S2.

To start a mineralization cycle, substrates are placed separately in screw-top jars and 1 ml of the reaction solution is added. The vessels are then placed in an oil bath heated to 60 °C and incubated for 90 min. Afterwards, the samples are washed in methanol thoroughly. For a new mineralization cycle, they are placed in fresh jars and fresh reaction solution is added. The number of cycles can be varied as is necessary to get thinner or thicker ZnO films.

Table 2.2: Concentrations and mixing ratios of deposition solution S2 with PVP batch BCBJ4889V.

	concentration in stock solution [mM]	Mixing ratio	concentration in deposition solution [mM]
PVP	25.71	1	8.57
TEAOH	75	1	25
$ZnAc_2$	37.42	1	12.47

It was found that PS brush samples are modified in the methanolic reaction solution (see 3.2). To investigate this process without film formation, the zinc acetate stock solution was replaced by pure methanol in the S1 recipe. Further reaction conditions and procedures were the same as described for a normal mineralization (see above). The samples were used after three modification cycles.

Additionally, the vinyl-terminaded PS powder was modified for three cycles. After each cycle, the powder was washed in methanol and centrifuged to separate the solvent. Afterwards, fresh reaction solution was added.

2.2.2 Deposition from aqueous solution

Experiments were partially carried out by Peter Gerstel.

Aside from the mineralization from methanolic solution, it is also possible to deposit ZnO from aqueous solutions [91]. In this case, 45 mM stock solutions in Milli-Q water contain $Zn(NO_3)_2 \cdot 6\,H_2O$ (Sigma-Aldrich, $\geq$ 99.0 %), histidine (His) (Sigma-Aldrich, $\geq$ 99 %) and hexamethylene tetramine (HMTA) (Sigma-Aldrich, $\geq$ 99.5 %), respectively. Equal amounts of the stock solutions are mixed by adding zinc nitrate solution drop wise to the other two under gentle stirring.

Si wafers covered with APTES/FDTS are put in screw-top jars and

Table 2.3: Concentrations of doping elements in zinc acetate stock solutions with respect to the concentration of Zn^{2+}.

Doping element	Doping concentrations [mol %]								
Al	0	2	4	5	10	15	20	30	50
Ga	0	1	2	3	4	5			
In	0	1	2	3					

covered with 2 ml of the deposition solution. It has to be taken care that the substrates are completely immersed into the solution since they are hydrophobic. Mineralization takes place at 70 °C for 4 h until the onset of turbidity of the solution.

2.2.3 Doping experiments

Deposition experiments and sample characterization for aluminum doping were performed by Rahel Eisele within the scope of her diploma thesis [159, 160].

Calculation of the stability diagrams of the doped solutions were performed with *ChemEQL v3.1* (eawag, Switzerland).

Salts of the doping elements were added to the zinc acetate stock solution in varying concentrations in relation to the concentration of Zn^{2+} (*cf.* Table 2.3): $Al(NO_3)_3 \cdot 9\,H_2O$ (Sigma-Aldrich, $\geq$ 98.0 %), $Ga(NO_3)_3 \cdot xH_2O$ (Sigma-Aldrich, 99 %) and $In(NO_3)_3 \cdot 9\,H_2O$ (Sigma-Aldrich, 99.9 %). Prepared stock solutions were stored in a fridge at 4 °C.

Reaction solutions were prepared as described in 2.2.1 on substrates functionalized with APTES. In the following, samples doped with Al, Ga and In are named aluminum-doped zinc oxide (AZO), gallium-doped zinc oxide (GZO) and indium-doped zinc oxide (IZO), respectively.

2.3 Sample characterization

2.3.1 Template characterization

2.3.1.1 Water contact angle measurements

Static WCA were measured with Milli-Q water on the freshly prepared templates with a *Contact Angle Measurement System G10* from Kruess. Results are an average of at least five measurements on several samples.

2.3.1.2 Zeta-potential measurements

ζ-potential measurements were carried out on a *SurPASS Electrokinetic Analyzer* from Anton Paar GmbH. Two samples with a size of 1 cm × 2 cm were prepared to fit in an adjustable gap cell. They were fixed on the stamps with double sided tape and the gap height was adjusted to 100 µm. Before and during the measurement, about 500 ml of a 1 mM KCl solution in Milli-Q water was purged with nitrogen. Additionally, it was gently stirred to ensure homogeneity. The system was rinsed with the solution before the measurement. Titration was performed automatically with a 0.1 M HCl solution. Prior to every measurement cycle, a rinse cycle is started with a pressure of 300 mbar that runs for 180 s. This allows the system to adjust to the new pH value. Afterwards, a pressure program is used for the measurement. In total, four pressure ramps are performed from 0 mbar and 40 mbar and the streaming current is recorded. ζ-potential values are calculated with a Fairbrother-Mastin approach to correct for surface conductance. [161]

2.3.1.3 Infrared spectroscopy

IR measurements were performed by Peter Lindemann (Institute of Functional Interfaces, KIT). [91]

For IRRA measurements, PS brushes were deposited onto Si wafers coated with 10 nm SiO_x, 100 nm Au and 5 nm Ti as adhesive layer between Au and Si (provided by Harald Leiste and Stefan Zils, both Institute for Applied Materials - Applied Materials Physics, KIT). This enhances the signal to noise ratio [162]. To obtain the spectra, a Bruker *Vertex 80* (Institute of Functional Interfaces, KIT) purged with dry air under a fixed angle of incidence of 80° was used. The detector was a narrow band liquid nitrogen cooled mercury cadmium telluride (LN-NB-MCT) detector with a resolution of $2\,cm^{-1}$. 1024 scans on a reference sample of perdeuterated hexadecanethiol-SAMs on Au/Ti/Si wafer were recorded. Afterwards, PS brush samples were measured before and after modification. A number of 900 to 3000 scans were cumulated and recorded until water bands vanished in the spectra.

To enhance the signal-to-noise-ratio, additional ATR measurements were performed on the vinyl-terminated PS powder used for the preparation of the brushes (*cf.* section 2.1.3). Since the sample volume is drastically increased, also the band intensities are increased. Spectra were recorded on a Bruker *Tensor 27* (Institute of Functional Interfaces, KIT) with *Platinum ATR* accessory and a room temperature deuterated L-alanine doped triglycine sulfate (RT-DLaTGS) detector with a resolution of $4\,cm^{-1}$. To determine the background signal, the empty diamond crystal was measured against air. For both background and sample, 64 scans were accumulated.

2.3.2 Characterization of ZnO thin films

2.3.2.1 Atomic force and piezoresponse force microscopy measurements

AFM tapping mode images of the PS brush and the AZO samples were taken by Caroline Hofmeister [155] and Rahel Eisele [160] on a Bruker *Multimode III* with commercially available tips from Nanosensors (*PPP-NCHR*).

Characterization of the APTES/FDTS covered wafers were done by Markus Moosmann and Jonathan Berson (both Institute of Nanotechnology, KIT) [91]. A Bruker *Dimension Icon* (Institute of Nanotechnology, KIT) was used in tapping mode under water. This prevents the effect of meniscus forces of surface absorbed water films that might be present. Imaging of the ZnO containing films on these substrates was performed with the same equipment, but tapping mode in air was used.

The topography of all other samples were was examined with a Bruker *Multimode VIII* with a *Nanosocope 5* controller. Tapping in air was performed with *PPP-NCHR* tips (Nanosensors). PE samples were characterized by Fabian Streb [156].

Piezoelectric properties of some of the samples were measured with a PFM setup on the Bruker *Multimode VIII*. Samples were glued onto AFM holders with graphite tape. Electrical contact was ensured by applying silver paste on the edges of the sample and connecting it with the bottom of the holder (figure 2.5). In contact mode, an AC voltage of 0 V to 10 V with a frequency of 20 kHz was applied between the tip (*MESP-RC*, Bruker) and the sample. The response of the sample (Amplitude 1) as well as the 2nd harmonic signal (Amplitude 2) were recorded simultaneously over a scan area of 1 µm × 2 µm. An average over the complete image gives the piezoelectric response and a mean value is determined by averaging at least four images per sample. The system has to be calibrated *via* the deflection sensitivity, that is calculated from the slope of a force-distance-curve. To obtain d_{eff}, the amplitude is plotted against the applied AC voltage. The slope of the Amplitude 1 curve gives d_{eff} and d_{33} can be calculated with equation 1.6.

2.3.2.2 Scanning electron microscopy

SEM images were taken by Felicitas Predel (Stuttgart Center for Electron Microscopy, Max-Planck-Institute (MPI) for Solid State Research, Stuttgart)

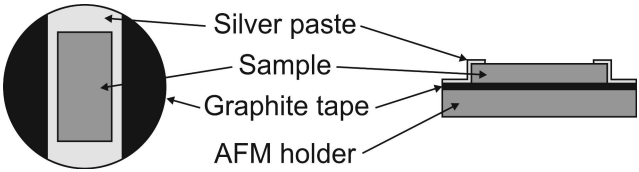

Figure 2.5: Schematic drawing of the samples prepared for PFM measurements. The samples are glued on an AFM holder and contacted with silver paste.

on a Zeiss *DSM 982 Gemini* (Stuttgart Center for Electron Microscopy, MPI for Solid State Research) with an accelerating voltage of 3 kV. Samples were sputtered with a 0.2 nm to 0.8 nm thin film of Pr:Pd (80:20). Stefan Kilper (Institute for Materials Science, University of Stuttgart) performed measurements on a Zeiss *Merlin* microscope (Nanostructuring Lab, MPI for Solid State Research). Samples for these measurements were sputtered with 0.2 nm Iridium on a Leica *EM ACE 600* (Nanostructuring Lab, MPI for Solid State Research). Cross sections were prepared freshly prior to the measurements by using a side cutter.

2.3.2.3 X-ray diffraction

XRD measurements were carried out by Maritta Dudek and Scherrer analysis was performed by Andreas Leineweber (both Department Mittemeijer, MPI for Intelligent Systems, Stuttgart).

Grazing incidence XRD measurements with an incidence angle of 2° on the PS brush and the AZO samples were done on a *X'Pert MRD* (PANalytical) with Cu K_α radiation. The beam is parallelized with polycapillary optics and a flat graphite monochromator is used in the diffracted beam. Measurements were performed in a 2θ range from 25° to 60°.

Other samples were measured on the same equipment in θ-2θ geometry. The diffractograms were recorded in a range of 28° to 40° with a step size of

0.04°. The samples were tilted by an angle of $\psi = 2°$ to prevent reflections from the substrate.

Texture coefficients $T_C(002)$ were calculated according to equation 1.10. [136] For $I_0(hkl)$, the standard relative intensity from the PDF card no. 1011258 for wurtzite ZnO powder was used. The $I(hkl)$ of the 100, 002, and 101 reflections of the corresponding samples were included, leading to $n = 3$.

The standard to determine the instrumental profile for crystallite size evaluation was LaB_6 powder (Standard Reference Material SRM 660a, National Institute of Standard and Technology NIST, Gaithersburg, USA) deposited on a zero-background specimen holder. Crystallite sizes were evaluated from the diffraction data with the help of the *TOPAS* software [163], applying a full-pattern Pawley refinement. A refined Lorentzian-shaped size broadening was matched for the line broadening of the ZnO diffraction pattern. The volume weighted mean column height D was calculated using equation 1.11. [138, 139]

2.3.2.4 X-ray photoelectron spectroscopy

The XPS measurements were carried out by Michaela Wieland (Department Mittemeijer, MPI for Intelligent Systems, Stuttgart) on a *Thermo VG Thetaprobe 300* (Department Mittemeijer, MPI for Intelligent Systems) with Al-K_α radiation ($h\nu = 1486.68\,eV$). To clean the sample surface, Ar^+ sputtering for 30 s on an area of 2 mm × 2 mm was applied. Afterwards, a survey scan between 0 eV and 1200 eV was recorded with a step size of 0.2 eV and a pass energy of 200 eV. For fitting, the individual regions of the Zn $2p_3/2$-, O 1s- and Al 2p-peaks were measured with a step size of 0.1 eV and a pass energy of 100 eV. The Zn $2p_3/2$-peak was normalized to a value of 1021.9 eV and the other peaks were shifted accordingly.

2.3.2.5 Inductively coupled plasma atomic emission spectroscopy

The samples were analyzed by Samir Hammoud and Gerhard Werner (both Central Scientific Facility Chemical Synthesis, MPI for Intelligent Systems, Stuttgart).

The films were dissolved in 1 ml HCl. Afterwards, the solutions were diluted up to 10 ml with Milli-Q water. Spectra were collected on a SPECTRO *Ciros CCD* (Central Scientific Facility Chemical Synthesis, MPI for Intelligent Systems, Stuttgart) with Ar plasma (6000 K to 7000 K). The emitted light was split and detected in a range of 125 nm to 800 nm. Quantitative evaluation was done with the help of reference solutions. For zinc and aluminum, Titrisol solutions (1000 ppm, Merck) were used. Reference solutions with different concentrations of gallium and indium were prepared by Samir Hammoud.

2.3.2.6 Photoluminescence spectroscopy

PL spectra were recorded on a Horiba Jobin Yvon *Fluorolog-3* with a Xe lamp. AZO samples were measured by Rahel Eisele [160] at an excitation wavelength of 325 nm with an step size of 1 nm and an integration time of 1 s. Other samples were measured at an excitation wavelength of 280 nm.

2.3.2.7 Conductivity measurements

Conductivity measurements were carried out by Jonathan Berson (Institute of Nanotechnology, KIT).

The samples with a square shape were contacted with microelectrodes of silver paste at the corners. Van der Pauw measurements were carried out on a probe station of Süss Microtec AG. An Agilent *4156C Analyzer* was used to sweep the current between two neighboring connections while the voltage was measured between the other two. The slope extracted from the measured I-V curve gave the resistance. A second measurement was

performed to get an average value R_A. By switching the current source and voltage measurement electrodes, the second resistance R_B was obtained. The sheet resistance can be calculated afterwards *via* equation 1.14.

3 Results and discussion

3.1 Template directed deposition of ZnO on SiO_x, SAMs and PE

In this work, the deposition of ZnO thin films on different organic templates is investigated. For a better understanding of the interactions between the polar crystallites (see chapter 1.1) in solution and the substrate surface, the as deposited templates are characterized. A cleaned Si wafer with a preoxidized SiO_x layer is used as a reference surface (see chapter 2.1.1). For the modification of this substrate, three different SAMs (APTES, COOH and FDTS) and polyelectrolyte multilayers with SO_3H-functionalization (*cf.* chapter 2.1.4) were investigated.

3.1.1 Template formation and characterization

In a first step, the templates used for the ZnO deposition were characterized by AFM and WCA measurements.

AFM images (figure 3.1) show very smooth surfaces for the SiO_x and the SAMs. The root mean squared (rms) roughness is (0.1 ± 0.0) nm for all surfaces, only the COOH-terminated SAM is slightly rougher with (0.7 ± 0.1) nm.

The template with the highest rms roughness of (6.8 ± 0.5) nm is the PE multilayer. As is described in the experimental section (section 2.1.4), this multilayer is formed by the layer-by-layer deposition of polymeric molecules.

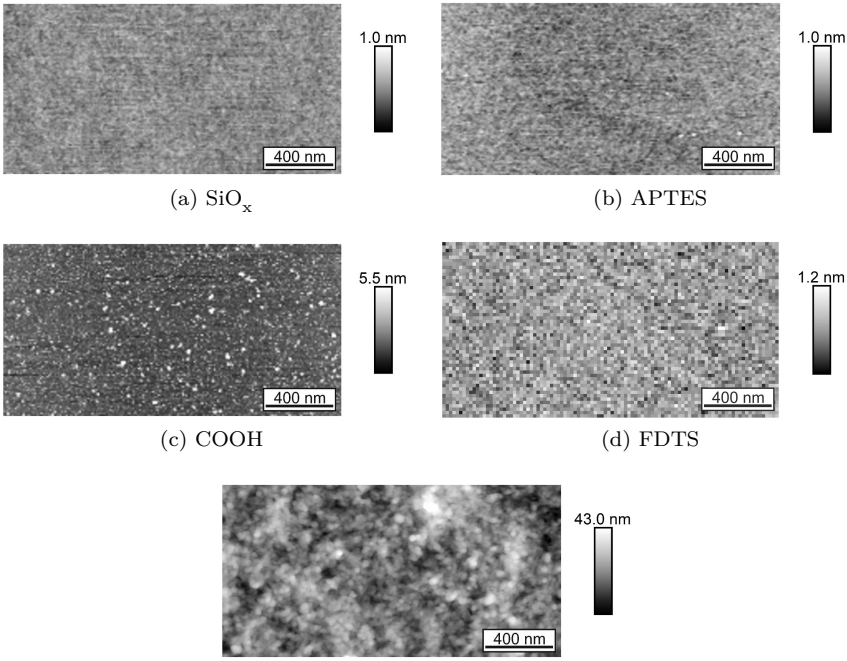

(a) SiO_x (b) APTES

(c) COOH (d) FDTS

(e) PE

Figure 3.1: AFM images of a SiO_x surface (a) and Si wafers covered with APTES (b), COOH-terminaded SAM (b), FDTS (d) and polyelectrolyte multilayer consisting of PLL, PGA and PSS (e).

The polyelectrolytes PLL and PGA form the multilayer with a terminal layer of PSS to provide a highly negatively charged surface. The higher roughness reveals that the structure of these layers is highly irregular. Additionally, Lipowsky et al. [18] measured a thickness of 15 nm for the PE multilayer with transmission electron microscopy. This is larger than that of the SAMs (1 nm to 2 nm).[1]

Information about the hydrophilic or hydrophobic character of the templates can be gained by measuring the WCA. The SiO_x layer of the substrate is the surface with the best wettability. Its WCA is as low as $(4 \pm 1)°$. This value corresponds to values reported by other groups for oxygen plasma treated Si wafers. [164–166] Hydrophilic behavior is also observed for APTES, the COOH-terminated SAM and the PE multilayer. The corresponding contact angles are $(48 \pm 5)°$, $(35 \pm 6)°$ and $(29 \pm 4)°$, respectively. The values are in the range of values found in literature. For APTES, WCAs between 38° and 70° were reported [154, 165, 167–169], while for COOH-terminated SAMs values between 27° and 58° were measured [74, 169–171]. The WCA of the PE layers is slightly lower than these values and indicates that this surface is more polar compared to the carboxyl-terminated one. A sulfonated SAM characterized by Shyue et al. showed a similar WCA of 32°. [74]

The only hydrophobic surface modification used in this work is the FDTS SAM. Therefore, the WCA of 104° is higher than for the other SAMs but in the range of 108° to 118° found by several groups for fluorinated SAMs and teflon. [154, 172–174]

[1] The thickness of the SAMs was measured with a single- wavelength ellipsometer (*DRE-ELX-02*, DRE, Germany) by Stefan Walheim at the Institute of Nanotechnology, KIT.

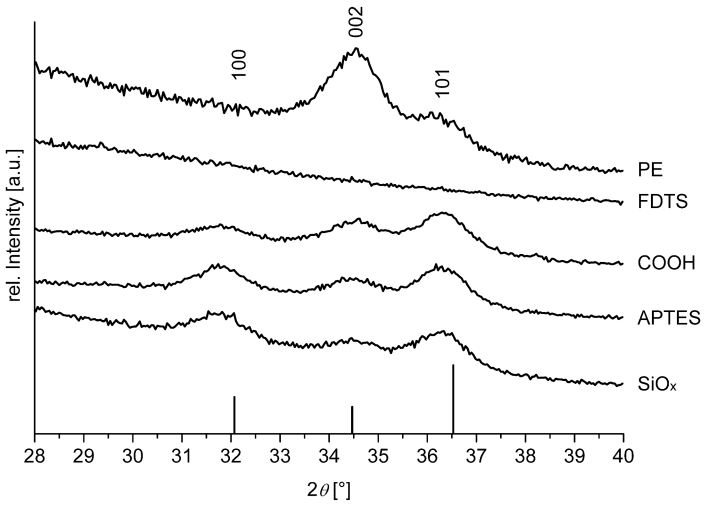

Figure 3.2: Diffractograms of ZnO samples after 20 mineralization cycles on different templates. Except for FDTS templating, all other organic modifications lead to the formation of wurtzite-type ZnO. The peak positions and relative intensities according to PDF card no. 1011258 are shown as lines at the bottom.

3.1.2 ZnO growth on SiO_x, SAMs and PE

The influence of the different templates on the ZnO deposition was studied on substrates that were mineralized for a varying number of deposition cycles (with 90 min each, see section 2.2). Phase analysis was performed by XRD. The deposition of ZnO on the SAMs and the PE multilayers could be confirmed with the exception of substrates modified with FDTS (figure 3.2).

The absence of any reflections in the diffractogram of the FDTS sample indicates that no or only a very small amount of ZnO was deposited. For the other templates, the characteristic reflections for wurtzite-type ZnO

can be identified (PDF card no. 1011258). The three main reflections at 32.1°, 34.5° and 36.5° 2θ correspond to the crystallographic planes of ZnO indexed 100, 002 and 101, respectively.

The nanocrystalline character of the ZnO films leads to significant broadening of the reflections. The mineralization solution contains PVP to control crystal growth. Its concentration was adjusted in a way that the particle sizes remains below 10 nm. [175]

The relative intensities of the ZnO film grown on the PE layers differ from the reference powder sample. The 002 reflection is more intensive compared to the 101 reflection, which is the most intensive for powders. The calculated texture coefficient $T_C(002)$ (compare chapter 1.4.6) of 2.15 confirms this statement. The texture coefficient for a random powder is close to 1. This indicates that in this film the attachment of the crystallites with their c-axis perpendicular to the substrate is favored.

The faces perpendicular to the c-axis of a ZnO crystallite are terminated by Zn^{2+} ions (0001) or O^{2-} ions $(000\overline{1})$. This leads to an intrinsic dipole moment of the crystallites (compare chapter 1.1). [7, 176] Furthermore, the templates exhibit a surface charge in the deposition solution that can interact with that dipole moment of the ZnO crystallites (figure 3.3). ζ-potential measurements on sulfonate-terminated SAMs show that sulfonate groups provide a high surface charge of -115 mV at a pH of 9, which corresponds to the pH of the deposition solution. [74] In contrast to this, a COOH-terminated SAM investigated in the same study shows a lower charge of -75 mV at a pH of 9. The ζ-potential of an amino-terminated SAM was even lower than that of the other two SAMs (-30 mV). [74] It has to be taken into account that the ζ-potential results were obtained in water. However, the solvent used in this work is methanol. Water has a dielectric constant of 80.4 whereas the dielectric constant of methanol (32.4) is much lower. [177] The polarizability of the solvent has a great influence on the surface charge of materials. This was shown for example by Kosmulsky et

al. [178]. They measured decreased values for the ζ-potential of silica in water/methanol mixtures compared to pure water.

The dipolar ZnO crystallites can interact with the surface charge of the templates (figure 3.3). The high negative charge density of the sulfonate-terminated PE attracts the positively charged face of the crystallites and leads to oriented attachment. The common orientation of the crystallites is the base for the 002 texture observed in the XRD diffractograms. Additionally, a strong interaction between sulfonate groups and zinc ions was found by Wegner et al. which supports this process. [179]

In comparison, the negative charge densities of the COOH-terminated SAM and the amino-terminated APTES are lower. Thus, the electrostatic interaction with the ZnO crystallites is decreased. The attraction is not strong enough to support oriented attachment. The crystallites attach to the surface randomly and non-oriented films grow (exemplarily shown for the COOH-terminated SAM in figure 3.3). The reflections in the corresponding XRD diffractograms show relative intensities close to those of a powder sample (figure 3.2).

To gain information about the film growth and structure, AFM (figure 3.4) and SEM (figure 3.5) measurements were performed for several stages of the mineralization process.

The AFM images of the ZnO deposited for three deposition cycles reveal differences in the early film growth. On SiO_x and FDTS, only small, isolated particles are visible (figures 3.4a and 3.4d). On APTES, there are particles as well, but the amount of ZnO that was deposited is higher compared to that on SiO_x or FDTS (figure 3.4b). The beginning of film growth can be observed on the COOH-terminated SAM and on the PE multilayer templates (figures 3.4c and 3.4e). While there are still holes in the film on the first template, an already dense layer is visible on the latter template.

These results also reflect in the SEM measurements performed after 5 and 20 deposition cycles (figure 3.5). The FDTS template inhibits the film

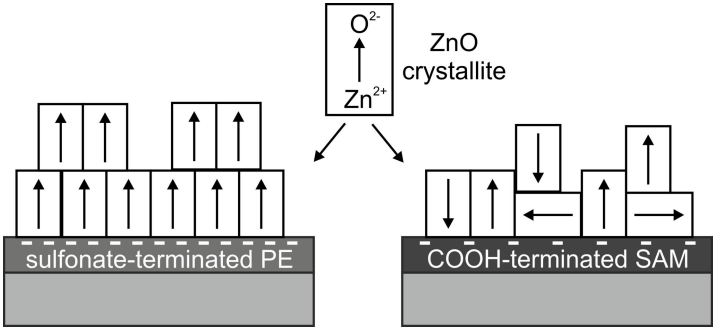

Figure 3.3: The ZnO crystallites have polar faces terminated by Zn^{2+} or O^{2-} ions, respectively, which lead to an intrinsic dipole moment. The charged templates can interact with this dipole moment. The high charge density of the sulfonate-terminated PE allows oriented attachment of the crystallites. The negative charge of the COOH-terminated SAM is not high enough to support oriented attachment and a film with random crystallite orientation is formed.

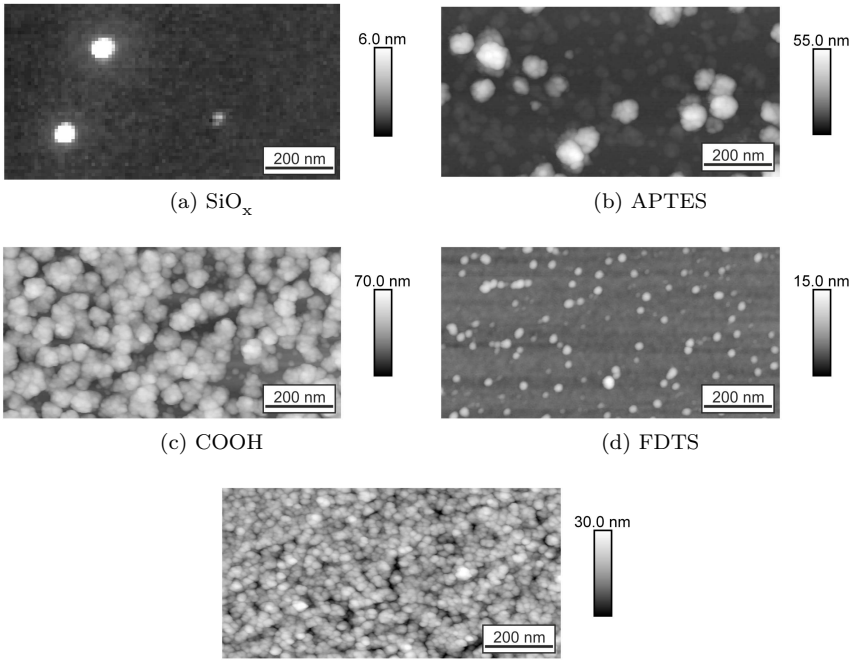

(a) SiO_x (b) APTES

(c) COOH (d) FDTS

(e) PE

Figure 3.4: AFM images after 3 deposition cycles of ZnO on SiO_x (a), APTES (b), COOH (c), FDTS (d) and PE (e).

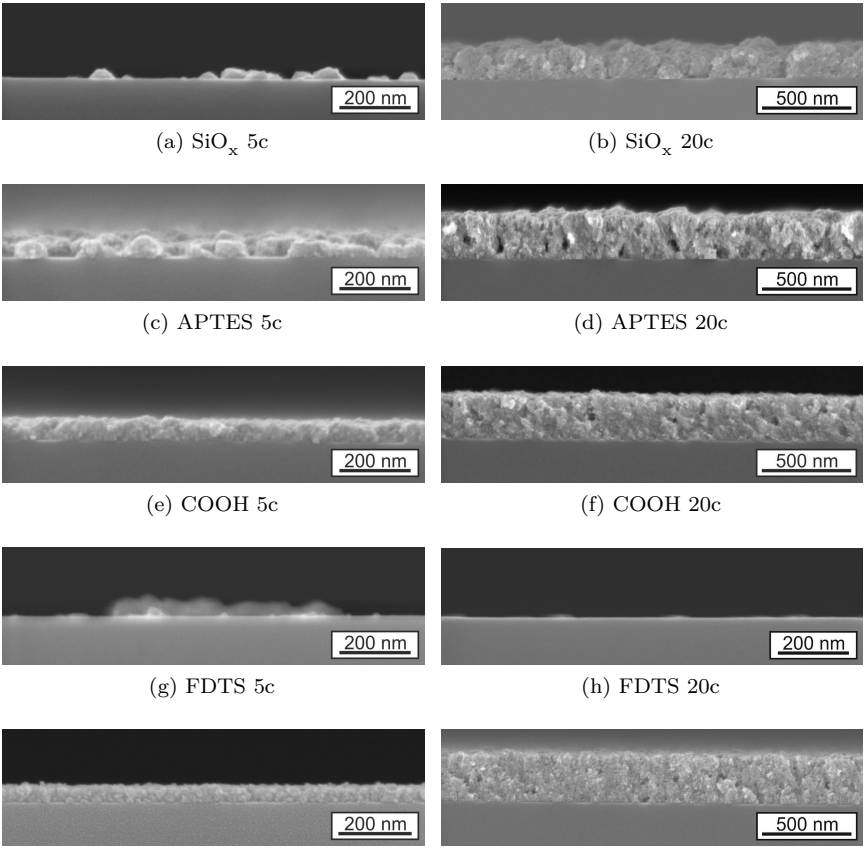

(a) SiO_x 5c (b) SiO_x 20c

(c) APTES 5c (d) APTES 20c

(e) COOH 5c (f) COOH 20c

(g) FDTS 5c (h) FDTS 20c

(i) PE 5c (j) PE 20c

Figure 3.5: SEM cross sections after 5 (a, c, e, g, and i) and 20 cycles (b, d,f, h, and j) of ZnO on SiO_x (a,b), APTES (c,d), COOH (e,f), FDTS (g,h) and PE (i,j).

growth even after 20 mineralization cycles (figures 3.5g and 3.5h). Here, the interaction between the polar ZnO particles in solution and the non-polar surface of the SAM is disadvantageous [81, 83]. It is also not possible for agglomerates to precipitate onto the substrate since the reaction solution is exchanged to prevent agglomeration (see chapter 2.2.1). The result is a clean FDTS surface. The presence of the few particles shown in figure 3.5g might be explained by defects in the FDTS layer. These molecule-sized holes can act as preferred growth sites that allow ZnO formation. [81, 83] These results confirm the XRD measurements. The amount of ZnO that is deposited is below the detection limit of this technique.

In contrast to FDTS, film growth on SiO_x is delayed but not suppressed completely. A closed film is not seen before 20 cycles (see figure 3.5b). The image for 5c (figure 3.5a) shows that the small particles observed in the AFM images (figure 3.4a) develop into islands that slowly merge and form a closed film. This is unexpected, since the SiO_x surface should be charged negatively under the reaction conditions, even though the deposition takes place in methanol. [74, 178, 180, 181] The dipolar ZnO particles are expected to interact with the polar surface, which should support homogeneous film growth. Therefore, the island growth has to have other reasons. Kim et al. [182] assumed for ZnO deposited by chemical vapor deposition onto silica, that the Volmer-Weber like growth is caused by the interfacial and surface energies of the system. During growth, the substrate surface, here SiO_x, is replaced by the surface of the growing ZnO islands and the interface between the ZnO and the SiO_x substrate. Volmer-Weber growth occurs, when the interface energy between SiO_x and ZnO ($\gamma_{SiO_x/ZnO}$) plus the surface energy of ZnO (γ_{ZnO}) is higher than the surface energy of SiO_x (γ_{SiO_x}): [183]

$$\gamma_{SiO_x/ZnO} + \gamma_{ZnO} > \gamma_{SiO_x}. \tag{3.1}$$

As a result, island growth is favored over film formation, which was observed

on the samples shown in figures 3.4a and 3.5a.

On the other templates (APTES, COOH-terminated SAM and PE multilayers), closed films are formed more readily than on SiO_x or FDTS. As observed by AFM, the ZnO on APTES is still very inhomogeneous at 5c (figure 3.5c). After 20c, a closed film has grown, but the roughness is still high and there are some big pores visible (figure 3.5c). In comparison, the films on COOH-terminated SAM and PE are more dense (figures 3.5e and 3.5i). Still, the films grown on the sulfonate-terminated PE are more homogeneous than those on the COOH-terminated SAM.

The growth rate on the different templates was monitored by measuring the film thickness after different numbers of deposition cycles (figure 3.6). Deposition on the FDTS samples is inhibited. Therefore, it was not possible to measure a film thickness and the values are missing in the diagram. On SiO_x, island growth was observed up to deposition cycle 10. After that, the islands merge into each other and a continuous film develops. This delay is responsible for the low height values. The inhomogeneous height of the islands is transferred to the growing films and lead to high standard deviations.

The film thickness on APTES, the COOH-terminated SAM and the PE multilayers increases with increasing number of deposition cycles. However, the growth rate is independent on the type of template used. Assuming a constant increase in film thickness, the calculated growth rate (11 nm/depositioncycle) is identical for all three templates.

These results show that the templates influence the growth of ZnO films strongly. The non-polar FDTS inhibits the deposition of the dipolar ZnO crystallites completely. The high negative surface potential of the SiOx substrate [74, 178, 180, 181] cannot compensate surface energy effects that lead to island growth. For APTES, the COOH-terminated SAM and the PE multilayers, the polarity of the templates has a strong influence on the early stages of ZnO film growth. The low ζ-potential of APTES (-30 mV

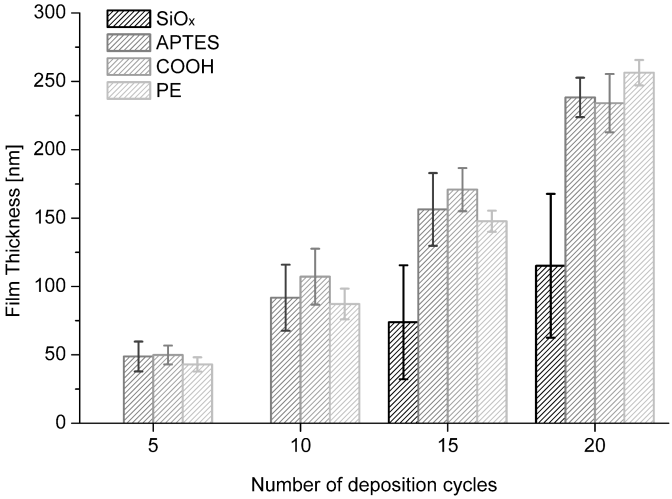

Figure 3.6: Film thickness in dependence on the number of deposition cycles measured from SEM cross-sections. Results for the FDTS samples are missing since no deposition was observed on this template. Continuous films on SiO_x could be found only after 15 deposition cycles.

[74]) leads to weak interaction with the dipolar ZnO particles (compare figure 3.3). The growing films are highly inhomogeneous (figures 3.4b, 3.5c and 3.5d) and the crystallites attach with random orientations (figure 3.2). The higher surface charge of the COOH-terminated SAM (−75 mV [74]) can support more homogeneous film growth, but still, the relative intensities in the XRD diffractograms are close to that of a powder with random crystallite orientation (figure 3.2). The films that are most homogeneous in this study are observed on the PE multilayers. The high negative surface charge of −115 mV [74] leads to strong interaction with the dipolar ZnO particles in solution. The particles attach to the template in an oriented way and a 002 texture is observed (figure 3.2). With increasing film thickness, the influence of the templates on the ZnO growth vanishes. After a closed film is formed, the ZnO particles from solution attach to the already grown ZnO film. Consequently, the growth rates assimilate and are identical, independent of the underlying template.

3.2 Deposition of textured ZnO films on vinyl-terminated PS brushes

3.2.1 Template characterization and transesterification

For the modification of a Si wafer with a PS brush, the molecule depicted in figure 3.7a was used. The mechanism of brush formation is still under discussion. Maas et al. [101] propose a mechanism where water is released by condensation reactions of siloxane groups at the substrate surface. These water molecules cause a transformation of the vinyl-terminated end of the PS molecule into alcohols. Afterwards, the newly formed alcohol groups react with the surface silanol groups. The result is a dense PS brush (figure 3.7b).

The substrate surface after the brush formation is shown in the AFM

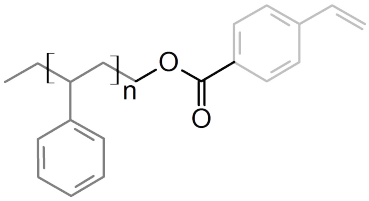

(a)

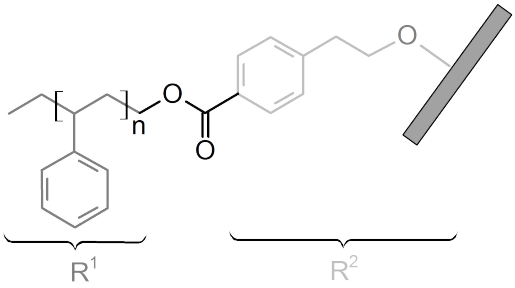

(b)

Figure 3.7: (a) α-methyl-ω-p-vinyl-benzoate-polystyrene used for the brush formation. (b) The vinyl endgroup transforms into an alcohol and attaches to the substrate surface *via* a condensation reaction with a silanol group.

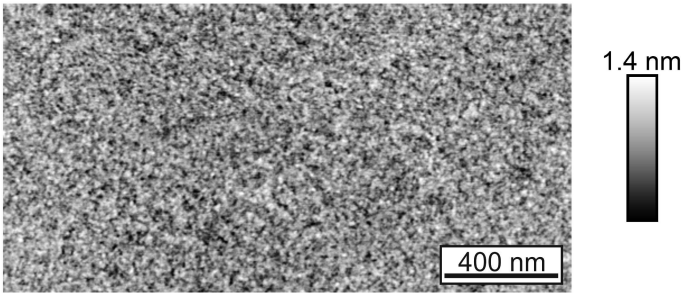

Figure 3.8: AFM image of a PS brush.

image (figure 3.8). The rms roughness is around (0.4 ± 0.2) nm and similar to the roughness of the SAM templates (see section 3.1.1).

The thickness of the template made of brushes can be measured by scratching the polymer layer and measuring the height difference between substrate and layer with an AFM. The height of the PS brush in this work is around 1 nm to 2 nm. As can be seen from figure 3.8, the substrate is homogeneously covered. Assuming a complete coverage, a brush density of 20 % to 40 % (0.24 molecules/nm^2 to 0.48 molecules/nm^2) can be calculated.[2]

Due to the low polarity of PS, hydrophobic behavior is expected after

[2]The molecular weight of the PS is $M_w = 2600\,\mathrm{g\,mol^{-1}}$. Since a single monomer has a molecular weight of $104.15\,\mathrm{g\,mol^{-1}}$, the polymer consists of 25 monomers. Estimating a length of 0.2 nm/monomer, this gives a total length of 5 nm, for a fully stretched molecule.

The volume of one mole PS ($4.32 \times 10^{-21}\,\mathrm{cm^3\,mol^{-1}}$) can be calculated by dividing the molecular weight ($M_w = 2600\,\mathrm{g\,mol^{-1}}$) by the specific weight ($1.05\,\mathrm{g\,cm^{-3}}$). With the Avogadro constant, this gives a volume per molecule of 4.11 nm^3/molecule. The volume V of one molecule is given by $V = Ah$. Taking the height h of 5 nm for a fully stretched molecule, the area A per molecule is 0.82 nm^2/molecule, which gives a grafting density of 1.22 molecules/nm^2.

The measured height of the brush is only 1 nm to 2 nm and not 5 nm as for a fully stretched brush with linear conformation. Therefore, the molecules are coiled up and need more space per molecule. Consequently, the grafting density is lower. With the volume per molecule of 4.11 nm^3/molecule this gives an area of 4.11 nm^2/molecule to 2.06 nm^2/molecule. Therefore, a nominal grafting density of 0.24 molecules/nm^2 to 0.48 molecules/nm^2 can be estimated.

coating of the substrate. This is confirmed by a WCA of 80°. ζ-potential measurements show that the brush shows a surface charge of $-47\,\mathrm{mV}$ at a pH of 9 which is caused by the adsorption of ions to the surface. [112]

Such a hydrophobic surface should not be suitable for ZnO mineralization (compare the results for the FDTS SAM in chapter 3.1.2). However, as will be seen in chapter 3.2.2, homogeneous ZnO films can be deposited onto the brushes. Therefore, experiments were carried out to investigate the stability of the PS brush in the methanolic deposition solution.

The results from the WCA and ζ-potential measurements show that the brush behaves differently before and after the treatment. The WCA is lowered from 80° to 60°. Additionally, the IEP of the as prepared brush is at a pH of 6.5 whereas the modification leads to an IEP of pH 2.5 (figure 3.9). The ζ-potential decreases from $-47\,\mathrm{mV}$ to $-80\,\mathrm{mV}$ (both at $\mathrm{pH} = 9$).

Therefore, it can be assumed that the treatment in an alkaline methanolic solution causes a transformation of the brush to a more polar, negatively charged surface. A possible explanation for this behavior is a base catalyzed transesterification of the α-methyl-ω-p-vinyl-benzoate-polystyrene (see figure 3.7a). Figure 3.10 shows the reaction of a methanolate ion with the ester group.

The polymer chain (R^1 in figures 3.7 and 3.10) is detached from the surface and only a small molecule (R^2 in figures 3.7 and 3.10) with a methylester termination remains on the substrate. The polar ester group that was previously shielded by the non-polar polymer chain is now at the surface and dominates the behavior of the substrate.

Prehn et al. [98] studied another surface functionalized with a methylester. They found a WCA of 53° which is similar to the one measured on the modified brush of 60°. The difference between those two values suggest an incomplete decomposition of the PS brush, according to figure 3.10.

For further investigation of the decomposition process, IRRA measurements were performed on the brushes before and after modification. Figure

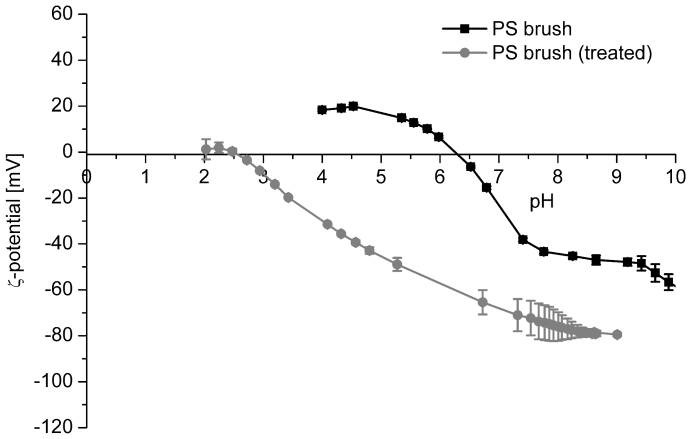

Figure 3.9: ζ-potential against pH for the PS brush templates before (black squares) and after (grey spheres) the treatment in the modification solution.

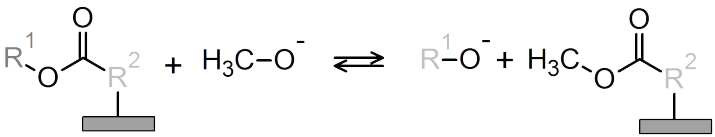

Figure 3.10: The scheme shows the transesterification reaction of a methanolate ion with a PS brush molecule. The ion attacks the ester bond and the polymer is split into two parts. The longer polymer chain R^1 is detached from the small end group R^2. The surface is now functionalized with a polar methylester group.

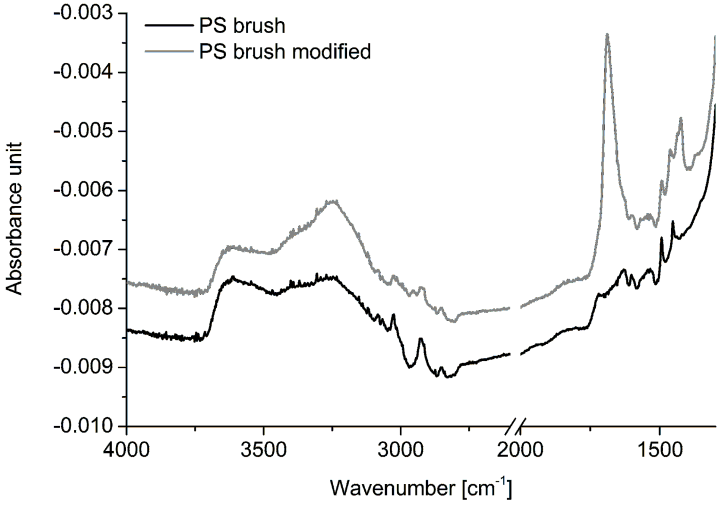

Figure 3.11: IRRA spectra of the PS brushes before and after treatment in the modification solution. The bands at $3025\,\mathrm{cm}^{-1}$ and $2928\,\mathrm{cm}^{-1}$ can be assigned to the polymeric background. Their intensity decreases after the treatment, confirming the modification due to the transesterification.

3.11 shows the obtained spectra.

The large band at $1688\,\mathrm{cm}^{-1}$ can be assigned to amide I [184]. The only component containing an amide group is PVP in the modification solution. Therefore, the band indicates that there is residual PVP present on the wafer. The band at $3025\,\mathrm{cm}^{-1}$ wavenumbers can be identified as the aromatic H-stretching mode. The bands at $2928\,\mathrm{cm}^{-1}$ and $2850\,\mathrm{cm}^{-1}$ correspond to the asymmetric and symmetric strechting modes of the backbone $\nu(\mathrm{CH_2})$, respectively. [185]

By comparing the two different spectra, it can be seen that the relative intensities of the bands assigned with $\nu(\mathrm{CH_2})$ of the backbone change

Table 3.1: Bands that can be correlated to the PS polymer. [185]

Wavenumber cm^{-1}	Assignment
3028-3026	Aromatic H-stretching modes
2922-2849	$\nu(CH_2)$
1600-1311	Aromatic vibrations
1070-1028	Aromatic H-bending modes
908	Aromatic vibrations
754	Aromatic vibrations

after the treatment. Therefore, the decreased intensities indicate that some of the chains named R^1 are detached from the surface. The residual intensities after the treatment confirm the conclusion drawn after the WCA measurements, i. e. the transesterification is incomplete and there are modified and unmodified molecules present.

To double-check these results, ATR experiments were carried out on the α-methyl-ω-p-vinyl-benzoate-polystyrene powder used for the brush formation. The advantage of using the powder is the higher amount of material available for the measurements. Since the polymer is insoluble in the modification solution, it is possible to treat, wash and dry it. During the transesterification, the polymer is split into two parts (see figure 3.10). This time, the molecule is not attached to a substrate. Therefore, the insoluble polymer part (R^1) remains in the reaction vessel, whereas the small endgroup (R^2) is soluble and is removed during the washing process.

The spectra obtained before and after modification (figure 3.12) show high similarity.

The bands that can be assigned to vibrations of the polymeric backbone are listed in table 3.1.

Changes in the relative intensities can be observed only in the bands correlated with the ester group (compare table 3.2). The corresponding bands are designated by arrows in figure 3.12.

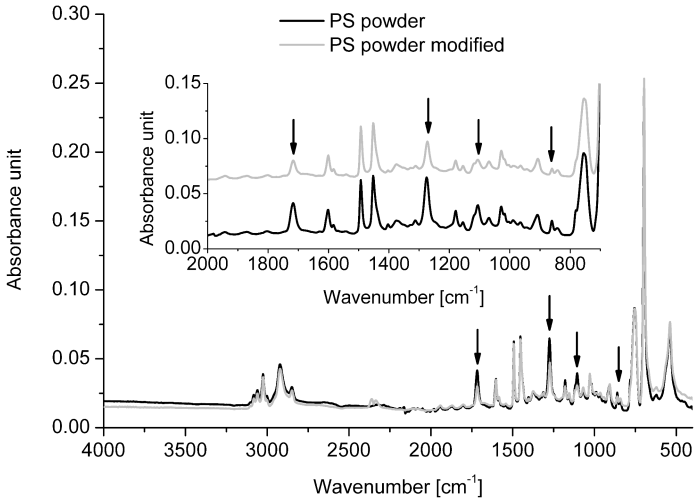

Figure 3.12: ATR spectra of the α-methyl-ω-p-vinyl-benzoate-polystyrene powder before and after treatment in the modification solution. The arrows mark the bands associated with the ester group that show a change in intensity after the treatment.

Table 3.2: Bands that can be assigned to the ester group. [184]

Wavenumber cm^{-1}	Assignment
1716	ν(CO)
1274	ν_{as}(COC)
1107	ν_{s}(COC)
860	ν(COC)

Compared to the measurement before the treatment, the relative intensities of the ν(COC) vibrations decrease after the modification. This confirms the assumption that the small end group with the methylester (R^2) is soluble and removed in the washing step. As was already stated before, the transesterification process is not complete, since the bands coming from the ν(COC) vibrations are not vanishing completely.

In summary, it can be concluded that the polymeric template is modified in the deposition solution. Due to the transesterification reaction, the ester group that was previously shielded by the PS chain is afterwards exposed to the surface. The thus activated polar surface is expected to be a beneficial template for the deposition of ZnO thin films.

3.2.2 Deposition of ZnO films on PS brushes

Deposition onto the PS brushes was performed with the S1 deposition solution (see experimental part 2.2). XRD measurements confirm the formation of crystalline ZnO. The 100, 002 and 101 reflections are clearly visible in figure 3.13 at the diffraction angles 32.1°, 34.5° and 36.5° 2θ.

In comparison with the relative intensities of the reference PDF card no. 1011258, a preferred crystallographic orientation along the 002 direction is visible. The corresponding texture coefficient $T_C(002)$ is 1.71, which confirms this statement.

The PS brush has a negative surface charge after the transesterification (compare figure 3.9). These charges can interact with the dipolar ZnO crystallites. The mechanism is the same as for the ZnO deposition onto sulfonate-terminated PE (compare figure 3.3). The negative charges of the template attract the positively charged (0001) face of the ZnO crystallites. The result is an oriented attachment of the ZnO crystallites. Additionally, the flexibility of the brush molecules can support the formation of a textured film. Turgeman et al. found that dense arrays of ZnO crystals form if the underlaying SAM molecules are free to rotate. By rotation of a phenyl ether

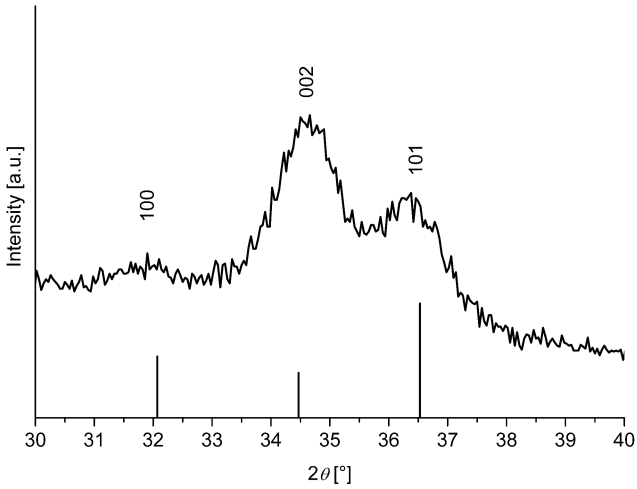

Figure 3.13: XRD result of the ZnO film deposited onto PS brushes after 20 deposition cycles. The line diagram at the bottom shows the reflections and relative intensities of the reference PDF card no. 1011258 of ZnO.

group, the polar ether can interact with the ZnO crystallites in solution. This allows oriented attachment of the crystallites. [186, 187] The reduced grafting density of the PS brushes (see chapter 3.2.1) provides a base for molecular rotation as well. After modification, the small remaining molecule is terminated by a methyl ester group. Rotation of this group supports the formation of textured ZnO films.

The film growth was investigated with AFM and SEM measurements after different numbers of deposition cycles (figure 3.14). A closed film is observed after 3 deposition cycles by AFM. SEM cross sections show that the films are dense with moderate porosity and homogeneous in thickness. The thickness increases with increasing number of deposition cycles (figure 3.14b).

3.3 Template directed growth of ZnO films with defined granularity

The deposition of ZnO onto two different templates can be investigated by using laterally structured templates. Like this, it is possible to investigate the influence of both templates at the same time under exactly the same reaction conditions. A structure that combines a polar and a non-polar template can be prepared with APTES and FDTS. First, a polymer blend of PS and PMMA is spin-coated onto a silicon wafer and phase separation leads to an island/matrix structure (compare section 2.1.2.4). By selectively dissolving the matrix polymer, the substrate is exposed and e.g. FDTS can be deposited. Afterwards, the other polymer is dissolved and the islands can be filled with APTES.

Figures 3.15b and 3.15c show an AFM image and a height profile of a substrate with islands filled with APTES in a matrix of FDTS. The APTES molecules are shorter than the FDTS molecules. This leads to a height

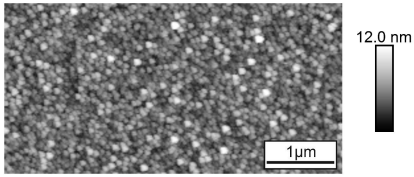

(a) PS 3c

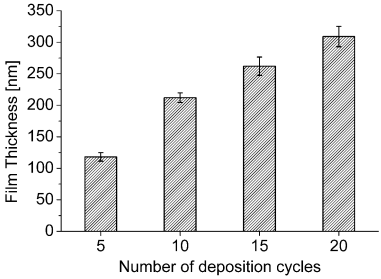

(b)

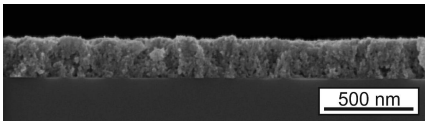

(c) PS 10c

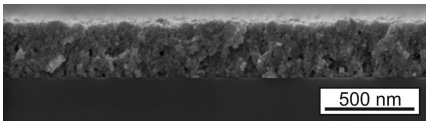

(d) PS 20c

Figure 3.14: Images of ZnO films grown on PS brushes. a) AFM image after 3 deposition cycles. b) Film thickness of the ZnO films on the brushes in dependence on the mineralization cycles. c) SEM image after 5 cycles and c) SEM image after 20 cycles.

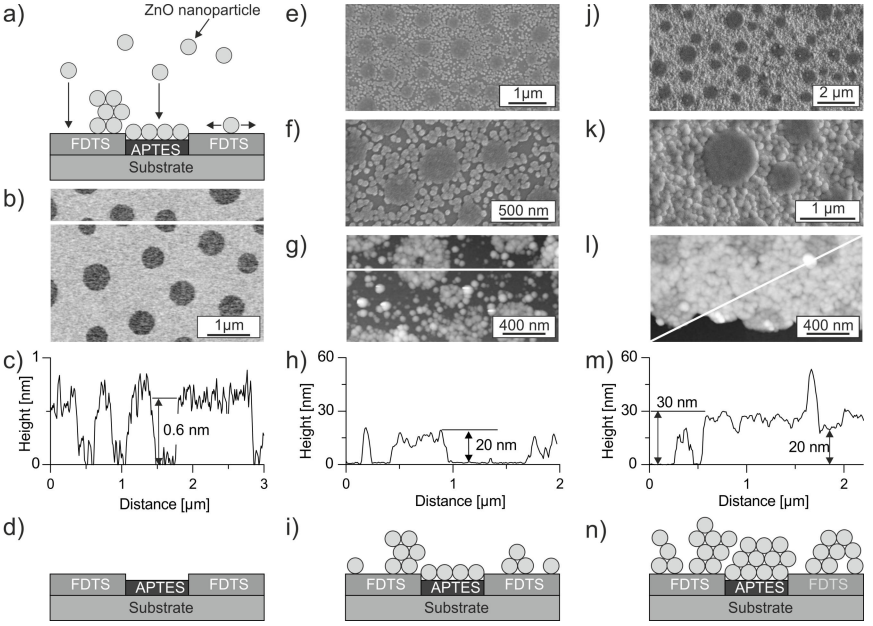

Figure 3.15: Deposition mechanism of ZnO nanoparticles onto a substrate with polar APTES and non-polar FDTS (a). (b-d) AFM image of the template before mineralization. (The white lines mark the positions of the height profiles shown in c), h) and m). The dark APTES islands are embedded in a matrix of FDTS. (e-i) SEM and AFM images of the substrates after the deposition. A compact film with a smooth surface is visible on the APTES islands while agglomerates are formed on FDTS. (j-n) The increasing amount of material leads to merging of the agglomerates into a coarse film, which represents the final morphology.

difference between the islands and the matrix of 0.6 nm. The rms roughness on the other hand is the same for both templates ((0.1 ± 0.0) nm).

The island/matrix structure of the templates leads to lateral structuring of the surface polarity. The islands are hydrophilic, whereas the matrix shows a non-polar, hydrophobic, behavior (compare chapter 3.1.1).

For ZnO deposition, an aqueous solution containing zinc nitrate and histidine was used. A temperature of 70 °C was found to provide optimum reaction conditions. Below this temperature, the particle growth is very slow. Above 70 °C, the deposition rate is very high so that bulk precipitation occurs and inhomogeneous films are formed. Gerstel et al. [65] found that the precipitated particles consist of a mixture of zinc hydroxide and zinc oxide. The material is X-ray amorphous (data not shown). The histidine controls the particle growth and is incorporated into the developing nanoparticles.

SEM and AFM images of the substrates after the deposition are shown in figures 3.15b, e-g and j-l. Schematic representations of the deposition mechanism are depicted in figures 3.15a, d, i and n. On the APTES islands, a homogeneous film with a rms roughness of 1 nm and a thickness of 20 nm is observed. The surface looks more granular in the AFM image (figure 3.15f) compared to the SEM image (figure 3.15g). This might be a result of the latter being less sensitive to topographic features compared to the AFM. In contrast to this, there are big agglomerates with diameters up to 75 nm visible on the FDTS matrix (figures 3.15k and 3.15l). The thickness of the resulting films is 30 nm with a rms roughness of 2.5 nm.

The deposition onto the two SAMs is governed by different driving forces. Gerstel et al. [65] measured a ζ-potential of 22.0 mV (pH = 6.7) on the ZnO particles. This means, at the pH of 5.3 of the deposition solution the particles are positively charged. At the same pH, the APTES is positively charged as well. For amino-terminated SAMs ζ-potentials of 30 mV [171, 181], 70 mV [74] or even 90 mV [188] were reported. Due to electrostatic repulsion,

Coulomb interactions cannot act as driving force for the deposition. This indicates that entropic interactions govern the mineralization of the APTES template. Both, template and particles are surrounded by a negatively charged Stern-layer. Upon approach of the surface, the ions from the particle's Stern layer can be replaced by the Stern-layer ions of the APTES. By releasing the residual counter ions, the entropy increases and functions as driving force (so-called counter-ion release force). [189] Additionally, van der Waals interactions contribute to the binding, as soon as close contact between the nanoparticles and the template is achieved. The homogeneous and dense distribution of the surface charges is directly reflected in the formed homogeneous film.

On the non-polar FDTS, electrostatic interactions are not active. However, particles can adsorb to the surface *via* van der Waals interactions. In addition, ions that are adsorbed to the template can be released in the same way as counter ions on the APTES leading to an entropic driving force for adsorption. Furthermore, the ZnO particles can interact with high-energy defect sites [81, 83]. Such defects can arise during the preparation of the template structure. Small defects with low density can form inside the FDTS matrix. Afterwards, when the islands are filled with APTES, the APTES molecules can also deposit into these defects. The result is a high surface energy spot inside the non-polar matrix to which the nanoparticles are attracted and fixed in their position.

The particles adsorbed by van der Waals or entropic forces are highly mobile. They can diffuse along the surface and coalesce with each other and the particles immobilized at the defect sites to reduce their surface energy (figure 3.15e-3.15i). The agglomerates grow and upon further deposition merge into a coarse but compact film (figures 3.15j-3.15n).

3.4 Piezoelectric ZnO thin films

The design of piezoelectric nanodevices requires a piezoactive material that can be structured to fit the devices geometry. ZnO has the highest piezoelectric coefficient in the group of wurtzite-type ceramics. [7, 190] Piezoelectric thin films were as yet only deposited *via* energy consumptive methods like radio frequency magnetron sputtering or sol-gel processes with subsequent annealing. [1–4] Therefore, it is of high interest to obtain piezoelectric thin films by bioinspired mineralization. Organic templates can be used to direct the formation of a texture which in turn directs the piezoelectric properties of the deposited films. In sections 3.1.2 and 3.2.2, it was shown that PE and PS templates on the one hand lead to the deposition of textured ZnO thin films. In the case of the COOH-terminated SAM on the other hand, XRD measurements confirmed a random orientation of the ZnO crystallites in the grown films. In this chapter, it will be described how the template-induced morphology influences the piezoelectric properties of the ZnO films. With piezoresponse force microscopy (PFM), a qualitative characterization of the localized piezoelectric response and a quantitative analysis of the average response of the samples were carried out.

3.4.1 PFM with local resolution

Figure 3.16 shows the PFM results of the ZnO films grown on COOH-terminated SAM, PS brushes and PE at 2 V, 6 V and 10 V. The color code corresponds to the magnitude of the piezoelectric response, i. e. the brighter the color, the higher the response.

The COOH sample for example shows a homogeneous dark grey color at all drive amplitudes. This can be explained by the lack of texture in the film ($T_C(002) = 1.35$). In the applied electric field, crystallites with different orientations respond differently. Therefore, the individual movements of the crystallites counteract and the net response is diminished. The amplitude

profiles at 10 V in figure 3.16d confirms this. The average response is as low as (9 ± 2) pm and even the maximum values do not exceed 20 pm.

The ZnO film on PS shows a homogeneous grey color as well. With increasing voltage, brighter domains can be distinguished from the background noise. As was already shown by XRD measurements (see chapter 3.2.2), the ZnO films deposited onto PS brushes exhibit a texture ($T_C(002) = 1.71$), i. e. many crystallites are oriented in the same direction. Clusters of such crystallites deform equally under an applied electric field. The deformation of these crystallites accumulates and a higher response can be measured, leading to visible domains in the amplitude images. Additionally, the macroscopic response of the sample is enhanced in comparison with the ZnO films on the COOH SAM. The cross section in figure 3.16h) shows that the average response is five times higher ((45 ± 6) pm at 10 V) with maximum values up to 75 pm. One reason for the low contrast in imaging PFM could be aging effects due to longer storage of the samples. Some surface layer might have formed that disturbs the tip-sample contact during the measurement. This could also explain the high noise level of that measurement.

In contrast to the other two samples, the film on the PE shows a distinct domain structure even at low drive amplitudes. The contrast between dark and bright domains increases with increasing drive amplitude. The average response at 10 V of (42 ± 4) pm is comparable to that of ZnO on PS. This can be correlated to the texture coefficient calculated from the XRD results ($T_C(002) = 2.15$), which is slightly higher compared to the one of ZnO on PS.

3.4.2 Evaluation of the piezoelectric constants

To quantify the magnitude of the response of the investigated samples, the average response at different spots on the sample and for several drive amplitudes was calculated. Figure 3.17 shows Δz_ω and $\Delta z_{2\omega}$ plotted against the drive amplitude.

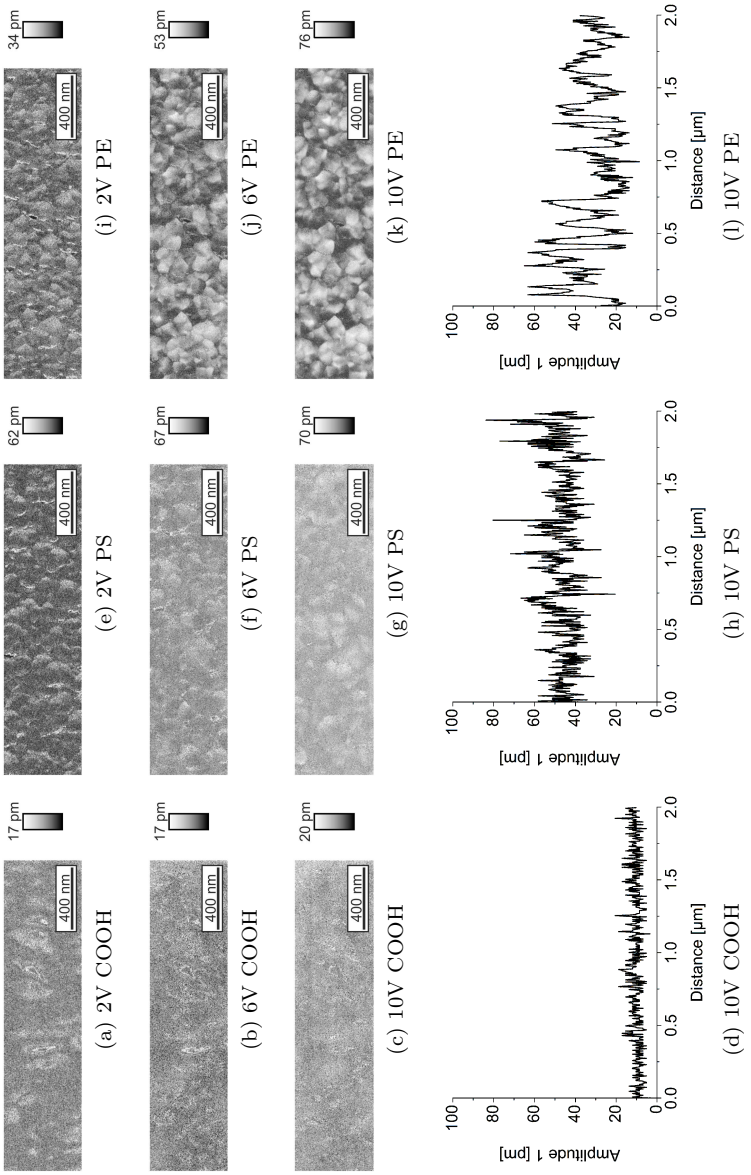

Figure 3.16: PFM images obtained on ZnO films deposited onto a COOH-terminated SAM (a-c), PS (e-g) and PE (i-k) and line profiles of the images at 10 V (d,h,l).

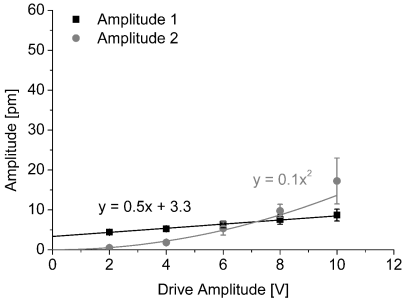

(a) COOH

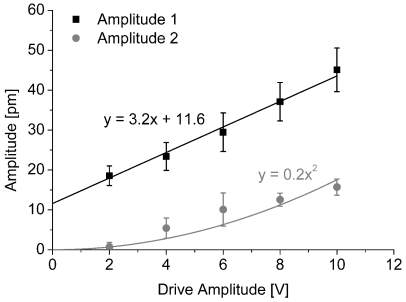

(b) PS

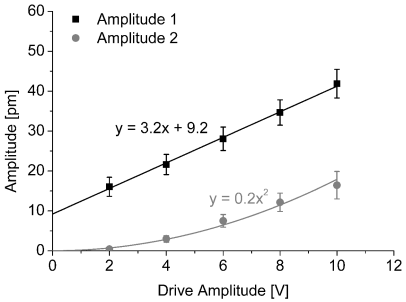

(c) PE

Figure 3.17: The average piezoelectric (amplitude 1) and electrostrictive (amplitude 2) response plotted against the drive amplitude for the ZnO films deposited onto a) a COOH-terminated SAM, b) PS brushes and c) PE layers.

The linear correlation of the amplitude 1 signals and the parabolic graph of the amplitude 2 signals with the drive amplitude coincide with the theoretical description from the equations 1.7 and 1.8 [49]:

$$\Delta z_\omega = d_{\text{eff}} V_\omega + 2\frac{M_{333}}{t} V_{\text{DC}} V_\omega \tag{1.7}$$

$$\Delta z_{2\omega} = \frac{M_{333}}{2t} V_\omega^2. \tag{1.8}$$

On the COOH-terminated SAM, the electrostrictive signal prevails over the piezoelectric signal at higher drive amplitudes. This indicates that the measured signal cannot be described as piezoelectric behavior. Additionally, the value of $0.5\,\text{pm}\,\text{V}^{-1}$ for the effective piezoelectric coefficient corresponds to the reference value of the non-piezoelectric pure silicon wafer [158]. This again agrees with the non-textured morphology of the ZnO film. The extrapolated offset at 0 V drive amplitude arises from a system inherent background noise and is measured on all samples.

In the case of ZnO on PS, both curves deviate from the ideal behavior, i.e. the amplitude 1 curve is not linear and the amplitude 2 curve does not show a parabolic trend. Still, the measured piezoelectric response is higher than the electrostrictive part. Therefore, it can be concluded that here, the measured response comes from the piezoelectric character of the ZnO film.

The sample with the most ideal behavior is the ZnO film on the PE. As for the sample on PS, the piezoelectric part dominates the overall response of the film. For both samples, an effective piezoelectric constant of $3.2\,\text{pm}\,\text{V}^{-1}$ can be calculated from the slopes of the amplitude 1 curves. According to Kalinin et al. [128], d_{33} can be estimated to be

$$d_{33} \approx 2 d_{\text{eff}} \tag{1.6}$$

if the AFM tip is used as a top electrode. In these measurements, this gives a d_{33} of $6.4\,\text{pm}\,\text{V}^{-1}$ for the ZnO films deposited onto PS brushes

and PE multilayers. Compared to single crystalline samples ($9.9\,\mathrm{pm\,V^{-1}}$ [1, 4]), this value is slightly lower. This is evident due to the nanocrystalline character of the films obtained in this work. Although there is a preferred orientation present, not all crystallites are oriented along the (002) direction since the $T_C(002)$ values are quite small. The response is decreased by the counteracting deformation of a part of the crystallites. However, the response is comparable to the one of ZnO films deposited with other methods like radio frequency magnetron sputtering or sol-gel processes. In literature, values between $2\,\mathrm{pm\,V^{-1}}$ and $13\,\mathrm{pm\,V^{-1}}$ were reported for such films [51, 52].

3.5 Deposition of ZnO thin films doped with Al, Ga and In

The template-directed bioinspired mineralization of ZnO thin films was a first step towards nanoscaled electronic devices. Another important factor on this way concerns the electrical conductivity and the optical properties of the ZnO. To achieve high carrier concentrations and to tune the optical band gap, n-type doping with group III elements was performed. For this purpose, precursor salts of Al, Ga and In were added to the ZnO deposition solution in order to allow incorporation of these impurity ions into the ZnO lattice. In this chapter, the doping solutions as well as the growth, the composition, the optical and electrical properties of the deposited films were investigated.

3.5.1 Solution chemistry of the deposition solutions with Al, Ga and In

To achieve various doping contents, different amounts of Al, Ga or In nitrate were added to the zinc acetate stock solution. Afterwards, the ZnO deposition solutions were mixed according to recipes S1 for Al doping and S2 for Ga and In doping as described in the experimental section 2.2.3. In contrast to the undoped solution, turbidity was observed for some of the stock and deposition solutions (see table 3.3). A very fine, white powder precipitates at higher doping contents of all three elements. The stock solutions containing 2 mol % or more Al or Ga as well as all In containing stock solutions were turbid. To retard the precipitation process, the stock solutions were stored at 4 °C and shaken before use. During preparation of the deposition solutions, the precipitate redissolved in some of the solutions so that clear solutions were obtained for lower Al and Ga doping contents (2 mol %, 4 mol %, 5 mol %, 10 mol %, 15 mol % and 20 mol % Al and 1 mol %,

Table 3.3: Summary of the stock/deposition solutions containing Al, Ga or In that are clear (-) or show turbitity (+).

	Doping concentration [mol %]										
	0	1	2	3	4	5	10	15	20	30	50
Al	-/-	-/-	-/-	+/-	+/-	+/-	+/-	+/-	+/-	+/+	+/+
Ga	-/-	+/-	+/-	+/-	+/+	+/+					
In	+/+	+/+	+/+	+/+							

2 mol % and 3 mol % Ga) (table 3.3).

The analysis of the precipitate composition in case of In and Al stock solutions was not possible due to the low amount. In the case of Ga doping, the precipitate from the stock solutions containing 4 mol % and 5 mol % gallium, could be extracted. Here, ICP-AES measurements showed that the precipitate consists mostly of gallium and only a very low amount (< 1 wt.%) of Zn was found.

Additionally, the pH of the deposition solutions was measured. For doping contents up to 10 mol %, the pH is nearly constant and between 8.8 and 8.9 (see figure 3.18). With increasing Al content, the pH decreases continuously until a pH as low as 7 is found for 50 mol % Al.

A possible explanation for this behavior can be found in the formation of insoluble hydroxides of the doping elements. The higher the doping content, the higher the amount of hydroxides formed and the more OH^- ions are removed from solution.

To check this hypothesis, stability diagrams of different species in solution in dependence on the pH were calculated (figure 3.19) with the software *ChemEQL v3.1* (eawag). The fraction f gives the amount of an element M(III) present in the respective species. For example, $f(M(OH)_3(aq))$ is

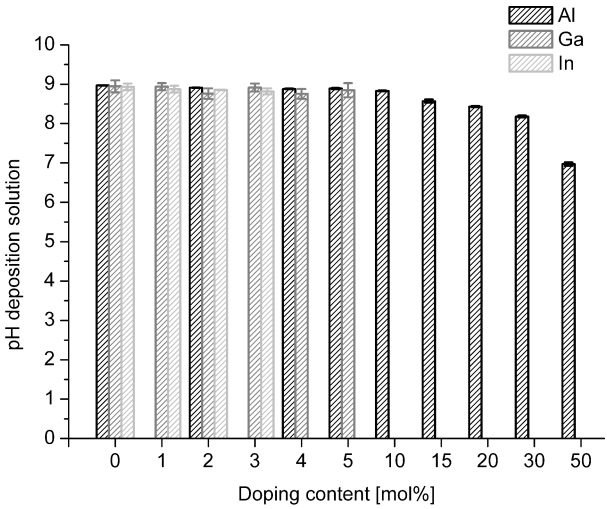

Figure 3.18: pH values of the deposition solutions containing different amounts of Al (black), Ga (dark grey) or In (light grey).

Table 3.4: Complex formation constants K for different species with Zn and M = Al, Ga or In. [191–193]

Complex formation reaction	$\log K$			
	Zn	Al	Ga	In
$Zn^{2+} \rightleftharpoons H^+ + Zn(OH)^+$	-9.0			
$Zn^{2+} \rightleftharpoons 2H^+ + Zn(OH)_2$	-16.9			
$Zn^{2+} \rightleftharpoons 3H^+ + Zn(OH)_3^-$	-28.4			
$Zn^{2+} \rightleftharpoons 4H^+ + Zn(OH)_4^{2-}$	-41.2			
$M^{3+} \rightleftharpoons H^+ + M(OH)^{2+}$		-5.0	-3.1	-4.4
$M^{3+} \rightleftharpoons 2H^+ + M(OH)_2^+$		-10.1	-6.7	-8.3
$M^{3+} \rightleftharpoons 3H^+ + M(OH)_3(aq)$		-16.9	-11.1	-12.4
$M^{3+} \rightleftharpoons 4H^+ + M(OH)_4^-$		-22.7	-17.1	-22.1

given as

$$f\left(M(OH)_3(aq)\right) = \frac{[M(OH)_3(aq)]}{[M(III)]} \times 100. \tag{3.2}$$

Since complex formation constants K in methanol are rare, the calculations were carried out with solublitity constants available for aqueous solutions (see table 3.4). [191–193]

The diagrams show the stable species in the three solutions containing 2 mol % of the doping elements. By choosing the same concentration, it is possible to compare the solution chemistry of all three elements. At the pH of the deposition solutions (8.8 and 8.9), only two stable species are present, namely $M(OH)_3(aq)$ and $M(OH)_4^-$. Their relative amounts are listed in table 3.5. The other species are stable at lower pH values only.

According to Baes and Mesmer $Al(OH)_3$ is amphoteric. [191] This means, it dissolves in acidic and alkaline media. At the basic pH of 8.9 of the deposition solution, 0.1 % of the Al(III) exists as $Al(OH)_3(aq)$ which can precipitate and form the solid hydroxide. At higher doping contents, the pH of the solution decreases. The stability diagram shows that in this case, more $Al(OH)_3(aq)$ is formed. This confirms the observation that the

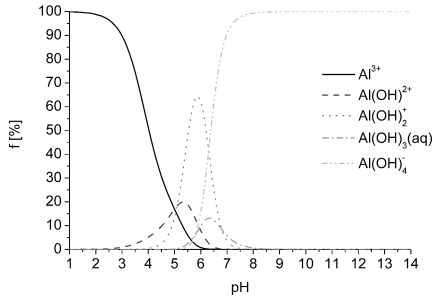

(a) Al(III)

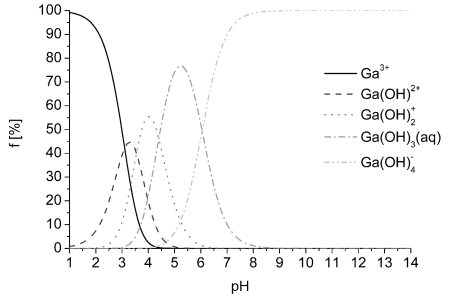

(b) Ga(III)

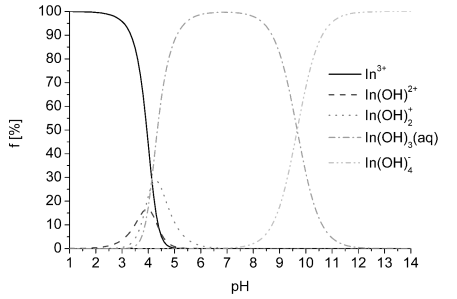

(c) In(III)

Figure 3.19: Solubility diagrams for fractions f of (a) Al(III), (b) Ga(III) and (c) In(III) existing as M^{3+}, $M(OH)^{2+}$, $M(OH)_2{}^{+}$, $M(OH)_3$(aq) and $M(OH)_4{}^{-}$. The calculations were performed for solutions containing 2 mol % Al, Ga or In.

Table 3.5: Relative amounts of the most stable species in solutions containing 2 mol % of Al, Ga or In that were calculated with *ChemEQL* at the pH of the corresponding deposition solutions.

Doping element	pH of the deposition solution	$f(M(OH)_3(aq))$ [%]	$f(M(OH)_4^-)$ [%]
Al	8.9	0.1	99.9
Ga	8.8	0.2	99.8
In	8.9	85.5	14.5

amount of precipitate increases with increasing doping content.

Similar behavior is also observed for Ga doping. $Ga(OH)_3$ is still amphoteric, but with a tendency to a more basic character. [191] Thus, the salt is less soluble under alkaline conditions. This also reflects in the solubility diagram. The fraction of $Ga(OH)_3(aq)$ is slightly higher compared to $Al(OH)_3(aq)$ ($f\,(Ga(OH)_3(aq)) = 0.2\,\%$). Compared to $Al(OH)_3(aq)$, $Ga(OH)_3(aq)$ is still stable at higher pH values. Therefore, the insoluble hydroxide is also formed in solutions with lower doping contents.

In contrast to this, $In(OH)_3$ shows a very broad range of stability. The relative amount of $In(OH)_3(aq)$ is 85.5 % at the pH of the deposition solution. This correlates with the precipitation observed in all deposition solutions.

In summary, the tendency to form insoluble salts under the conditions in the deposition solution increases from Al and Ga to In. Therefore, precipitation already occurs for low concentrations of In, while it is only observed for high concentrations of Al.

The formation of insoluble hydroxides can also account for the decrease in pH of the Al containing deposition solutions with increasing doping content (figure 3.18). To increase the doping content, more aluminum nitrate is added to the solution. This leads to the formation of more insoluble

$Al(OH)_3$. Calculations show that for 2 mol % Al in solution, $f(Al(OH)_3)$ is only 0.1 % whereas it increases to 5.7 % for the solution with 50 mol % Al. By removing the insoluble species from the solution, there are less OH^- ions present and the pH decreases from 8.9 (2 mol % Al) to 7.0 (50 mol % Al).

3.5.2 Deposition of Al-doped ZnO films

ZnO films doped with different amounts of Al were deposited on APTES modified substrates with deposition solutions prepared according to recipe S1 (see experimental part 2.2.1). The samples were characterized after 40 deposition cycles.

To characterize these aluminum-doped ZnO (AZO) samples, XRD measurements were carried out. Figure 3.20 shows the reflections of wurtzite-type ZnO for all, but the 50 mol % sample. According to PDF card no. 1011258, the reflections at 32.1°, 34.5° and 36.5° 2θ can be assigned to the 100, 002 and 101 reflections, respectively. There are no diffraction lines of further crystalline phases visible in the diagram. For the sample with 50 mol % Al, no crystalline phase could be detected at all.

Starting from 15 mol % Al, a 002 texture is observed. The texture coefficients $T_C(002)$ are 1.22, 1.55 and 2.08 for the 15 mol %, 20 mol % and 30 mol % Al samples, respectively. This can be explained by the introduction of water into the deposition solution. Stitz et al. [158] observed that ZnO films deposited in the presence of small amounts of water exhibit a 002 texture. Similar results were also obtained by Wang et al. [194, 195] They observed a change in the shape of ZnO crystallites upon addition of small amounts of water into a methanolic deposition solution. They concluded that the water adsorbs to the polar (0001) and $(000\bar{1})$ crystal planes and inhibits the growth in these directions. The resulting particles are less rod-like shaped and can more easily attach to the surface in an oriented way as is shown in figure 3.21. [194, 195] The Al precursor salt used for the

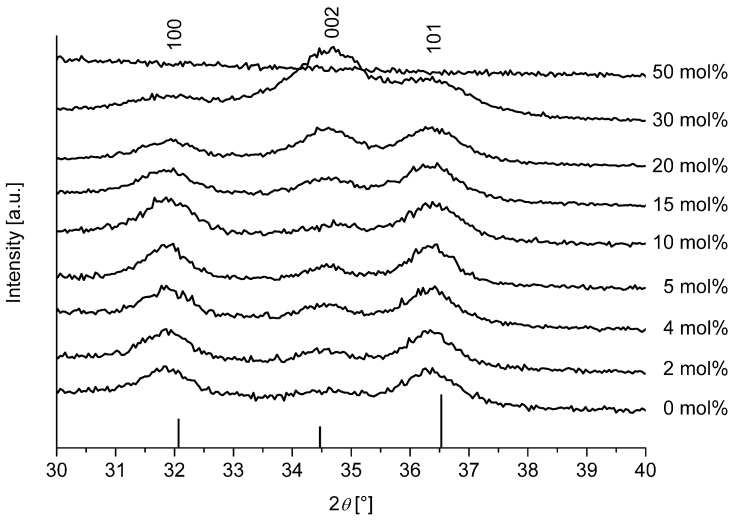

Figure 3.20: XRD diagrams of the samples mineralized for 40 deposition cycles from solutions containing 0 mol % to 50 mol % Al. The line diagram at the bottom shows the reflections and relative intensities of wurtzite-type ZnO according to PDF card no. 1011258.

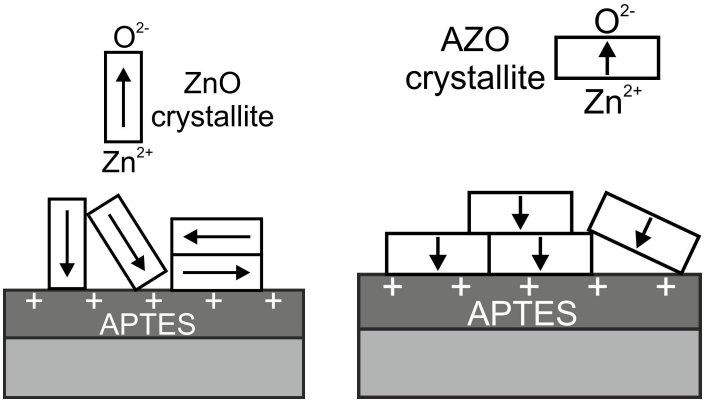

(a) (b)

Figure 3.21: Schematic representation of the attachment process of ZnO crystallites with different shapes. a) The undoped deposition solution does not contain any water. The shape of the crystallites is more rod-like. b) The deposition solution with Al contains water which caps the crystal growth and the AZO crystallites have a more plate-like shape. This shape supports the formation of a textured film.

doping experiments is aluminum nitrate nonahydrate. This means, 9 mol water are added to the deposition solution for every mol of Al^{3+}. The water can cap the crystal growth along the (002) direction, leading to a more plate-like crystallite shape. The area of the polar crystallite faces is higher compared to that of the rod-like shape. Therefore, the interaction of these faces with the template is increased. The crystallites can attach more easily to the surface in an oriented way and the observed 002 texture arises.

In addition to phase identification, volume weighted crystallite sizes can be calculated from the integral breadth of the reflections *via* Scherrer equation 1.11 (figure 3.22). The crystallite size increases slightly from 8.9 nm to 10.7 nm for 0 mol % to 5 mol % Al. This can be correlated with the increasing

water content in the solution. A. Greß measured in his bachelor's thesis the crystallite sizes for deposition solutions containing different amounts of water. It was found that the crystallite size increases with increasing water content.[175] This result is also supported by other research groups that compared the mineralization behavior of ZnO crystallites from solutions with and without water. [194–196] The hydrolyzation rate increases in the presence of water, compared to pure methanol. Therefore, the formation of zinc hydroxides that act as precursors for ZnO mineralization increases. As a result, the crystallite growth rate increases and larger crystallites are formed. [194–196] Starting from 10 mol % Al in the deposition solution, the crystallite size decreases with increasing doping content. At 30 mol %, the crystallite size is as low as 7.3 nm. In this concentration range, the increase in crystallite size caused by the introduction of water might be counteracted by the increasing amount of Al that is incorporated into the films. Al^{3+} ions (ionic radius = 0.53 Å) are smaller than Zn^{2+} ions (0.74 Å). [197] Incorporation of the doping element into the ZnO lattice leads to internal stresses that are reported to hinder crystallite growth. [198–204]. Additionally, other research groups found that ions or counter ions can act as capping agents that reduce the crystallite growth. [47, 205, 206]

For structure investigations, SEM and AFM measurements were carried out (figures 3.23 and 3.24). The images of the samples up to 30 mol % show homogeneous films that consist of nanoparticles of around 10 nm in size. These particles form aggregates with diameters between 100 nm and 1 µm. For the sample with 50 mol % Al in solution, there is only a thin film visible in the AFM image (figure 3.24h) which cannot be detected by SEM (figure 3.24g). The drastic decrease in film thickness can be explained by the low pH of 7.0 of the deposition solution (compare chapter 3.5.1). The stability diagram shows that $Zn(OH)_2$ is not stable at this pH. [70] According to Lipowsky et al., this species is a precursor for the formation of ZnO. If this precursor is not stable, the amount of ZnO that is precipitated decreases

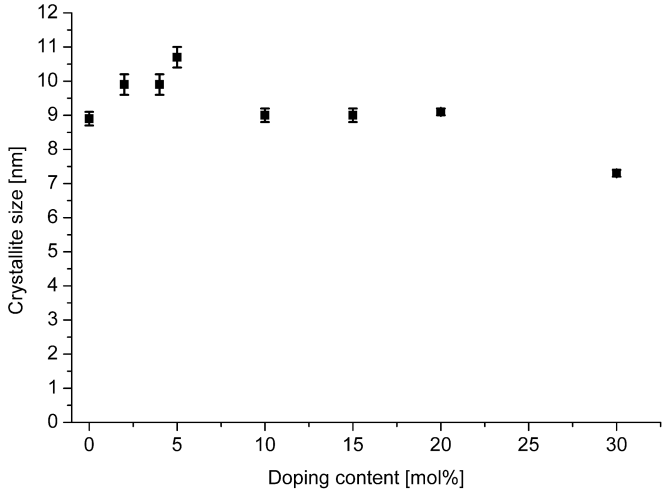

Figure 3.22: Crystallite sizes calculated from XRD data of the AZO thin films in dependence on the doping content.

and only a thin film is deposited which also cannot be detected by XRD (compare figure 3.20).

The thickness of the films was determined from the SEM cross sections. The summarized results in figure 3.26 show that the film thickness increases strongly from 111 nm for the undoped sample to 1161 nm for the 30 mol % with increasing amount of Al in the deposition solution. This high thickness of the latter film induces mechanical stresses which cause cracking and delamination of the film from the substrate (compare figures 3.24e and 3.25).

Similar to the crystallite sizes, the high increase of the film thickness can be explained by the introduction of water into the deposition solution by adding the aluminum precursor. Becheri et al. and Wang et al. investigated the influence of water on the mineralization of ZnO nanoparticles. [194–196] They found that the rate of hydrolysis of the Zn precursor is higher in the presence of water and more ZnO is precipitated. Therefore, the increasing film thickness with increasing amount of Al in solution could be a result of the same effect. A second effect that can support the film growth is the decrease in crystallite size, especially for the 30 mol % sample, where the crystallite size is only 7.3 nm. To minimize the surface energy, the particles tend to agglomerate. These agglomerates help forming thicker films.

The composition of the films was determined by ICP-AES measurements. The amount of Al incorporated into the film is very low. For 30 mol % Al in the stock solution, only 0.7 mol % Al can be traced in the deposited film. This is near the detection limit of the spectroscopic technique and therefore, films with lower Al contents could not be analyzed. An explanation for this observation is the high difference in ionic radii between Al^{3+} (0.53 Å) and Zn^{2+} (0.74 Å). [197] The lattice distortion upon substituting Zn^{2+} by Al^{3+} is very high. As a consequence, incorporation of the doping element into the lattice is inhibited.[207] In the same way, the solubility limits reported for Al in ZnO are low (0.3 mol % to 3.6 mol %). [32, 208–210]

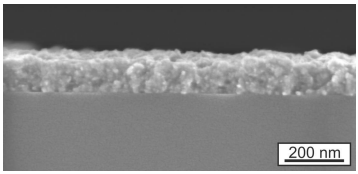

(a) 0 mol % Al

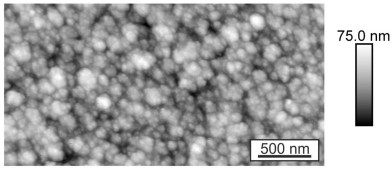

(b) 0 mol % Al

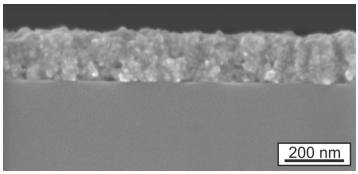

(c) 2 mol % Al

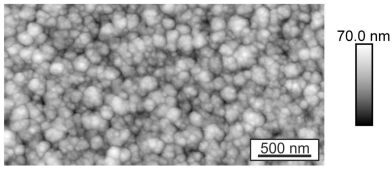

(d) 2 mol % Al

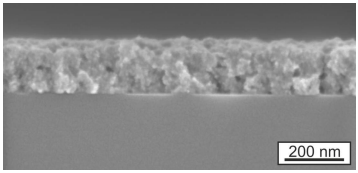

(e) 4 mol % Al

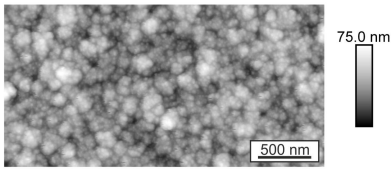

(f) 4 mol % Al

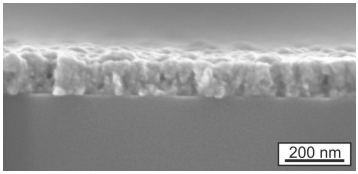

(g) 5 mol % Al

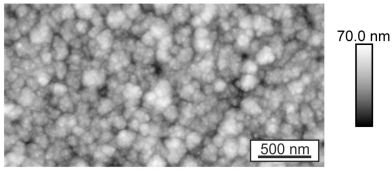

(h) 5 mol % Al

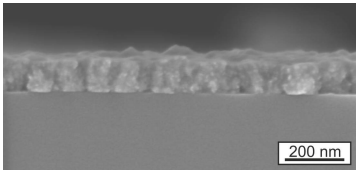

(i) 10 mol % Al

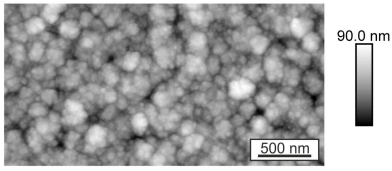

(j) 10 mol % Al

Figure 3.23: SEM cross sections (a,c,e,g,i) and AFM images (b,d,f,h,j) of the samples without Al and with Al contents up to 10 mol %. The films were deposited for 40 cycles onto APTES modified substrates.

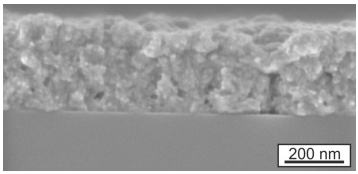

(a) 15 mol % Al

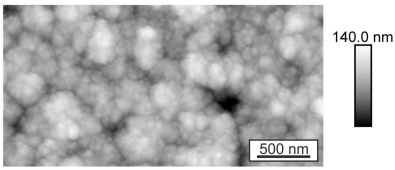

(b) 15 mol % Al

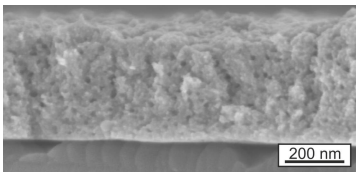

(c) 20 mol % Al

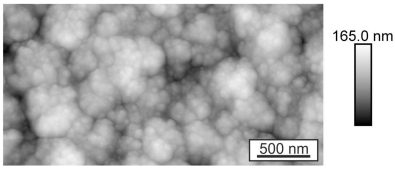

(d) 20 mol % Al

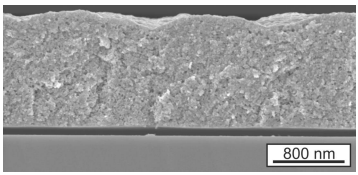

(e) 30 mol % Al

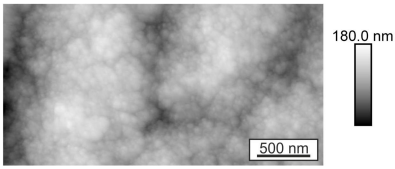

(f) 30 mol % Al

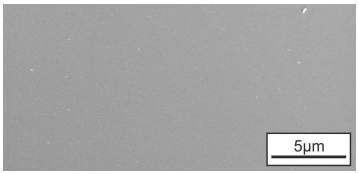

(g) 50 mol % Al

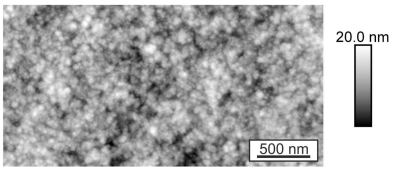

(h) 50 mol % Al

Figure 3.24: SEM cross sections (a,c,e), SEM top view (g) and AFM images (b,d,f,h) of the samples with Al contents between 15 mol % and 50 mol % deposited for 40 cycles onto APTES modified substrates.

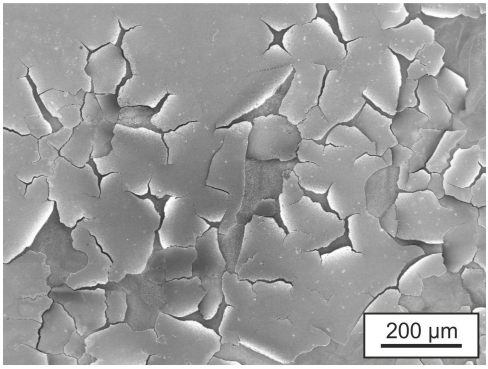

Figure 3.25: SEM top view of the 30 mol % AZO film deposited for 40 cycles. The cracks show that the film delaminates from the substrate due to high internal stresses generated by the high thickness of 1.16 µm (see also figure 3.24e).

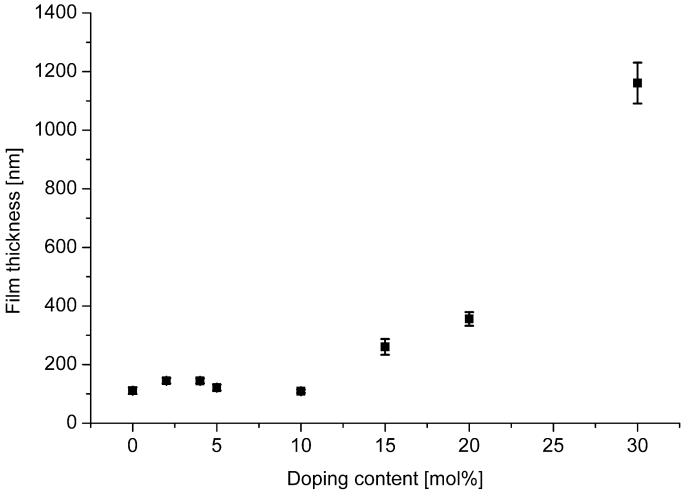

Figure 3.26: Film thickness of the Al-doped ZnO films in dependence on the doping content.

Additionally, XPS measurements were carried out on the 30 mol % and 50 mol % Al samples. Figure 3.27 shows the Zn $2p_{2/3}$, O 1s and Al 2p peaks after 30 s sputtering with Ar to ensure a clean sample surface. To normalize the spectra, the binding energies were shifted so that the Zn $2p_{2/3}$ peak is located at 1021.9 eV. [9, 65, 211, 212]

The fitted peak positions are listed in table 3.6. The positions of the Zn $2p_{2/3}$ peak at 1021.9 eV of both samples correspond to that of ZnO. [83, 213–216] The Zn $2p_{2/3}$ peak of the 30 mol % Al sample is accompanied by a low intensity peak at 1025.2 eV (figure 3.27a) indicating the presence of residual zinc acetate.[217] The O 1s peak can be split into three components. The first component at the lowest binding energy can be attributed to O^{2-} in ZnO. [213–216, 218–221] The second component at the middle binding energy can be correlated with oxygen in an oxygen deficient ZnO matrix. The third peak is ascribed to chemisorbed surface oxygen. [40, 212–214, 216, 221–223] The relative intensities of the three components show that the amount of oxygen in ZnO is higher for the sample with 30 mol % Al. Additionally, the intensity of the shoulder at 532.3 eV increases for the 50 mol % sample. Therefore, the amount of chemisorbed surface oxygen is lower for this sample compared to that of the 30 mol % sample. This indicates that the ZnO in the 30 mol % Al sample has better stoichiometry and less contamination on the surface which correlates with the film quality observed by SEM and XRD. The Al 2p peak of the 30 mol % and 50 mol % Al sample is positioned at 75.6 eV and 74.2 eV, respectively. This peak can be assigned with the Al-O bond. [213–216, 219–222, 224, 225] There are several possibilities, how the Al is coordinated. One assumption is that the Al is incorporated into the ZnO lattice and substitutes Zn. [211, 215, 216, 219, 224] Other research groups assume that a second phase is formed that is either Al_2O_3 [221, 225] or $ZnAl_2O_4$ [222, 226]. However, the binding energies of these components are very close and cannot be used to identify the coordination of the Al.

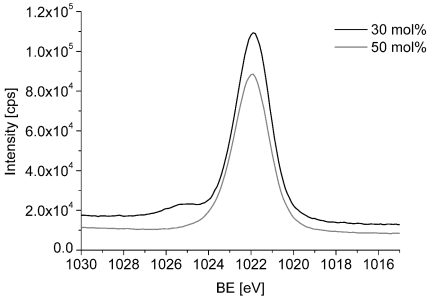

(a)

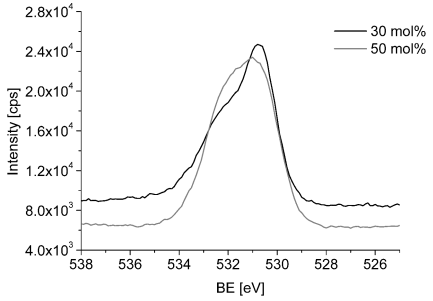

(b)

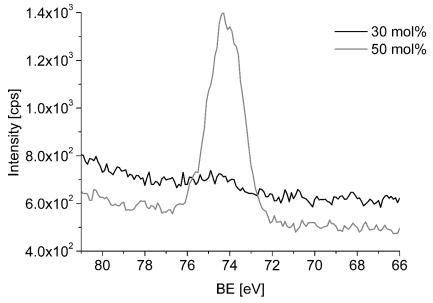

(c)

Figure 3.27: XPS spectra of a) Zn $2p_{2/3}$, b) O 1s and c) Al 2p peaks obtained on films precipitated with 30 mol % and 50 mol % Al in solution. The surface of the samples was sputtered for 30 s to remove any contamination.

Table 3.6: Binding energies of the Zn $2p_{2/3}$, O 1s and Al 2p XPS peaks of the samples with 30 mol % and 50 mol % Al.

Sample	Zn $2p_{2/3}$ [eV]		O 1s [eV]			Al 2p [eV]
30 mol % Al	1024.9	1021.9	532.3	531.0	530.4	75.6
50 mol % Al		1021.9	532.3	531.2	530.4	74.2

The influence of the Al on the optical properties of the ZnO was investigated by PL measurements. The UV band is ascribed to the near band emission of exciton-exciton recombinations. [45, 48, 227–231] Figure 3.28 shows the room temperature PL spectra of the AZO films in dependence on the doping content.

The position of the UV band depends on the crystallite size and on the doping content. The influence of the first parameter can be investigated by calculating a theoretical UV band by inserting the crystallite sizes obtained from XRD (see figure 3.22) into equation 1.13. Figure 3.29 shows the UV band position as measured by PL (black squares) and calculated from the crystallite sizes (grey circles). For the undoped ZnO sample, both values should be identical, since the only influencing parameter is the crystallite size. The difference between the calculated and measured values seen in figure 3.29 confirms that equation 1.13 is only an approximation. [146]

For doping contents lower than 10 mol % Al, the calculated band position increases from 354 nm to 357 nm. This red shift is not observed in the PL measurements. Here, the position remains at 361 nm. This indicates that the shift due to the change in crystallite size is neutralized by the incorporation of the Al into the ZnO lattice. The introduction of charge carriers raises the Fermi level into the conduction band (see chapter 1.1.1). To excite an electron into the conduction band, an energy larger than the Fermi energy is necessary. Like this, the optical band gap is larger than

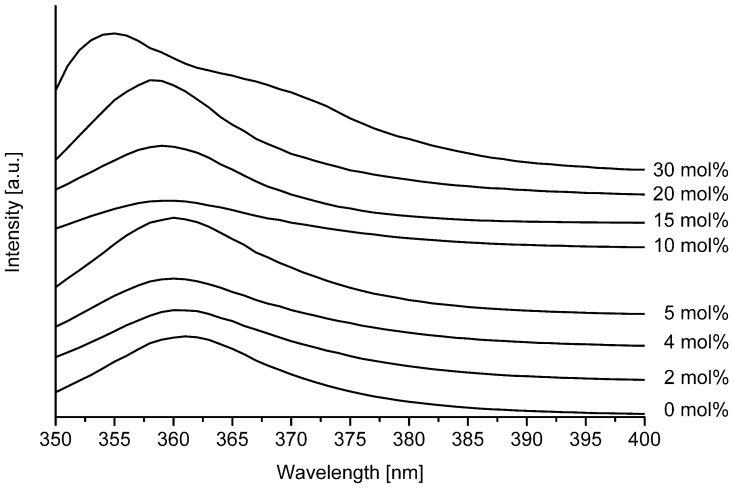

Figure 3.28: Room temperature PL spectra of the ZnO films doped with Al for various doping concentrations.

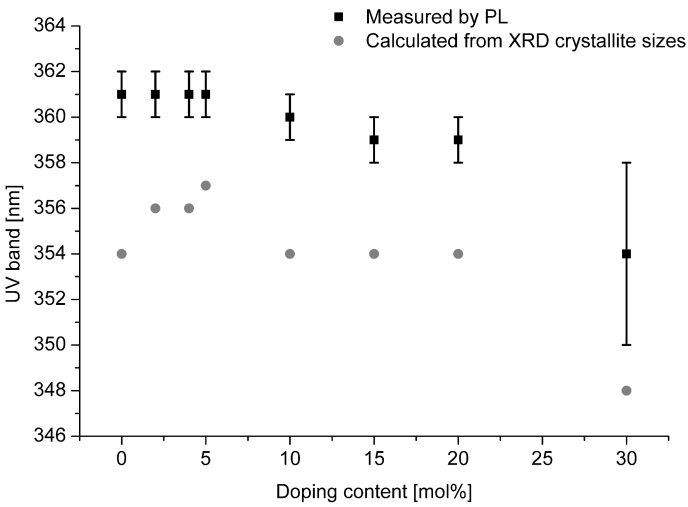

Figure 3.29: UV band position of the Al doped ZnO films in dependence on the Al content measured by PL (black squares). UV band position calculated with the crystallite sizes obtained from XRD (grey circles).

the real band gap and leads to a blue shift of the UV band in the PL spectra. This Burstein-Moss effect is often found for doped ZnO. [44–48] Starting from 10 mol % Al, the crystallite size decreases and consequently, the calculated UV band position is shifted to lower wavelengths. This blue shift coincides with the blue shift of the Burstein-Moss effect. Therefore, it is not possible to distinguish which of the two parameters acts predominantly on the UV band position.

3.5.3 Deposition of ZnO films doped with Ga and In

ZnO thin films were deposited from solutions containing Ga or In precursor salts onto substrates modified with APTES (see chapter 2.2.3). The XRD

diffractograms of the samples after 40 deposition cycles in figure 3.30 confirm the formation of ZnO for all doping concentrations, except for 5 mol % Ga and 3 mol % In. Another crystalline phase was not observed. The reflections at 32.1°, 34.5° and 36.5° 2θ represent the 100, 002 and 101 reflections of wurtzite-type ZnO (PDF card no. 1011258). Additionally, the GZO samples with 1 mol % and 2 mol % Ga exhibit a 002 texture. The corresponding texture coefficients $T_C(002)$ are 1.74 and 1.22 for the 1 mol % and 2 mol % Ga samples, respectively.

All reflections visible are considerably broadened. This indicates that the films are nanocrystalline. Indeed, the calculated volume weighted crystallite sizes (compare equation 1.11) are below 7 nm (figure 3.31). For the GZO sample, the crystallite size increases from 5 nm to 7 nm. This behavior is already known for GZO. [44, 232–235] It is explained by the formation of defects to maintain charge neutrality upon introduction of the doping element. Surface defects increase the surface energy of the crystallites or they are said to decrease the driving force for crystallization [234, 236]. Both effects inhibit nucleation and thus less, but bigger crystallites are formed. However, with increasing doping content, the crystallite growth seems to be limited. In this regime, additional effects counteract the defect mechanisms discussed by Pineda-Hernandez and Schwartz. Substitution of a Zn^{2+} ion (0.74 Å [197]) with a slightly smaller Ga^{3+} ion (0.61 Å [197]) leads to internal stresses that reduce the crystallite growth. [198–204]. Furthermore, the probability of segregation and the presence of counter ions that can act as capping agents increases as well. [47, 205, 206]

For 1 mol % In, the crystallite size increases in the same way as for GZO. Khalfallah et al. and Nunes et al. investigated IZO films and found an increase in crystallite size with increasing doping content as well. [232, 237] Khalfallah et al. discuss the increase of the lattice constant of the ZnO unit cell. Since the In^{3+} ion is slightly larger (0.76 Å [197]) than the Zn^{2+} ion (0.74 Å, there are lattice distortions. This distortion is minimized by

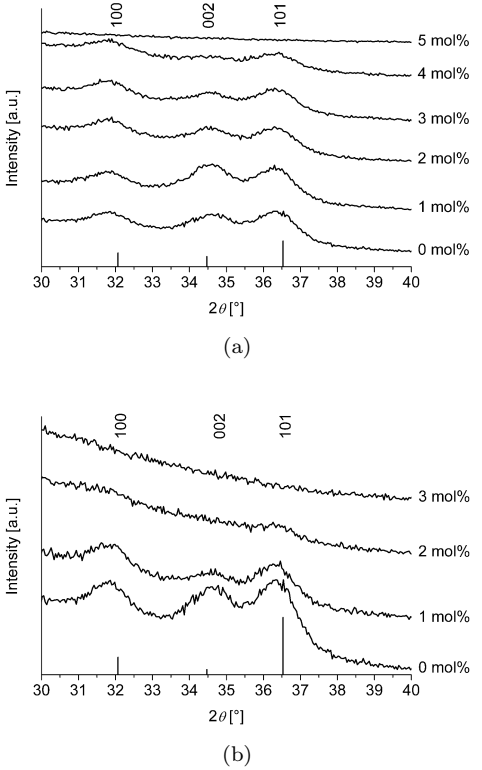

Figure 3.30: XRD results of (a) GZO and (b) IZO films after 40 deposition cycles in dependence on the doping content. The line diagrams at the bottom show the reflections and relative intensities of wurtzite-type ZnO according to PDF card no. 1011258.

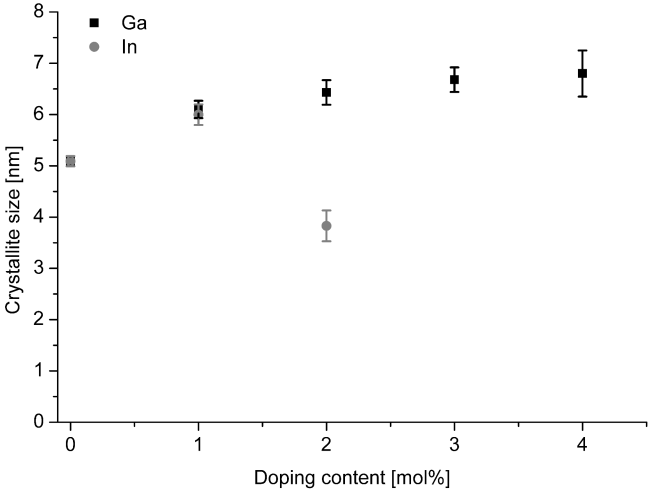

Figure 3.31: Crystallite sizes calculated from XRD data of the GZO (black) and IZO (grey) thin films in dependence on the doping content.

relaxation of the unit cell increasing the lattice parameters. [237] In addition, the mechanisms discussed by Pineda-Hernandez et al. and Schwartz et al. can contribute to the increase in crystallite size. [234, 236] They found that the nucleation of ZnO is inhibited by the introduction of defects into the ZnO lattice upon doping. These lead to a higher surface energy of the crystallites or decrease the driving force for nucleation. The number of nuclei decreases, but the formed nuclei grow faster. In contrast to the GZO results, there is a drastic decrease in crystallite size for the 2 mol % In sample. However, due to the low intensities of the corresponding XRD reflections, evaluation of the crystallite size is highly unreliable and could be the reason for this strong drop.

The structure and topography of the GZO and IZO samples were characterized by SEM and AFM measurements (figures 3.32 and 3.33). Films are

observed for the undoped ZnO film, the samples with 1 mol % to 4 mol % Ga and the 1 mol % In sample. The films are composed of nanoparticles and moderate porosity is visible. The corresponding AFM images show that there are holes present in the granular films. For higher doping contents, the film thickness decreases and the structure gets more irregular. For 2 mol % In, an island structure is observed in the SEM images (figure 3.33e). On the samples that were mineralized with the highest amount of Ga (5 mol %) and In (3 mol %) there are only isolated particles visible in the SEM cross sections (figures 3.32k and 3.33g). The AFM image of the 3 mol % In shows the structure of a very thin film with a rms roughness of (1.6 ± 0.1) nm which is higher than that of the APTES template ((0.1 ± 0.0) nm). The film is not visible in the SEM image. This could be due to the higher sensitivity against topographical features of the AFM technique.

The measured film thicknesses confirm the observations from the SEM cross sections. Figure 3.34 shows that a strong decrease in film thickness is observed upon introduction of the doping elements into the deposition solution. The thickness drops from 412 nm to 160 nm or 169 nm from undoped to GZO and IZO with 1 mol % Ga and In, respectively.

One of the possible reasons for this behavior - a change in pH of the deposition solution - can be ruled out since the pH remains the same with or without addition of the doping precursor salts (figure 3.18).

Another reason might be a change in the surface energy of the growing crystallites by the doping ions. To maintain charge neutrality, defects are formed in the ZnO lattice. Surface defects lead to an increase in the surface energy of the crystallites. [203, 238, 239] If the condition for Volmer-Weber growth is fulfilled (equation 3.3), islands form instead of a closed film:

$$\gamma_{\mathrm{APTES/ZnO}} + \gamma_{\mathrm{ZnO}} > \gamma_{\mathrm{APTES}}, \tag{3.3}$$

with the surface energies γ_{APTES}, γ_{ZnO} and the interface energy $\gamma_{\mathrm{APTES/ZnO}}$.

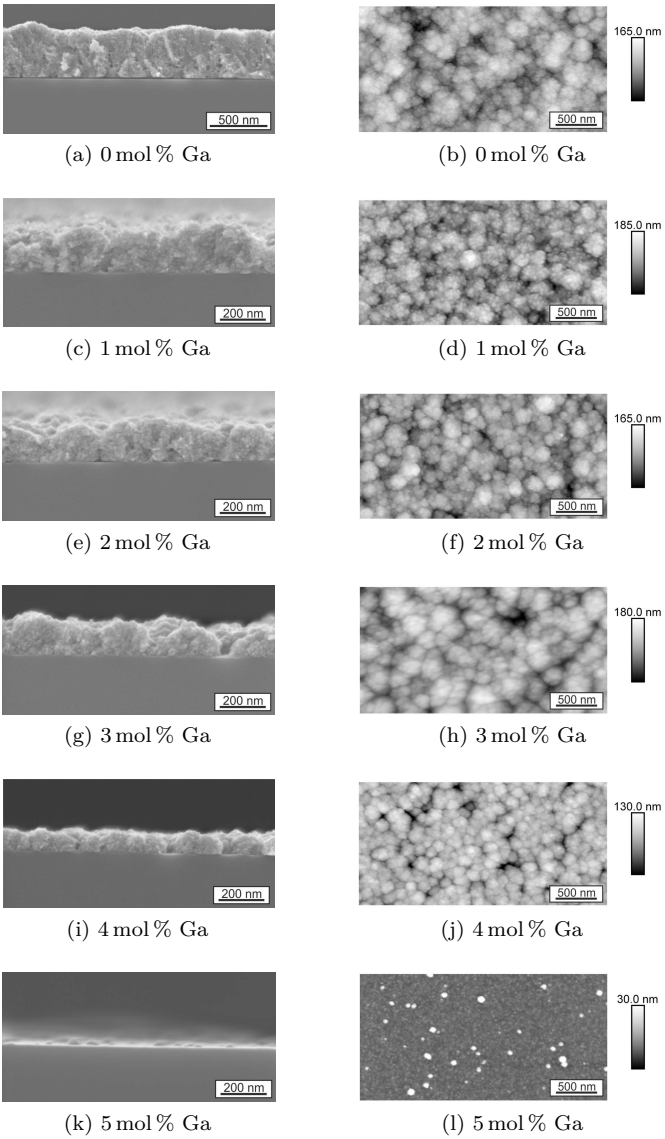

(a) 0 mol % Ga (b) 0 mol % Ga

(c) 1 mol % Ga (d) 1 mol % Ga

(e) 2 mol % Ga (f) 2 mol % Ga

(g) 3 mol % Ga (h) 3 mol % Ga

(i) 4 mol % Ga (j) 4 mol % Ga

(k) 5 mol % Ga (l) 5 mol % Ga

Figure 3.32: SEM cross sections (a,c,e,g,i,k) and AFM images (b,d,f,h,j,l) of the samples mineralized with different amounts of Ga in the deposition solution.

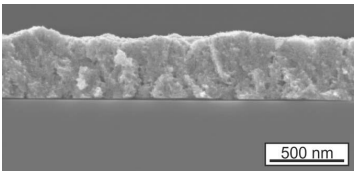

(a) 0 mol % In

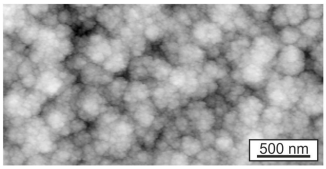

(b) 0 mol % In

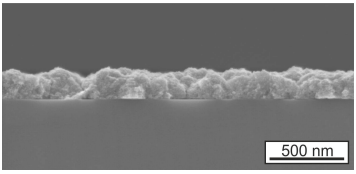

(c) 1 mol % In

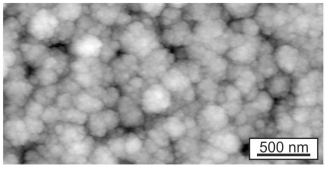

(d) 1 mol % In

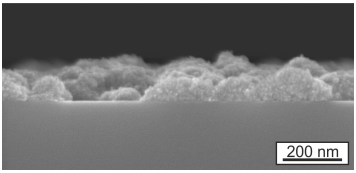

(e) 2 mol % In

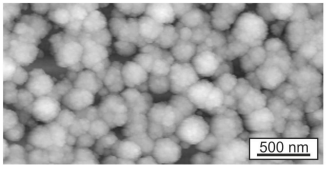

(f) 2 mol % In

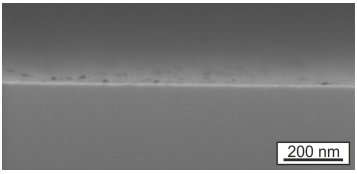

(g) 3 mol % In

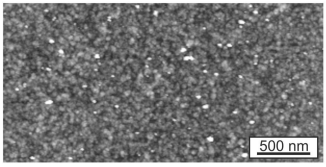

(h) 3 mol % In

Figure 3.33: SEM cross sections (a,c,e,g) and AFM images (b,d,f,h) of the samples mineralized with different amounts of In in the deposition solution.

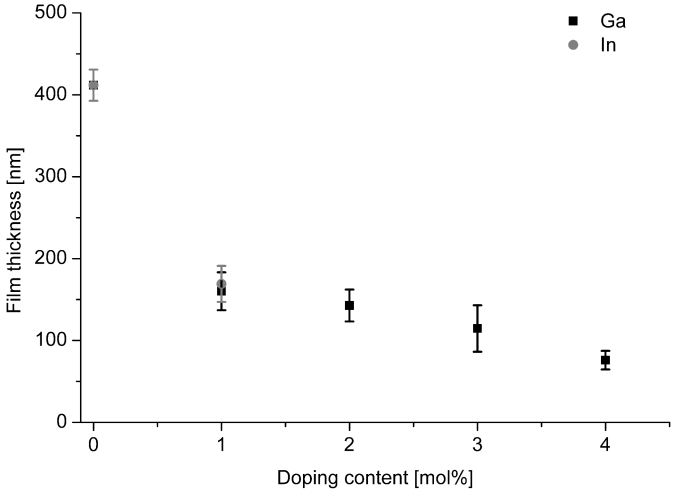

Figure 3.34: Film thickness of the ZnO films in dependence on the Ga (black) and In (grey) doping content.

A third factor that can influence the film growth can be found in the composition of the deposition solutions. At higher doping contents, precipitation was observed (compare table 3.3) which could be identified as $Ga(OH)_3$ and $In(OH)_3$ (see chapter 3.5.1). It is known that in solutions containing different species, the salt with the lowest solubility constant is precipitated first. This can even completely suppress the precipitation of a salt with better solubility. [240] Therefore, in the case of the doped deposition solutions, the precipitation of $Ga(OH)_3$ and $In(OH)_3$ could prevent the formation of the more soluble $Zn(OH)_2$. The latter is a precursor for the formation of ZnO. [68] Accordingly, ZnO film growth is inhibited, if the formation of $Zn(OH)_2$ is suppressed. The higher the doping content, the more $Ga(OH)_3$ and $In(OH)_3$ is precipitated and the smaller the amount of precipitated ZnO. Furthermore, the calculations of the stability diagrams show that $In(OH)_3$ occurs in high concentrations even for low doping contents (compare table 3.5). This could explain, why IZO film growth is only observed at 1 mol % and 2 mol % In.

The composition of the films was determined by ICP-AES measurements. Figure 3.35 shows that the $[M^{3+}]/[Zn^{2+}]$ ratio (M = Ga, In) in the films is directly correlated with the $[M^{3+}]/[Zn^{2+}]$ ratio that was present in the stock solutions. For GZO the reported solubility limits are in the range of (2 mol % to 6 mol %). [198, 201, 206, 233, 241] The content of the sample with 3 mol % in the solution (1.9 mol % in the film) is slightly below that range. Only the amount of Ga that is incorporated into the film with 4 mol % in solution (3.2 mol %) is in the range of the solubility limits. This means, the Ga^{3+} ions do not only substitute Zn^{2+} ions in the ZnO lattice, but also segregate at grain boundaries or interfaces. This is reflected in the deviation of the content in this sample from the linear trend in figure 3.35.

In the case of IZO, the amounts of In in the films are lower than the reported solubility limits (0.5 mol % to 6 mol %). [200, 230, 242] The values follow the extrapolated linear trend line. In comparison with GZO, there is

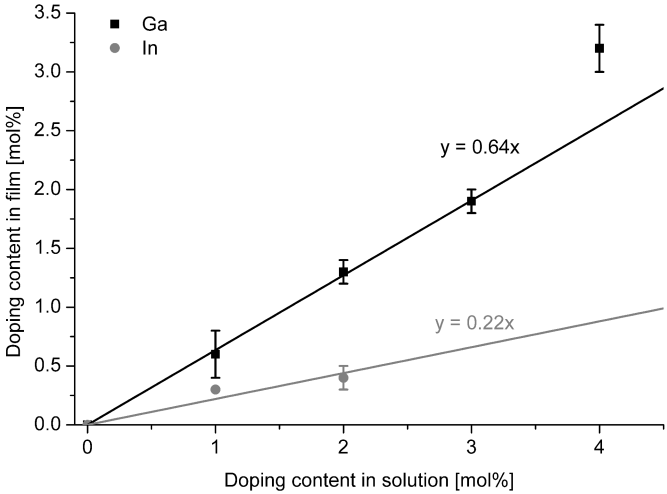

Figure 3.35: Ratio of M^{3+} (M = Ga or In) to Zn^{2+} in the films compared to the ratio in the stock solutions. The amount of the doping elements in the films was determined by ICP-AES.

less In incorporated into the ZnO. For 1 mol % Ga or In in solution, there are 0.6 mol % Ga in the film, but only 0.3 mol % of In, for example. The In^{3+} ion is larger (0.76 Å) than the Zn^{2+} ion (0.74 Å), while Ga^{3+} is smaller (0.61 Å). [197] Paul et al. found that incorporation of the larger In^{+3} ion increases the internal stresses in the ZnO lattice more than for Al^{+3} or Ga^{+3}. [223] This indicates that the incorporation of the larger ion is more difficult compared to the smaller one and can explain the lower In contents found by the ICP-AES measurements.

PL measurements were carried out to characterize the optical properties of the different GZO and IZO films. The recorded spectra are shown in figure 3.36. The intensity of the UV emission band depends on the doping concentration and consequently on the number of charge carriers. The

higher this number, the more exciton recombinations can be activated and the more light is emitted. [46, 48] However, the spectra of the GZO and IZO films show that the UV band intensity decreases with increasing doping content (figure 3.36). This might be correlated with the occurrence of nonradiative transitions that counteract the exciton emission. [46, 243–248] Ko et al. suggested that Auger recombinations compete with radiative transitions in GZO and lower the emission efficiency.[245] Additionally, defects that are introduced by doping can act as traps for electrons that are not available for recombination processes anymore. [46, 243, 246, 248] A third reason for the quenching can be the presence of impurity atoms that act as scattering centers. [45, 248]

Further information about the influence of the doping on the optical properties of the films can be gained by plotting the position of the UV band versus the doping content (figure 3.37). A blue-shift with increasing doping content was observed for GZO and IZO films. This effect is caused by the Burstein-Moss shift (see chapter 1.1.1). [44–48] An increased number of charge carriers introduced by doping lifts the Fermi level into the conduction band. Electrons that are excited have to be raised to energy levels above the Fermi energy. Therefore, the energy difference is higher compared to the undoped case. Accordingly, the emitted light is shifted to lower wavelengths.

The influence of the crystallite size is a competing effect to the Burstein-Moss shift. Equation 1.13 shows that the UV band position is inversely proportional to the crystallite radius. The calculated crystallite sizes for the samples increase with increasing doping content (figure 3.31). The UV band should be shifted to higher wavelengths accordingly. This is contradictory to the PL results and shows that the influence of the doping elements *via* the Burstein-Moss shift prevails over that of the crystallite size.

Van der Pauw measurements were performed on the GZO and IZO samples to determine the electrical properties of the doped ZnO films. The results are shown in figure 3.38. Reference measurements on the Si-substrate

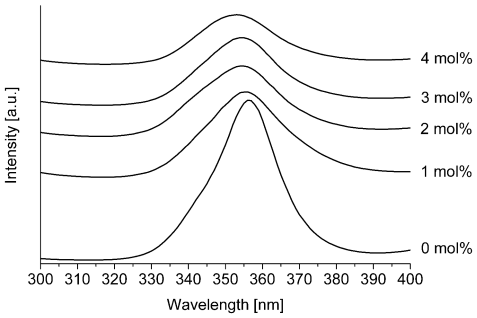

(a)

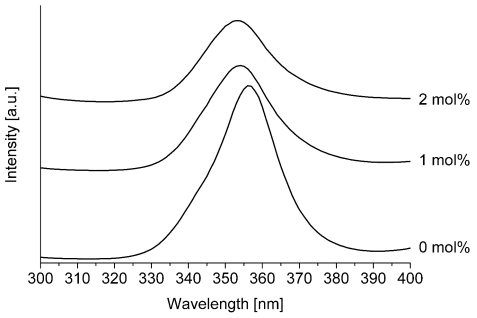

(b)

Figure 3.36: Room temperature PL spectra of the films doped with Ga (a) and In (b).

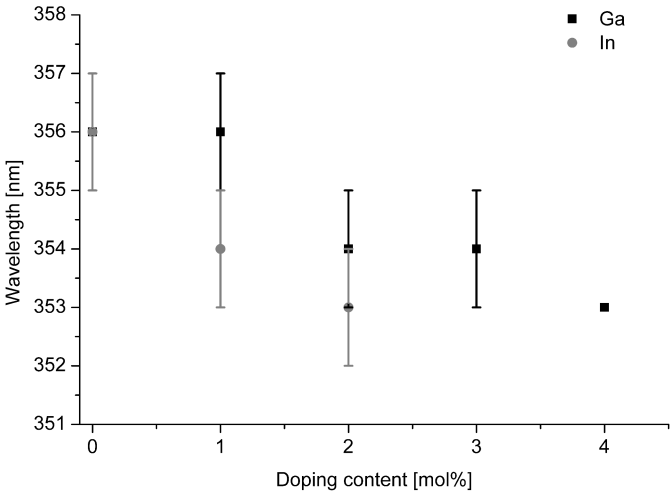

Figure 3.37: Position of the UV band of ZnO in dependence on the doping content.

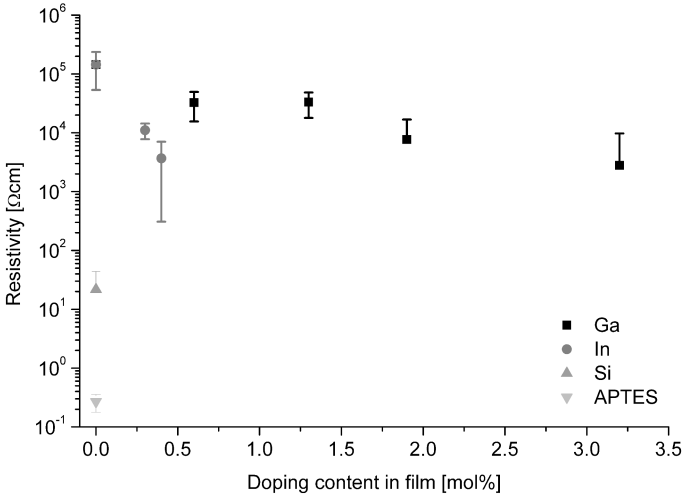

Figure 3.38: Results of the van der Pauw measurements on the Si substrate (diamond), the substrate modified with APTES (triangle) and the GZO (squares) and IZO films (circles). The lower value of the standard deviations for the Si substrate ($(22 \pm 22)\,\Omega\,\mathrm{cm}$), the 1.9 mol % ($(7.7 \pm 9.1) \times 10^3\,\Omega\,\mathrm{cm}$) and 3.2 mol % ($(2.8 \pm 7.0) \times 10^3\,\Omega\,\mathrm{cm}$) cannot be shown in the logarithmic plot since the corresponding values are negative.

and the APTES coated substrates were carried out as well.

It is important to note that the sheet resistance measured on all ZnO films is higher by several orders of magnitude compared to the values obtained on the pure substrates. This indicates that the substrate does not contribute to the conductivity. Else, the same resistance would be measured on all samples, since the current pathways usually form in the material with lowest resistivity, which would here be the substrate.

In general, the high standard deviations show that the variation in resistance is quite high. Especially for the highest doping contents, the

standard deviation is in the range of the measured value (0.4 mol % In: $(3.7 \pm 3.4) \times 10^3\,\Omega\,\mathrm{cm}$) or even higher than the measured value (1.9 mol % Ga: $(7.7 \pm 9.1) \times 10^3\,\Omega\,\mathrm{cm}$ and 3.2 mol % Ga: $(2.8 \pm 7.0) \times 10^3\,\Omega\,\mathrm{cm}$). This is correlated with the deterioration of the film quality. [249] The SEM images in figures 3.32 and 3.33 illustrate that the film thickness decreases and the films are less homogeneous. Therefore, the measured resistance changes when changing the sample orientation.

Furthermore, the resistance of the ZnO films is high ($2.8 \times 10^3\,\Omega\,\mathrm{cm}$ to $1.4 \times 10^5\,\Omega\,\mathrm{cm}$). There are only few reports of resistances for samples doped with Al, Ga or In comparable to those in this work. [204, 210, 249, 250] More typical values lie in the range of $3.5 \times 10^{-3}\,\Omega\,\mathrm{cm}$ to $2.0 \times 10^3\,\Omega\,\mathrm{cm}$ for GZO and between $5.5 \times 10^{-3}\,\Omega\,\mathrm{cm}$ and $5.0 \times 10^3\,\Omega\,\mathrm{cm}$ for IZO. There are different mechanisms discussed for such a discrepancy in electrical resistance. One of the main issues is the crystallite size of the films. XRD measurements showed that the crystallite size of the GZO and IZO samples is below 7 nm and therefore very small (see chapter 3.31). The smaller the crystallites, the more grain boundaries are present in the material. These structures cause scattering of the charge carriers an consequently decrease their mobility. The resistivity is inversely proportional to the mobility and increases, if the latter decreases. [198, 201–204, 248, 250–253] Another parameter that influences the electrical resistance is the porosity of the films. [201, 202, 252] Pores act as traps for free electrons and as barriers for electron transport. Again, the mobility of the charge carriers decreases and the resistivity increases. [201] As was observed by SEM, the films in this work show moderate porosity, which can contribute to the decreased charge transport (see figures 3.32 and 3.33). Additionally, for higher doping contents, the film thickness is quite low and the films resemble islands that are loosely connected. Both can be reasons for the low conductivity as well. [249]

Nevertheless, there is a strong decrease in electrical resistance observed

for the GZO and IZO samples. Compared to the high resistance of undoped ZnO of $(1.4 \pm 0.9) \times 10^5\,\Omega\,\mathrm{cm}$ the resistance drops to $(3.3 \pm 1.7) \times 10^4\,\Omega\,\mathrm{cm}$ for the 0.6 mol % Ga film and to $(1.1 \pm 0.3) \times 10^4\,\Omega\,\mathrm{cm}$ for the 0.3 mol % In film. The lowest values that were obtained are $(2.8 \pm 7.0) \times 10^3\,\Omega\,\mathrm{cm}$ for the 3.2 mol % Ga film and $(3.7 \pm 3.4) \times 10^3\,\Omega\,\mathrm{cm}$ for the 0.4 mol % In film (see figure 3.38). The monotonous decrease of sheet resistance is related to the doping concentration. The Ga and In substitutes the Zn^{2+} ions in the ZnO lattice. They are ionized and free electrons are formed that increase the charge carrier density. The higher the doping content, the higher the charge density and the lower the resistance. [198, 200–204, 206, 229, 230, 233, 237, 242, 249, 252–255]

An increase in resistivity for doping contents above the solubility limit (2 mol % to 6 mol % for GZO [44, 204, 233, 235, 248, 254] and 0.5 mol % to 6 mol % for IZO [200, 242]) as was found by other research groups could not be observed here. This effect is ascribed to the segregation of the dopants at grain boundaries or the formation of neutral defects. The first is a scatter center for the charge carriers and the second decreases the doping efficiency resulting in a lower number of charge carriers. Both effects increase the intensity.[198, 200, 206, 210, 251, 254] The absence of such an increase in the films investigated in this work confirms that the Ga and In is incorporated into the ZnO lattice and not segregated.

4 Conclusions

In this work, the deposition of functional ZnO films *via* a bioinspired approach was investigated. In the mineralization solution, crystallite growth was controlled by the organic additive PVP. To direct the formation of the thin films, silicon substrates were modified with organic molecules terminated by different functional groups. A polar functionalization was achieved with amino- (APTES) or carboxylate-terminated SAMs or a sulfonate-terminated PE multilayer. A non-polar surface was obtained by deposition of a fluorined SAM (FDTS). The non-modified pre-oxidized silicon substrate was used as a reference surface. The polar and non-polar character of the templates was confirmed by WCA measurements. It was observed that the polarity increases from FDTS (non-polar), APTES, the COOH-terminated SAM to the sulfonate-terminated PE with the highest polarity (see chapter 3.1.1).

Mineralization experiments showed that the non-modified, pre-oxidized SiO_x surface of the Si substrates is not suited for the deposition of homogeneous ZnO films. Surface-energy effects lead to Volmer-Weber growth of islands and 15 deposition cycles are necessary to produce a closed film (see figures 3.4a, 3.5a and 3.5b). For the substrates modified with the organic templates, a strong influence of the polarity of the functional groups on the ZnO deposition could be detected. The ZnO crystallites in solution exhibit an intrinsic dipole moment. The non-polar FDTS surface does not interact with these dipoles and consequently inhibits film growth completely (see figures 3.4d, 3.5g and 3.5h). Another behavior is observed for the polar

templates. The ZnO crystallites can interact with the surface charges of the surface functional groups. The higher the polarity is, the stronger is the interaction and the more homogeneous are the films (the polarity increases from APTES, the COOH-terminated SAM to the PE and consequently the homogeneity of the ZnO films increases as well). In addition, the high surface charge of the sulfonate-functionality of the PE multilayer leads to oriented attachment of the ZnO crystallites (figure 3.3). The resulting 002 texture can be verified by XRD measurements (figure 3.2). However, with increasing film thickness, the influence of the templates decreases and the deposition rate is independent of the template polarity (figure 3.6).

Further evidence of the importance of a polar surface for the deposition of ZnO thin films could be found by applying a PS brush as template. The non-polar polymer surface is expected to inhibit ZnO deposition similar as FDTS. However, IR measurements could confirm a transesterification of the PS molecules in the deposition solution (see chapter 3.2.1). The result is a polar functional surface group that can interact with the dipolar ZnO crystallites. This process supports the formation of homogeneous ZnO films (chapter 3.2.2).

Another parameter that is influenced by the polarity of the template is the granularity. This was investigated by deposition of a ZnO-containing material from aqueous solution on a structured APTES/FDTS template (chapter 3.3). Here, polar APTES islands are embedded in a matrix of non-polar FDTS. The nanoparticles in solution are attached to the polar APTES by entropic forces. Such a homogeneous adsorption leads to the formation of smooth ZnO areas. In contrast to this, the interaction with the non-polar FDTS is low. Nanoparticles can adsorb to small defect sites in the SAM layer only, while other particles are highly mobile. To reduce the surface energy, the nanoparticles agglomerate and finally, an area with high roughness is formed.

As was shown by the deposition experiments, the surface charge of the

sulfonate-terminated PE multilayer and the modified PS brush supports the formation of 002 textured ZnO films. The surface charge of the COOH-terminated SAM however is not high enough to promote oriented attachment. Such preferred orientation is a prerequisite for a macroscopic piezoelectric behavior of the ZnO film. Therefore, the piezoelectric performance of the films deposited onto these three templates was measured by PFM (see chapter 3.4). The results show that the non-textured film on the COOH-terminated SAM is not piezoactive and exhibits a low piezoelectric coefficient of $1.0\,\mathrm{pm\,V^{-1}}$ only. In contrast to this, the textured films are piezoactive with a value of d_{33} of $6.4\,\mathrm{pm\,V^{-1}}$. Thus, it is possible to direct the formation of piezoelectric ZnO films *via* a bioinspired process by choosing an appropriate template. Like this, the value of d_{33} can be varied to be as low as for non-piezoelectric materials to values equal or higher than those of ZnO films produced by conventional processes.

Functionalization of ZnO films can also be achieved by improving the electrical properties or by tuning the wavelength of emitted light. Doping with group III elements can influence both properties. Therefore, a bioinspired approach was developed to incorporate Al, Ga or In into the ZnO lattice and to tune the optical and electrical properties of the deposited films (chapter 3.5). By introducing an Al precursor salt in various concentrations into the deposition solution, several effects can be observed. With increasing doping content, the pH of the mineralization solution decreases (see figure 3.18). This was shown to be correlated with the precipitation of hydroxides. For the highest doping content in solution of 50 mol % Al, the pH is as low as 7.3, which is too low for the formation of ZnO. Consequently, film growth is inhibited (figures 3.24g and 3.24h). However, for contents lower than 50 mol % Al, ZnO was deposited successfully. Furthermore, it was found that with increasing doping content, the film thickness increases strongly (figure 3.26). This is a result of the introduction of water with the Al precursor salt, which is a nonahydrate. The water increases the hydrolyza-

tion rate and ZnO is precipitated faster. This effect is also responsible for the occurrence of a 002 texture of the films with 15 mol % to 30 mol % Al (figure 3.20). Incorporation of Al into the ZnO lattice could be confirmed by ICP-AES and PL measurements. The first showed that for 30 mol % Al in solution, there are 0.7 mol % Al in the deposited film. This low value can be explained by the high difference in ionic radii between the Al^{3+} and the Zn^{2+} ions. Substitution of Zn^{2+} with Al^{3+} leads to lattice distortions that limit the solubility of Al in ZnO. Nevertheless, PL measurements show that the doping leads to a shift in the UV band of ZnO. With increasing doping content, a blue-shift can be observed that is a result of the so-called Burstein-Moss effect (figure 3.28).

Doping with Ga and In was also successful (see chapter 3.5.3). The precipitation of hydroxides from the deposition solution leads to a decreasing film thickness with increasing doping content (figure 3.34). However, the formation of GZO and IZO could be confirmed by ICP-AES measurements. The difference in ionic radii of the Ga^{3+} and In^{3+} ion to Zn^{2+} is lower than for Al^{3+}. As a result, the amount of Ga or In incoroprated into the films is higher than for Al (figure 3.35). Again, a blue-shift of the UV band in the measured PL spectra is a result of the incorporation of the doping elements (figure3.36). Additionally, the resistivity of the films was measured by the van der Pauw method. Successful incorporation could be proven by a decrease in the resistivity values for the doped samples. In comparison to $(1.4 \pm 0.9) \times 10^5\,\Omega\,\mathrm{cm}$ for the undoped ZnO sample, the resistivity drops to $(2.8 \pm 7.0) \times 10^3\,\Omega\,\mathrm{cm}$ for ZnO with 3.2 mol % Ga content and to $(3.7 \pm 3.4) \times 10^3\,\Omega\,\mathrm{cm}$ for ZnO with 0.4 mol % In content (figure 3.38).

Bibliography

1 J. A. Christman, J. R. R. Woolcott, A. I. Kingon and R. J. Nemanich, *Appl. Phys. Lett.*, 1998, **73**, 3851–3853.

2 C. P. Li and B. H. Yang, *J. Electron. Mater.*, 2011, **40**, 253–258.

3 I. K. Bdikin, J. Gracio, R. Ayouchi, R. Schwarz and A. L. Kholkin, *Nanotechnology*, 2010, **21**, 235703.

4 K.-M. Zhang, Y.-P. Zhao, F.-Q. He and D.-Q. Liu, *Chin. J. Chem. Phys.*, 2007, **20**, 721.

5 J. W. Dunlop and P. Fratzl, *Annu. Rev. Mater. Res.*, 2010, **40**, 1–24.

6 S. Mann, in *Biomineralization: chemical and biochemical perspectives*, ed. S. Mann, VCH, Weinheim [u.a.], 1989, ch. Crystallochemical Strategies in Biomineralization, pp. 35–62.

7 C. F. Klingshirn, B. K. Meyer, A. Waag, A. Hoffmann and J. Geurts, *Zinc Oxide: From Fundamental Properties Towards Novel Applications*, Springer, Berlin, Heidelberg, 2010.

8 *Transparent Conductive Zinc Oxide*, ed. K. Ellmer, A. Klein and B. Rech, Springer-Verlag Berlin Heidelberg, 2008.

9 J. Baier, N. J. Blumenstein, J. Preusker, L. P. H. Jeurgens, U. Welzel, T. A. Do, J. Pleiss and J. Bill, *CrystEngComm*, 2014, **16**, 5301–5307.

10 J. Baier, T. Naumburg, N. J. Blumenstein, L. P. H. Jeurgens, U. Welzel, T. A. Do, J. Pleiss and J. Bill, *Biointerface research in applied chemistry*, 2012, **2**, 380–391.

11 J. Baier, R. Strumberger, F. Berger, P. Atanasova, U. Welzel and J. Bill, *Biointerface Research in Applied Chemistry*, 2012, **2**, 399–349.

12 M. Jitianu and D. V. Goia, *J. Colloid Interface Sci.*, 2007, **309**, 78–85.

13 P. Ma, Y. Wu, Z. Fu and W. Wang, *Adv. Powder Technol.*, 2012, **23**, 170 – 174.

14 T. Togashi, N. Yokoo, M. Umetsu, S. Ohara, T. Naka, S. Takami, H. Abe, I. Kumagai and T. Adschiri, *J. Biosci. Bioeng.*, 2011, **111**, 140 – 145.

15 M. M. Tomczak, M. K. Gupta, L. F. Drummy, S. M. Rozenzhak and R. R. Naik, *Acta Biomater.*, 2009, **5**, 876–882.

16 P. Atanasova, D. Rothenstein, J. J. Schneider, R. C. Hoffmann, S. Dilfer, S. Eiben, C. Wege, H. Jeske and J. Bill, *Adv. Mater.*, 2011, **23**, 4918–4922.

17 R. C. Hoffmann, P. Atanasova, S. Dilfer, J. Bill and J. J. Schneider, *phys. status solidi (a)*, 2011, **208**, 1983–1988.

18 P. Lipowsky, Z. Burghard, L. P. H. Jeurgens, J. Bill and F. Aldinger, *Nanotechnology*, 2007, **18**, 345707.

19 D. R. Clarke, *J. Am. Ceram. Soc.*, 1999, **82**, 485–502.

20 S. C. Pillai, J. M. Kelly, R. Ramesh and D. E. McCormack, *J. Mater. Chem. C*, 2013, **1**, 3268–3281.

21 A. Wei, L. Pan and W. Huang, *J. Mater. Sci. Eng. B*, 2011, **176**, 1409 – 1421.

22 E. Hosono, S. Fujihara, I. Honma and H. Zhou, *Adv. Mater.*, 2005, **17**, 2091–2094.

23 H. Rensmo, K. Keis, H. Lindstroem, S. Soedergren, A. Solbrand, A. Hagfeldt, S.-E. Lindquist, L. N. Wang and M. Muhammed, *J. Phys. Chem. B*, 1997, **101**, 2598–2601.

24 H. Wang, H. Long, Z. Chen, X. Mo, S. Li, Z. Zhong and G. Fang, *Electronic Materials Letters*, 2015, **11**, 664–669.

25 Q. Yang, Y. Liu, C. Pan, J. Chen, X. Wen and Z. L. Wang, *Nano Lett.*, 2013, **13**, 607–613.

26 P. Atanasova, N. Stitz, S. Sanctis, J. H. M. Maurer, R. C. Hoffmann, S. Eiben, H. Jeske, J. J. Schneider and J. Bill, *Langmuir*, 2015, **31**, 3897–3903.

27 H. Qian, Y. Wang, Y. Fang, L. Gu, R. Lu and J. Sha, *J. Appl. Phys.*, 2015, **117**, 164308.

28 K. Momma and F. Izumi, *J. Appl. Crystallogr.*, 2011, **44**, 1272–1276.

29 D. C. Reynolds, D. C. Look, B. Joga, J. E. Van Nostrand, R. Jones and J. Jenny, *Solid State Commun.*, 1998, **106**, 701 – 704.

30 S. A. Studenikin, N. Golego and M. Cocivera, *J. Appl. Phys.*, 1998, **84**, 2287–2294.

31 R. Dingle, *Phys. Rev. Lett.*, 1969, **23**, 579–581.

32 A. Catellani, A. Ruini, G. Cicero and A. Calzolari, *phys. status solidi (b)*, 2013, **250**, 2106–2109.

33 C. G. V. de Walle, *Physica B: Condensed Matter*, 2001, **308-310**, 899 – 903.

34 J. E. Stehr, W. M. Chen, N. K. Reddy, C. W. Tu and I. A. Buyanova, *Scientific Reports*, 2015, **5**, 13406.

35 C. Ton-That, L. Zhu, M. N. Lockrey, M. R. Phillips, B. C. C. Cowie, A. Tadich, L. Thomsen, S. Khachadorian, S. Schlichting, N. Jankowski and A. Hoffmann, *Phys. Rev. B*, 2015, **92**, 024103.

36 T. Jeong, J. Yu, H. Mo, T. Kim, K. Lim, C. Youn, K. Hong and H. Kim, *J. Electron. Mater.*, 2014, **43**, 2688–2693.

37 C. Park, S. Kim and S. Lim, *Solid State Communications*, 2013, **167**, 18 – 22.

38 Y. Sui, B. Yao, L. Xiao, G. Xing, L. Yang, X. Li, X. Li, J. Lang, S. Lv, J. Cao, M. Gao and J. Yang, *J. Appl. Phys.*, 2013, **113**, –.

39 H. Liang, Y. Chen, X. Xia, Q. Feng, Y. Liu, R. Shen, Y. Luo and G. Du, *Thin Solid Films*, 2015, **589**, 199 – 202.

40 M. Gabás, A. Landa-Cánovas, J. Luis Costa-Krämer, F. Agulló-Rueda, A. R. González-Elipe, P. Díaz-Carrasco, J. Hernández-Moro, I. Lorite, P. Herrero, P. Castillero, A. Barranco and J. Ramón Ramos-Barrado, *J. Appl. Phys.*, 2013, **113**, –.

41 J. A. Sans, J. F. Sánchez-Royo, A. Segura, G. Tobias and E. Canadell, *Phys. Rev. B*, 2009, **79**, 195105.

42 K. Yoshino, T. Hata, T. Kakeno, H. Komaki, M. Yoneta, Y. Akaki and T. Ikari, *physica status solidi (c)*, 2003, **0**, 626–630.

43 A. P. Roth, J. B. Webb and D. F. Williams, *Phys. Rev. B*, 1982, **25**, 7836–7839.

44 A. R. Babar, P. R. Deshamukh, R. J. Deokate, D. Haranath, C. H. Bhosale and K. Y. Rajpureai, *J. Phys. D: Appl. Phys.*, 2008, **41**, 135404.

45 Y. W. Chen, Y. C. Liu, S. X. Lu, C. S. Xu and C. L. Shao, *Applied Physics B*, 2006, **84**, 507–510.

46 T. Makino, Y. Segawa, S. Yoshida, A. Tsukazaki, A. Ohtomo and M. Kawasaki, *Appl. Phys. Lett.*, 2004, **85**, 759–761.

47 S. Suwanboon, *Science Asia*, 2008, **34**, 31–34.

48 X. B. Wang, C. Song, K. W. Geng, F. Zeng and F. Pan, *J. Phys. D: Appl. Phys.*, 2006, **39**, 4992.

49 A. L. Kholkin, S. V. Kalinin, A. Roelofs and A. Gruverman, in *Review of Ferroelectric Domain Imaging by Piezoresponse Force Microscopy*, ed. S. Kalinin and A. Gruverman, Springer New York, 2007, vol. 1, ch. 1.6, pp. 173–214.

50 I. Kornev, M. Willatzen, B. Lassen and L. C. Lew Yan Voon, *AIP Conference Proceedings*, 2010, **1199**, 71–72.

51 D. A. Scrymgeour, T. L. Sounart, N. C. Simmons and J. W. P. Hsu, *J. Appl. Phys.*, 2007, **101**, 014316.

52 M.-H. Zhao, Z.-L. Wang and S. X. Mao, *Nano Lett.*, 2004, **4**, 587–590.

53 K. Momeni, A. Asthana, A. Prasad, Y. K. Yap and R. Shahbazian-Yassar, *Appl. Phys. A*, 2012, **109**, 95–100.

54 *Biomimetic and Bioinspired Nanomaterials*, ed. C. S. S. R. Kumar, Wiley VCH, Weinheim, 2010, vol. 7.

55 H. Coelfen, in *Biomineralization II*, ed. K. Naka, Springer Berlin Heidelberg, 2007, vol. 271, pp. 1–77.

56 S. Mann, *Biomineralization: principles and concepts in bioinorganic materials chemistry*, Oxford University Press, Oxford [u.a.], 1st edn., 2001.

57 W. Ostwald, *Z. Phys. Chem.*, 1897, **22**, 289–330.

58 S. K. Das, M. M. R. Khan, A. K. Guha and N. Naskar, *Green Chem.*, 2013, **15**, 2548–2557.

59 J. M. Delgado-Lopez, R. Frison, A. Cervellino, J. Gomez-Morales, A. Guagliardi and N. Masciocchi, *Adv. Funct. Mater.*, 2014, **24**, 1090–1099.

60 C. C. Hire, A. J. Oyer, G. E. Macek, J. L. Bento and D. H. Adamson, *J. Mater. Chem. B*, 2013, **1**, 1977–1984.

61 W. Jo, K. J. Freedman and M. J. Kim, *Materials Science and Engineering: C*, 2012, **32**, 2426 – 2430.

62 G. Lasko, Z. Burghard, J. Bill, I. Schäfer, U. Weber and S. Schmauder, *Advanced Engineering Materials*, 2013, **15**, 908–920.

63 Y. Yan, B. Hao, X. Wang and G. Chen, *Dalton Trans.*, 2013, **42**, 12179–12184.

64 P. Gerstel, P. Lipowsky, O. Durupthy, R. C. Hoffmann, P. Bellina, J. Bill and F. Aldinger, *J. Ceram. Soc. Jpn.*, 2006, **114**, 911–917.

65 P. Gerstel, R. C. Hoffmann, P. Lipowsky, L. P. H. Jeurgens, J. Bill and F. Aldinger, *Chem. Mater.*, 2006, **18**, 179–186.

66 K. Govender, D. S. Boyle, P. B. Kenway and P. O'Brien, *J. Mater. Chem.*, 2004, **14**, 2575–2591.

67 R. C. Hoffmann, S. Jia, L. P. Jeurgens, J. Bill and F. Aldinger, *J. Mater. Sci. Eng. C*, 2006, **26**, 41 – 45.

68 P. Lipowsky, N. Hedin, J. Bill, R. C. Hoffmann, A. Ahniyaz, F. Aldinger and L. Bergstrom, *J. Phys. Chem. C*, 2008, **112**, 5373–5383.

69 P. Lipowsky, S. Jia, R. C. Hoffmann, N. Y. Jin-Phillipp, J. Bill and M. Ruhle, *Int. J. Mater. Res.*, 2006, **97**, 607–613.

70 R. A. Reichle, K. G. McCurdy and L. G. Hepler, *Can. J. Chem.*, 1975, **53**, 3841–3845.

71 P. Lipowsky, R. C. Hoffmann, U. Welzel, J. Bill and F. Aldinger, *Adv. Funct. Mater.*, 2007, **17**, 2151–2159.

72 P. Lipowsky, *Ph.D. thesis*, University of Stuttgart, 2007.

73 J. Bill, R. C. Hoffmann, T. M. Fuchs and F. Aldinger, *Zeitschrift fur Metallkunde*, 2002, **93**, 478–489.

74 J.-J. Shyue, M. R. De Guire, T. Nakanishi, Y. Masuda, K. Koumoto and C. N. Sukenik, *Langmuir*, 2004, **20**, 8693–8698.

75 R. G. Nuzzo and D. L. Allara, *J. Am. Chem. Soc.*, 1983, **105**, 4481–4483.

76 L. Netzer and J. Sagiv, *J. Am. Chem. Soc.*, 1983, **105**, 674–676.

77 J. Sagiv, *J. Am. Chem. Soc.*, 1980, **102**, 92–98.

78 M. J. Stevens, *Langmuir*, 1999, **15**, 2773–2778.

79 F. Schreiber, *Prog. Surf. Sci.*, 2000, **65**, 151 – 257.

80 D. K. Schwartz, *Annu. Rev. Phys. Chem.*, 2001, **52**, 107–137.

81 L. P. Bauermann, P. Gerstel, J. Bill, S. Walheim, C. Huang, J. Pfeifer and T. Schimmel, *Langmuir*, 2010, **26**, 3774–3778.

82 M. E. Coltrin, J. W. P. Hsu, D. A. Scrymgeour, J. R. Creighton, N. C. Simmons and C. M. Matzke, *J. Cryst. Growth*, 2008, **310**, 584 – 593.

83 J. W. P. Hsu, W. M. Clift and L. N. Brewer, *Langmuir*, 2008, **24**, 5375–5381.

84 P. Lipowsky, M. Hirscher, R. C. Hoffmann, J. Bill and F. Aldinger, *Nanotechnology*, 2007, **18**, 1 – 5.

85 Z. Shi and A. V. Walker, *Langmuir*, 2015, **31**, 1421–1428.

86 P. Yang, S. Zou and W. Yang, *Small*, 2008, **4**, 1527–1536.

87 Y. Masuda, N. Kinoshita, F. Sato and K. Koumoto, *Cryst. Growth Des.*, 2006, **6**, 75–78.

88 H. Shao, X. Qian and B. Huang, *Mater. Sci. Semicond. Process.*, 2007, **10**, 68 – 76.

89 J. J. Schwartz, J. N. Hohman, E. I. Morin and P. S. Weiss, *ACS Applied Materials & Interfaces*, 2013, **5**, 10310–10316.

90 C.-C. Wu, D. N. Reinhoudt, C. Otto, A. H. Velders and V. Subramaniam, *ACS Nano*, 2010, **4**, 1083–1091.

91 N. J. Blumenstein, J. Berson, S. Walheim, P. Atanasova, J. Baier, J. Bill and T. Schimmel, *Beilstein J. Nanotechnol.*, 2015, **6**, 1763–1768.

92 C. Huang, A. Förste, S. Walheim and T. Schimmel, *Beilstein J. Nanotechnol.*, 2015, **6**, 1205–1211.

93 C. Huang, M. Moosmann, J. Jin, T. Heiler, S. Walheim and T. Schimmel, *Beilstein J. Nanotechnol.*, 2012, **3**, 620–628.

94 S. Walheim, T. Schimmel and R. Gröger, *Stempel für das Mikrokontaktdrucken und Verfahren zu seiner Herstellung*, EU Pat., EP 2 150 854 B1, 2012.

95 S. Zou, H. Bai, P. Yang and W. Yang, *Macromol. Chem. Phys.*, 2009, **210**, 1519–1527.

96 S. Minko, in *Polymer Surfaces and Interfaces*, ed. M. Stamm, Springer Berlin Heidelberg, 2008, pp. 215–234.

97 Y. Huang, Z. Zhan, X. Zhang, H. Li and C. Huang, *J. Nanopart. Res.*, 2015, **17**, year.

98 J. Prehn, F. C. and S. G. Boyes, *Macromolecules*, 2015, **48**, 4269–4280.

99 S. Burkert, M. Kuntzsch, C. Bellmann, P. Uhlmann and M. Stamm, *Appl. Surf. Sci.*, 2009, **255**, 6256 – 6261.

100 G. Emilsson, R. L. Schoch, L. Feuz, F. Höök, R. Y. H. Lim and A. B. Dahlin, *ACS Appl. Mater. Interfaces*, 2015, **7**, 7505–7515.

101 J. H. Maas, M. A. C. Stuart, A. B. Sieval, H. Zuilhof and E. J. R. Sudhölter, *Thin Solid Films*, 2003, **426**, 135 – 139.

102 G. Decher, *Science*, 1997, **277**, 1232–1237.

103 N. G. Hoogeveen, M. A. C. Stuart, G. J. Fleer and M. R. Böhmer, *Langmuir*, 1996, **12**, 3675–3681.

104 D. G. Kurth, D. Volkmer and R. v. Klitzing, in *Multilayer Thin Films: Sequential Assembly of Nanocomposite Materials*, ed. G. Decher and J. B. Schlenoff, Wiley-VCH, 2002, ch. Multilayers on Solid Planar Substrates: From Structure to Function, pp. 393–426.

105 J. Dejeu, L. Buisson, M. C. Guth, C. Roidor, F. Membrey, D. Charraut and A. Foissy, *Colloids Surf., A*, 2006, **288**, 26 – 35.

106 T. Young, *Phil. Trans. R. Soc. Lond.*, 1805, **95**, 65–87.

107 D. C. Grahame, *Chem. Rev.*, 1947, **41**, 441–501.

108 R. H. Müller, W. Mehnert and G. E. Hildebrand, *Zetapotential und Partikelladung in der Laborpraxis: Einführung in die Theorie, praktische Meßdurchführung, Dateninterpretation*, Wiss. Verl.-Ges., Stuttgart, 1996.

109 B. J. Kirby and E. F. Hasselbrink, *Electrophoresis*, 2004, **25**, 187–202.

110 C. Werner, H. Koerber, R. Zimmermann, S. Dukhin and H.-J. Jacobasch, *J. Colloid Interface Sci.*, 1998, **208**, 329 – 346.

111 H. J. Jacobasch, G. Bauböck and J. Schurz, *Colloid Polym. Sci.*, 1985, **263**, 3–24.

112 K. Grundke, in *Polymer Surfaces and Interfaces*, ed. M. Stamm, Springer Berlin Heidelberg, 2008, pp. 103–138.

113 M. Hesse, H. Meier and B. Zeeh, in *Spektroskopische Methoden in der organischen Chemie*, Georg Thieme Verlag, 8th edn., 2005, ch. Infrarot- und Raman-Spektren, pp. 33–72.

114 J. Fahrenfort, *Spectrochimica Acta*, 1961, **17**, 698 – 709.

115 N. J. Harrick, *J. Phys. Chem.*, 1960, **64**, 1110–1114.

116 V. P. Tolstoy, I. V. Chernyshova and V. A. Skryshevsky, in *Optimum Conditions for Recording Infrared Spectra of Ultrathin Films*, John Wiley & Sons, Inc., 2003, pp. 307–415.

117 G. Binnig, C. F. Quate and C. Gerber, *Phys. Rev. Lett.*, 1986, **56**, 930–933.

118 A. Foster and W. Hofer, in *The Physics of Scanning Probe Microscopes*, Springer New York, New York, NY, 2006, pp. 1–10.

119 G. Kaupp, in *Atomic Force Microscopy*, Springer Berlin Heidelberg, Berlin, Heidelberg, 2006, pp. 1–86.

120 D. Ricci and P. C. Braga, in *Atomic Force Microscopy: Biomedical Methods and Applications*, ed. P. C. Braga and D. Ricci, Humana Press, Totowa, NJ, 2004, ch. Imaging Methods in Atomic Force Microscopy, pp. 13–23.

121 F. J. Giessibl, *Rev. Mod. Phys.*, 2003, **75**, 949–983.

122 Q. Zhong, D. Inniss, K. Kjoller and V. B. Elings, *Surface Science Letters*, 1993, **290**, L688 – L692.

123 S. V. Kalinin and A. Gruverman, *Scanning Probe Microscopy - Electrical and Electromechanical Phenomena at the Nanoscale*, Springer-Verlag New York, 2007.

124 S. V. Kalinin, B. J. Rodriguez, S. Jesse, J. Shin, A. P. Baddorf, P. Gupta, H. Jain, D. B. Williams and A. Gruverman, *Microsc. Microanal.*, 2006, **12**, 206–220.

125 A. Gruverman and S. V. Kalinin, *J. Mater. Sci.*, 2006, **41**, 107–116.

126 S. V. Kalinin, A. Rar and S. Jesse, *IEEE Trans. Sonics Ultrason.*, 2006, **53**, 2226–2252.

127 E. Soergel, *J. Phys. D: Appl. Phys.*, 2011, **44**, 464003.

128 S. V. Kalinin and D. A. Bonnell, *Phys. Rev. B*, 2002, **65**, 125408.

129 D. A. Scrymgeour and J. W. P. Hsu, *Appl. Phys. Lett.*, 2008, **93**, 233114.

130 T. Jungk, A. Hoffmann and E. Soergel, *Appl. Phys. Lett.*, 2006, **89**, 163507.

131 T. Jungk, A. Hoffmann and E. Soergel, *Appl. Phys. Lett.*, 2007, **91**, year.

132 M. von Ardenne, *Zeitschrift für Physik*, 1938, **109**, 553–572.

133 L. Reimer, *Scanning Electron Microscopy - Physics of Image Formation and Microanalysis*, Springer Berlin Heidelberg, 1998.

134 W. H. Bragg and W. L. Bragg, *Proc. R. Soc. London, Ser. A*, 1913, **88**, 428–438.

135 V. K. Pecharsky and P. Y. Zavali, in *Fundamentals of Powder Diffraction and Structural Characterization of Materials*, Springer US, Boston, MA, 2003, ch. Experimental Techniques, pp. 261–338.

136 C. S. Barrett and T. B. Massalski, *Structure of Metals*, McGraw-Hill Book Company, 3rd edn., 1966.

137 P. Scherrer, *Nachrichten von der Gesellschaft der Wissenschaften zu Göttingen*, 1918, 98–100.

138 D. Balzar, N. Audebrand, M. R. Daymond, A. Fitch, A. Hewat, J. I. Langford, A. Le Bail, D. Louër, O. Masson, C. N. McCowan, N. C. Popa, P. W. Stephens and B. H. Toby, *J. Appl. Crystallogr.*, 2004, **37**, 911–924.

139 P. Scardi, M. Leoni and R. Delhez, *J. Appl. Crystallogr.*, 2004, **37**, 381–390.

140 A. Einstein, *Ann. d. Phys.*, 1905, **322**, 132–148.

141 *Practical Surface Analysis*, ed. D. Briggs and M. P. Seah, Wiley, New York, 2nd edn., 1990, vol. 1, pp. XIV, 657 S.

142 D. Pleul and F. Simon, in *Polymer Surfaces and Interfaces - Characterization, Modification and Applications*, ed. M. Stamm, Springer-Verlag Berlin Heidelberg, 2008, ch. X-Ray Photoelectron Spectroscopy, pp. 71–90.

143 C. D. Harris, in *Lehrbuch der quantitativen Analyse*, ed. G. Werner and T. Werner, Springer Berlin Heidelberg, Berlin, Heidelberg, 2014, ch. Atomspektroskopie, pp. 541–567.

144 C. D. Harris, in *Lehrbuch der quantitativen Analyse*, ed. G. Werner and T. Werner, Springer Berlin Heidelberg, Berlin, Heidelberg, 2014, ch. Grundlagen der Spektralphotometrie, pp. 443–471.

145 D. Schroder, in *Semiconductor Material and Device Characterization*, Wiley-IEEE Press, 3rd edn., 2006, ch. Optical Characterization, pp. 563–626.

146 L. Brus, *J. Phys. Chem.*, 1986, **90**, 2555–2560.

147 L. Irimpan, V. P. N. Nampoori, P. Radhakrishnan, A. Deepthy and B. Krishnan, *J. Appl. Phys.*, 2007, **102**, year.

148 L. J. van der Pauw, *Philips Res. Repts.*, 1958, **13**, 1–9.

149 G. Kissinger and W. Kissinger, *physica status solidi (a)*, 1991, **123**, 185–192.

150 A. Plößl and G. Kräuter, *Materials Science and Engineering: R: Reports*, 1999, **25**, 1 – 88.

151 R. Sherman, *Part. Sci. Technol.*, 2007, **25**, 37–57.

152 R. Sherman, D. Hirt and R. Vane, *Journal of Vacuum Science & Technology A*, 1994, **12**, 1876–1881.

153 Y. Han, A. Offenhaeusser and S. Ingebrandt, *Surf. Interface Anal.*, 2006, **38**, 176–181.

154 D. Janssen, R. D. Palma, S. Verlaak, P. Heremans and W. Dehaen, *Thin Solid Films*, 2006, **515**, 1433 – 1438.

155 C. G. Hofmeister, *Diplomarbeit*, University of Stuttgart, 2012.

156 F. Streb, *M.Sc. thesis*, University of Stuttgart, 2014.

157 N. J. Blumenstein, C. G. Hofmeister, P. Lindemann, C. Huang, J. Baier, A. Leineweber, S. Walheim, C. Woell, T. Schimmel and J. Bill, *Beilstein J. Nanotechnol.*, 2016, **7**, 102–110.

158 N. Stitz, S. Eiben, P. Atanasova, N. Domingo, A. Leineweber, Z. Burghard and J. Bill, *Scientific Reports*, 2016, **6**, 26518–.

159 R. Eisele, *diploma thesis*, University of Stuttgart, 2013.

160 R. Eisele, N. J. Blumenstein, J. Baier, S. Walheim, T. Schimmel and J. Bill, *CrystEngComm*, 2014, **16**, 1560–1567.

161 F. Fairbrother and H. Mastin, *J. Chem. Soc., Trans.*, 1924, **125**, 2319–2330.

162 I. Zawisza, G. Wittstock, R. Boukherroub and S. Szunerits, *Langmuir*, 2007, **23**, 9303–9309.

163 A. A. Coelho, *TOPAS : General Profile. Structure Analysis Software for Powder Diffraction Data. V2. 0*, Bruker AXS GmbH, Karlsruhe, Germany, 2003.

164 C. W. Extrand, *Langmuir*, 2003, **19**, 3793–3796.

165 S. Fiorilli, P. Rivolo, E. Descrovi, C. Ricciardi, L. Pasquardini, L. Lunelli, L. Vanzetti, C. Pederzolli, B. Onida and E. Garrone, *J. Colloid Interface Sci.*, 2008, **321**, 235 – 241.

166 L. Jiang, S. Li, J. Wang, L. Yang, Q. Sun and Z. Li, *Journal of Nanomaterials*, 2014, **2014**, year.

167 L. Liu, S. Song and P. Zhang, *Surf. Interface Anal.*, 2013, **45**, 993–997.

168 E. A. Smith and W. Chen, *Langmuir*, 2008, **24**, 12405–12409.

169 G. K. Toworfe, R. J. Composto, I. M. Shapiro and P. Ducheyne, *Biomaterials*, 2006, **27**, 631 – 642.

170 O. Gershevitz, and C. N. Sukenik, *J. Am. Chem. Soc.*, 2004, **126**, 482–483.

171 W.-C. Lin, S.-H. Lee, M. Karakachian, B.-Y. Yu, Y.-Y. Chen, Y.-C. Lin, C.-H. Kuo and J.-J. Shyue, *Phys. Chem. Chem. Phys.*, 2009, **11**, 6199–6204.

172 D. K. Owens and R. C. Wendt, *J. Appl. Polym. Sci.*, 1969, **13**, 1741–1747.

173 M. J. Pellerite, E. J. Wood and V. W. Jones, *J. Phys. Chem. B*, 2002, **106**, 4746–4754.

174 U. Srinivasan, M. R. Houston, R. T. Rowe and R. Maboudian, TRANSDUCERS '97 - International Conference onSolid State Sensors and Actuators, Chicago, 1997, pp. 1399–1402.

175 A. Greß, *bachelors thesis*, University of Stuttgart, 2014.

176 K. Ellmer, *J. Phys. D: Appl. Phys.*, 2001, **34**, 3097.

177 G. Akerlof, *J. Am. Chem. Soc.*, 1932, **54**, 4125–4139.

178 M. Kosmulski and E. Matijevic, *Langmuir*, 1992, **8**, 1060–1064.

179 G. Wegner, P. Baum, M. Mueller, J. Norwig and K. Landfester, *Macromol. Symp.*, 2001, **175**, 349–356.

180 M. Kosmulski, J. Hartikainen, E. Maczka, W. Janusz and J. B. Rosenholm, *Anal. Chem.*, 2002, **74**, 253–256.

181 P. J. Majewski and T. M. Fuchs, *Adv. Powder Technol.*, 2007, **18**, 303 – 310.

182 S.-W. Kim, S. Fujita and S. Fujita, *Jpn. J. Appl. Phys.*, 2002, **41**, L543.

183 J. A. Venables, G. D. T. Spiller and M. Hanbucken, *Rep. Prog. Phys.*, 1984, **47**, 399.

184 G. Socrates, *Infrared and Raman Characteristic Group Frequencies – Tables and Charts*, John Wiley and Sons LTD, Chichester, 3rd edn., 2001.

185 C. Y. Liang and S. Krimm, *J. Pol. Sci.*, 1958, **17**, 241–254.

186 R. Turgeman, O. Gershevitz, M. Deutsch, B. M. Ocko, A. Gedanken and C. N. Sukenik, *Chem. Mater.*, 2005, **17**, 5048–5056.

187 R. Turgeman, O. Gershevitz, O. Palchik, M. Deutsch, B. M. Ocko, A. Gedanken and C. N. Sukenik, *Cryst. Growth Des.*, 2004, **4**, 169–175.

188 C.-H. Kuo, H.-Y. Chang, C.-P. Liu, S.-H. Lee, Y.-W. You and J.-J. Shyue, *Phys. Chem. Chem. Phys.*, 2011, **13**, 3649–3653.

189 H. Gliemann, Y. Mei, M. Ballauff and T. Schimmel, *Langmuir*, 2006, **22**, 7254–7259.

190 U. Oezguer, Y. I. Alivov, C. Liu, A. Teke, M. A. Reshchikov, S. Dogan, V. Avrutin, S.-J. Cho and H. Morkoc, *J. Appl. Phys.*, 2005, **98**, –.

191 C. Baes and R. Mesmer, *The Hydrolysis of Cations*, Krieger Publ., 1986.

192 R. M. Smith, *Critical Stability Constants - Inorganic Complexes*, Springer US, 1976, vol. 4.

193 W. Stumm and J. J. Morgan, *Aquatic Chemistry: Chemical Equilibria and Rates in Natural Waters*, Wiley, 3rd edn., 1996.

194 H. Wang, C. Xie and D. Zeng, *J. Cryst. Growth*, 2005, **277**, 372 – 377.

195 H. Wang, C. Xie, D. Zeng and Z. Yang, *J. Colloid Interface Sci.*, 2006, **297**, 570 – 577.

196 A. Becheri, M. Dürr, P. Lo Nostro and P. Baglioni, *Journal of Nanoparticle Research*, 2008, **10**, 679–689.

197 R. D. Shannon, *Acta Crystallographica Section A*, 1976, **32**, 751–767.

198 S. Chen, G. Carraro, D. Barreca and R. Binions, *Thin Solid Films*, 2015, **584**, 316 – 319.

199 D. J. Goyal, C. Agashe, M. G. Takwale, V. G. Bhide, S. Mahamuni and S. K. Kulkarni, *J. Mater. Res.*, 1993, **8**, 1052–1056.

200 A. Hafdallah, F. Yanineb, M. S. Aida and N. Attaf, *J. Alloys Compd.*, 2011, **509**, 7267 – 7270.

201 H. Mahdhi, Z. B. Ayadi, J. L. Gauffier and K. Djessas, *J. Electron. Mater.*, 2016, **45**, 557–565.

202 Z.-N. Ng, K.-Y. Chan, C.-Y. Low, S. A. Kamaruddin and M. Z. Sahdan, *Ceram. Int.*, 2015, **41, Supplement 1**, S254 – S258.

203 S. Pati, P. Banerji and S. B. Majumder, *RSC Adv.*, 2015, **5**, 61230–61238.

204 C.-Y. Tsay, C.-W. Wu, C.-M. Lei, F.-S. Chen and C.-K. Lin, *Thin Solid Films*, 2010, **519**, 1516 – 1520.

205 S. Chen, G. Carraro, D. Barreca, A. Sapelkin, W. Chen, X. Huang, Q. Cheng, F. Zhang and R. Binions, *J. Mater. Chem. A*, 2015, **3**, 13039–13049.

206 V. R. Shinde, C. D. Lokhande, R. S. Mane and S.-H. Han, *Applied Surface Science*, 2005, **245**, 407 – 413.

207 D. Ramírez, K. Álvarez, G. Riveros, M. Tejos and M. G. Lobos, *J. Solid State Electrochem.*, 2014, **18**, 2869–2884.

208 H. Serier, M. Gaudon and M. Menetrier, *Solid State Sci.*, 2009, **11**, 1192 – 1197.

209 K. Shirouzu, T. Ohkusa, M. Hotta, N. Enomoto and J. Hojo, *J. Ceram. Soc. Jpn.*, 2007, **115**, 254–258.

210 I. Valenti, S. Benedetti, A. di Bona, V. Lollobrigida, A. Perucchi, P. Di Pietro, S. Lupi, S. Valeri and P. Torelli, *J. Appl. Phys.*, 2015, **118**, year.

211 J. T. Chen, J. Wang, R. F. Zhuo, D. Yan, J. J. Feng, F. Zhang and P. X. Yan, *Appl. Surf. Sci.*, 2009, **255**, 3959 – 3964.

212 J. Rashid, M. A. Barakat, N. Salah and S. S. Habib, *RSC Adv.*, 2014, **4**, 56892–56899.

213 M. Chen, Z. L. Pei, C. Sun, L. S. Wen and X. Wang, *J. Cryst. Growth*, 2000, **220**, 254 – 262.

214 M. Chen, X. Wang, Y. H. Yu, Z. L. Pei, X. D. Bai, C. Sun, R. F. Huang and L. S. Wen, *Appl. Surf. Sci.*, 2000, **158**, 134 – 140.

215 L. Li, L. Fang, X. J. Zhou, Z. Y. Liu, L. Zhao and S. Jiang, *J. Electron Spectrosc. Relat. Phenom.*, 2009, **173**, 7 – 11.

216 S. Yun, J. Lee, J. Yang and S. Lim, *Physica B: Condensed Matter*, 2010, **405**, 413 – 419.

217 L. G. Mar, P. Y. Timbrell and R. N. Lamb, *Thin Solid Films*, 1993, **223**, 341 – 347.

218 J. F. Chang and M. H. Hon, *Thin Solid Films*, 2001, **386**, 79 – 86.

219 C.-H. Hsu and D.-H. Chen, *Nanotechnology*, 2010, **21**, 285603.

220 V. I. Nefedov, *J. Electron Spectrosc. Relat. Phenom.*, 1982, **25**, 29 – 47.

221 K. H. Yoon, J.-W. Choi and D.-H. Lee, *Thin Solid Films*, 1997, **302**, 116 – 121.

222 S.-S. Lin, J.-L. Huang and P. Šajgalik, *Surf. Coat. Technol.*, 2005, **190**, 39 – 47.

223 B. Paul, B. Singh, S. Ghosh and A. Roy, *Thin Solid Films*, 2016, **603**, 21 – 28.

224 L. Gong, Z. Ye, J. Lu, L. Zhu, J. Huang, X. Gu and B. Zhao, *Vacuum*, 2010, **84**, 947 – 952.

225 Y.-S. Kim and W.-P.Tai, *Appl. Surf. Sci.*, 2007, **253**, 4911 – 4916.

226 B. R. Strohmeier, *Surface Science Spectra*, 1994, **3**, 128–134.

227 H. Algarni, M. M. El-Gomati and M. S. Al-Assiri, *J. Nanosci. Nanotechnol.*, 2014, **14**, 5317–5323.

228 S. Y. Bae, C. W. Na, J. H. Kang and J. Park, *J. Phys. Chem. B*, 2005, **109**, 2526–2531.

229 K. Chen, F. Hung, S. Chang and Z. Hu, *Applied Surface Science*, 2009, **255**, 6308 – 6312.

230 P. M. R. Kumar, C. S. Kartha and K. P. Vijayakumar, *J. Appl. Phys.*, 2005, **98**, year.

231 J. Shim, H. Kim, H. Chang and S.-O. Kim, *J. Mater. Sci.: Mater. Electron.*, 2011, **22**, 1350–1356.

232 P. Nunes, E. Fortunato, P. Tonello, F. B. Fernandes, P. Vilarinho and R. Martins, *Vacuum*, 2002, **64**, 281 – 285.

233 G. K. Paul and S. K. Sen, *Mater. Lett.*, 2002, **57**, 742 – 746.

234 G. Pineda-Hernández, A. Escobedo-Morales, U. Pal and E. Chigo-Anota, *Materials Chemistry and Physics*, 2012, **135**, 810 – 817.

235 S. S. Shinde, P. S. Shinde, Y. W. Oh, D. Haranath, C. H. Bhosale and K. Y. Rajpure, *Appl. Surf. Sci.*, 2012, **258**, 9969 – 9976.

236 D. A. Schwartz, N. S. Norberg, Q. P. Nguyen, J. M. Parker and D. R. Gamelin, *J. Am. Chem. Soc.*, 2003, **125**, 13205–13218.

237 B. Khalfallah, F. Chaabouni and M. Abaab, *J. Mater. Sci.: Mater. Electron.*, 2015, **26**, 5209–5216.

238 R. Chen, P. Zhu, L. Deng, T. Zhao, R. Sun and C. Wong, *ChemPlusChem*, 2014, **79**, 743–750.

239 N. R. Yogamalar and A. C. Bose, *J. Alloys Compd.*, 2011, **509**, 8493 – 8500.

240 E. Riedel and C. Janiak, *Anorganische Chemie*, De Gruyter, Berlin, Boston, 2015, pp. –.

241 B. Singh and S. Ghosh, *J. Electron. Mater.*, 2015, **44**, 2663–2669.

242 P. Jood, R. J. Mehta, Y. Zhang, T. Borca-Tasciuc, S. X. Dou, D. J. Singh and G. Ramanath, *RSC Adv.*, 2014, **4**, 6363–6368.

243 J. C. Boyer, F. Vetrone, J. A. Capobianco, A. Speghini and M. Bettinelli, *J. Appl. Phys.*, 2003, **93**, 9460–9465.

244 L. Calderon, Y. Lu, H. Shen, J. Pamulapati, M. Dutta, W. H. Chang, L. W. Yang and P. D. Wright, *Appl. Phys. Lett.*, 1992, **60**, 1597–1599.

245 H. J. Ko, Y. F. Chen, S. K. Hong, H. Wenisch, T. Yao and D. C. Look, *Appl. Phys. Lett.*, 2000, **77**, 3761–3763.

246 G. S. Lotey, J. Singh and N. K. Verma, *J. Mater. Sci.: Mater. Electron.*, 2013, **24**, 3611–3616.

247 J. C. Tsang, P. J. Dean and P. T. Landsberg, *Phys. Rev.*, 1968, **173**, 814–823.

248 J. D. Ye, S. L. Gu, S. M. Zhu, S. M. Liu, Y. D. Zheng, R. Zhang, Y. Shi, H. Q. Yu and Y. D. Ye, *J. Cryst. Growth*, 2005, **283**, 279 – 285.

249 M. A. Awad, A. M. Ahmed, V. O. Khavrus and E. M. M. Ibrahim, *Ceram. Int.*, 2015, **41**, 10116 – 10124.

250 G. Singh, S. B. Shrivastava, D. Jain, S. Pandya, T. Shripathi and V. Ganesan, *Bull. Mater. Sci.*, 2010, **33**, 581–587.

251 S. Kuprenaite, T. Murauskas, A. Abrutis, V. Kubilius, Z. Saltyte and V. Plausinaitiene, *Surf. Coat. Technol.*, 2015, **271**, 156 – 164.

252 S. K. Swami, N. Chaturvedi, A. Kumar and V. Dutta, *Progress in Photovoltaics: Research and Applications*, 2016, **24**, 74–82.

253 K. Tang, S. Gu, J. Liu, J. Ye, S. Zhu and Y. Zheng, *J. Alloys Compd.*, 2015, **653**, 643 – 648.

254 V. Fathollahi and M. M. Amini, *Mater. Lett.*, 2001, **50**, 235 – 239.

255 H. Mahdhi, Z. Ben Ayadi, N. Hadded, L. Gauffier and K. Djessas, *J. Mater. Sci.: Mater. Electron.*, 2015, **26**, 9873–9881.

List of publications

1. N. J. Blumenstein; C. G. Hofmeister, P. Lindemann, C. Huang, J. Baier, A. Leineweber, S. Walheim, C. Woell, Th. Schimmel and J. Bill, "Chemical bath deposition of textured and compact zinc oxide thin films on vinyl-terminated polystyrene brushes", *Beilstein J. Nanotechnol.*, 2016, **7**, 102-110. (Chapter 3.2 of this thesis)

2. N. J. Blumenstein, J. Berson, S. Walheim, P. Atanasova, J. Baier, J. Bill and Th. Schimmel, "Template-controlled mineralization: Determining film granularity and structure by surface functionality patterns", *Beilstein J. Nanotechnol.*, 2015, **6**, 1763-1768. (Chapter 3.3 of this thesis)

3. N. J. Blumenstein, F. Streb, S. Walheim, Th. Schimmel, Ž. Burghard and J. Bill, "Template Controlled Piezoactivity of ZnO Thin Films Grown via a Bio-inspired Approach", *submitted.* (Chapter 3.4 of this thesis)

4. R. Eisele, N. J. Blumenstein, J. Baier, S. Walheim, Th. Schimmel and J. Bill, "Synthesis and characterization of textured Al-doped zinc oxide films prepared by template-directed deposition", *CrystEngComm*, 2014, **16**, 1560-1567. (Chapter 3.5.2 of this thesis)

Erklärung über die Eigenständigkeit der Dissertation

Ich versichere, dass ich die vorliegende Arbeit mit dem Titel „Template controlled mineralization of functional ZnO thin films“ selbständig verfasst und keine anderen als die angegebenen Quellen und Hilfsmittel benutzt habe; aus fremden Quellen entnommene Passagen und Gedanken sind als solche kenntlich gemacht.

Declaration of authorship

I hereby certify that the dissertation entitled “Template controlled mineralization of functional ZnO thin films” is entirely my own work except where otherwise indicated. Passages and ideas from other sources have been clearly indicated.

Name/Name: _____

Unterschrift/Signature: _____

Datum/Date: _____

Danksagung

An dieser Stelle möchte ich mich bei allen bedanken, die mich während meiner Arbeit unterstützt haben.

Meinem Doktorvater, Herrn Prof. Dr. J. Bill, möchte ich dafür danken, dass ich diese Arbeit an seinem Lehrstuhl durchführen konnte. Ohne unsere Diskussionen und seine Kommentare, wäre diese Arbeit nicht das geworden, was sie jetzt ist.

Herrn Prof. Dr. Ir. E. J. Mittemeijer danke ich für die freundliche Übernahme des Mitberichtes. Herrn Prof. Dr. R. Niewa danke ich für die Übernahme des Prüfungsvorsitzes.

Bei meinen Betreuern Dr. J. Baier und Dr. Ž. Burghard möchte ich mich für die vielen hilfreichen Diskussionen bedanken. Sie hatten immer ein offenes Ohr für mich, selbst dann, wenn sie eigentlich mit anderen Dingen beschäftigt waren.

Meinen Projektpartnern vom KIT danke ich für die freundliche Aufnahme in ihrer Gruppe. Namentlich möchte ich vor allem Prof. Dr. Th. Schimmel, Dr. S. Walheim, Dr. M. Moosmann, Dr. J. Berson und Dr. C. Huang nennen. Meine Besuche in Karlsruhe haben mir immer Spaß gemacht.

R. Eisele, Dr. C. Hofmeister und F. Streb danke ich für dafür, dass sie mir ihre Ergebnisse zur Verfügung gestellt haben. Für experimentelle Hilfe bei Messungen danke ich F. Predel, S. Kilper, M. Dudek, M. Wieland, Dr. A. Leineweber, S. Hammoud, G. Werner, P. Gerstel und Dr. P. Lindemann.

Allen meinen Kollegen der Gruppen von Prof. Dr. J. Bill und Prof. Dr. A. Weidenkaff möchte ich für die schöne Zeit danken. Ich habe gerne mit euch gearbeitet und wir haben viel zusammen erlebt.

Am Ende möchte ich mich ganz besonders bei meiner Familie und meinem Freund Matthias bedanken. Ohne ihre Unterstützung, unendliche Geduld und andauernde Motivation hätte es diese Arbeit wohl nicht gegeben.